Title
Behavior of Nanoscale Water Structures in External Electric Field

Author
Lee, Jane HyoJin

Publication Date
2015

Peer reviewed|Thesis/dissertation

University of California, Merced

Behavior of Nanoscale Water Structures in External Electric Field

A dissertation submitted in partial fulfillment of the requirements
for the degree Doctor of Philosophy

in

Applied Mathematics

by

Jane HyoJin Lee

Committee in charge:

Professor Mayya Tokman, Chair

Professor François Blanchette

Professor Michael E. Colvin

Professor Arnold D. Kim

2015

The Dissertation of Jane HyoJin Lee is approved, and it is acceptable in quality and form for publication on microfilm and electronically:

Mayya Tokman, Chair — Date

François Blanchette — Date

Michael E. Colvin — Date

Arnold D. Kim — Date

University of California, Merced

2015

Dedicated to my parents
in gratitude for their endless love.

Contents

List of Figures

List of Tables

Acknowledgements

Foremost, I would like to express my deepest gratitude to my advisor, Professor Mayya Tokman, for her enormous help and advice and for providing inspiration which cannot be expressed with words. It would have been impossible to overcome the difficult times without her patient care, understanding and encouragement. I am truly grateful for all these years of life guidance and devoted support.

I would like to express my sincere gratitude to committee members Professor Michael Colvin, Professor Arnold Kim, and Professor François Blanchette for their kind and continuous support. I am especially grateful to Professor Michael Colvin for his generous and practical support, moreover for his enthusiastic and valuable help on research work beyond being a committee.

I wish to thank other applied mathematics faculty members at the University of California, Merced, for creating a wonderful studying environment. I would like to mention Prof. Boaz Ilan, Prof. Roummel Marcia, and Prof. Yue Lei to appreciate their thoughtful support and help. I have been very fortunate to meet and share time with many fellow graduate students at the University of California, Merced, during my study. I would particularly like to acknowledge John Loffeld, Nitesh Kumar, Derya Şahin, Garnet Vaz, and SeungBum Park for their full support, friendship and companionship. I want to thank former Graduate Student Programs Coordinator Carrie King for her kind support and wise advice during difficult times. I benefitted a lot from the Center for Research on Teaching Excellence and particularly thank Belinda Braunstein for her kind help.

Last but not least, I thank my family: my parents for their endless love and dedication, and my sister and brother-in-law for their heartful support.

The work in Chapter 2 was supported in part by grant #DE-FG02-04ER25625 from the U.S. Department of Energy, Office of Science, Offices of Advanced Scientific Computing Research, and Biological and Environmental Research through the University of California, Merced - Center for Computational Biology.

The material of Chapter 2 is a reprint of the material as it appears in PLOS ONE. Among the co-author listed in this publication, Mayya Tokman and Michael E. Colvin directed and supervised the research which forms the basis for the dissertation.

The partial work in Chapter 3 used the Extreme Science and Engineering Discovery Environment (XSEDE), which is supported by National Science Foundation grant number ACI-1053575.

Vita

Education

Doctor of Philosophy in Applied Mathematics — Expected 2015
University of California, Merced
Field of Study: Computational Biology, Molecular Dynamics
Advisor: Professor Mayya Tokman

Master of Science in Applied Mathematics — 2005
University of Auckland, New Zealand
Field of Study: Numerical Method for Ordinary Differential Equations
Advisor: Professor John C. Butcher

Bachelor of Science in Applied Mathematics and Physics — 2002
University of Auckland, New Zealand
Field of Study: Electronics and Computing, Applied Mathematics

Honors and Awards

Applied Mathematics Dissertation Fellowship — 2015
University of California, Merced

Applied Mathematics Summer Research Fellowship — 2014
University of California, Merced

2013-2014 Outstanding Teaching Award — 2014
University of California, Merced

Applied Mathematics Summer Research Fellowship — 2013
University of California, Merced

Graduate Division General Fellowship — 2012
University of California, Merced

Teaching Experience

Teaching Fellow, University of California, Merced — 2010–2014
Field of Teaching: Differential Equations, Linear Algebra, Numerical Analysis

Teaching Assistant, University of California, Merced — 2008–2009
Field of Teaching: Calculus, Linear Algebra, Numerical Analysis

Behavior of Nanoscale Water Structures in External Electric Field

by

Jane HyoJin Lee

Doctor of Philosophy in Applied Mathematics

University of California, Merced, 2015

Chair: Professor Mayya Tokman

Abstract

We present our study of the behavior of water at the molecular level in the presence of an external electric field. We develop two model systems using the theory of molecular dynamics (MD) and demonstrate how the tendency of interfacial water molecules to reorganize explains the structural behavior of the systems. Water molecules can interact with external electric fields. This interaction can be observed in various processes such as formation of raindrops in thunderclouds, lightning strikes and electrofreezing. Understanding of this interaction is relevant to variety of applications, like for example, electrospinning, electrospray ionization, crop spraying, spray painting, and inkjet printing. Furthermore, the interaction of water molecules with an external electric field plays an important role in the electroporation process. First, we present a novel theory of electroporation that provides insight into initiation pore formation in biological cell membranes when they are exposed to an external electric field. Using thorough structural and energetic analysis, we demonstrate that the formation of a pore is driven by the reorganization of the interfacial water molecules into energetically favorable structures. Second, we present our study of nano-sized water droplets placed in an external electric field. Our analysis exposes the molecular mechanism behind the nanodroplet shape change from a spheroid to a highly prolate ellipsoid. We demonstrate that a droplet extends its shape as water dipoles align with the electric field while simultaneously restructuring to minimize the dipole-related interaction energy. A new semi-empirical model is developed to predict the critical electric field value which separates the two states. We show that the new model sheds more light onto the dynamics of the system compared to previous theoretical results. Finally, we conclude with a possible future research work.

Chapter 1

Introduction

In this dissertation, we study behavior of water at the molecular level in the presence of external electric field.

Because water is a polar molecule with a large electrical dipole moment and is free to rotate in solution, water molecules can interact strongly with external electric fields. This interaction occurs in variety of interesting chemical, physical, and biological processes. For example, formation of raindrops in thunderclouds and lightning strikes [1, 2] are closely related to this interaction. Long history of scientific research on water and electric field provided a fundamental understanding of electrospray [3] process which advanced into various versatile applications such as electrospinning [4, 5] and Nobel Prize research, Electrospray ionization [6, 7], and electrofreezing [8, 9, 10, 11]. It is further relevant to crop spraying [12], spray painting [13], and inkjet printing [14, 15] processes. Moreover, since water is integral ingredient of many biomolecules and plays an essential role in biological cells and biomolecular interactions, the interaction of water molecules has significant effect in biotechnical processes involving external electric field such as electroporation [16, 17, 18, 19, 20, 21, 22]. The main motivation for our work comes from understanding the mechanism of electroporation.

Electroporation, also known as electropermeabilization, is a membrane phenomenon involving breaching the integrity of the cell membrane by an externally applied electric field. The electric field charges the cell membrane and increases the electrical conductivity and permeability significantly. Under the influence of electric field pores are created which allows molecular transport across the cell membrane. Electroporation has broad range of applications in biology, biotechnology, and medicine. For example, it can be used to deliver drugs and to transfer genes into cells or to treat tumors [23, 24, 25]. Despite the fact that electroporation is used in many field, the mechanism of pore creation is not understood. We propose a new theory that provides insight into why pores form in membrane when its exposed to external electric field.

Our work split into two parts. The first part concerns understanding cause of pore formation in the cell membrane during the electroporation process. The effect of imposing external electric field and their interactions with biological structures remain unknown. Particularly, the mechanism and the cause of structural defects like nanopores in lipid bilayers are not fully understood. Although the importance of role of water was noticed before [18], the majority of investigations focused on how the lipids respond to an externally imposed electric field [26, 27, 28, 22].

We propose a new hypothesis for explaining pore formation as a consequence of the dynamics of water molecules in the electric field. Our main tool for studying the role of water molecules in the process of electroporation is computational molecular dynamics (MD). We use a versatile MD package GROMACS to simulate our models and perform statistical analysis of simulation results as well as create additional mathematical models. Our study demonstrates that water is not just important but in fact is the main driver behind the electroporation process. More precisely, our analysis demonstrates that the tendency of interfacial water molecules to organize in order to minimize their energy serves as an initial step in the formation of the pore.

While the first part of our work provided a valuable insight into the process of electroporation, there are certain limitations associated with simulating a small portion of a membrane. For example, use of periodic boundary conditions is necessary to simulate a piece of a membrane at the molecular level. Particle Mesh Ewald [29] is required to approximate the electrostatic forces and cut-off is used to compute van der Waal's interactions associated with periodic boundary conditions. Hence, we developed a different model to overcome the limitations and to support the conclusion about behavior of interfacial water molecules in the electric field and to generalize our result in case when these forces are exactly computed.

The second part focuses on modeling nano-sized water droplets and investigates the behavior under the influence of an externally applied electric field. Study of the effects of electric fields on liquid drops dated back to the work of Rayleigh [30] in 1879. Later in 1964, Taylor [31] made an significant contribution on the research of behavior of water drops in strong electric fields and proposed a theoretical model that assumes the droplet shape stays as symmetrical ellipsoid in equilibrium state (i.e. when the fluid pressure, surface tension of droplet, and force due to internal electric field are balanced). In the past few decades, understanding the behavior of water molecules in droplets in electric field became more important and relevant to a variety of applications mentioned above i.e. metrology [32], electrospray [3], etc. However, majority efforts have been in large scale droplets. Theoretical approaches has been done to study disintegration mechanism of electrified drops [33, 34]. Although there has been studies of nano-sized water droplet coalescence [35, 36, 37] and studies of nano-sized charged droplets [38, 39] using MD, to our knowledge, our work is the first addresses the molecular level behavior of nano-sized water droplets itself in applied external electric field.

This dissertation is organized as follows. Chapter 2 presents the first part of work, the new theory of electroporation. We directly address modeling the process of pore formation during electroporation procedure. We describe our simulation models and the analysis tools we developed and explain the statistical analysis result in structural and energetic perspectives to understand the driving forces behind this initiation of pore process. In addition, we present a simple mathematical model to support our understanding of formation of protrusions at the interface as a result of electrostatic energy minimization. Chapter 3 presents the second part of work, the modeling of nano-sized water droplets. We explain the molecular mechanism behind the shape deformation through large number of MD simulations and careful analysis of the structural and energetic behavior of the nanodroplets as the electric field is varied from low to high strengths. We confirmed that the minimization of energy in fact takes place in shape deformation. We present a quantitative theory is developed to

describe the energetic landscape of the nanodroplet shape transitions between equilibrium states as well as the relationships among the critical electric field that causes the shape extension and the strength of the applied field and the initial size of the nanodroplet. In addition, we show that Taylor's physics-based model for macro-size droplet can be used for nano-sized droplet to predict the critical electric field. We also present the derivation of predictive semi-empirical model using the internal energy of the droplet that provide good prediction of the droplet's shape dynamics while ignoring the entropy term included in the free energy analysis. Furthermore, we show that nanodroplets in an electric field follows Arrhenius-like behavior as it has to overcome the energy barrier to reach the global minima. Finally, in Chapter 4, we conclude the dissertation with a short summary and the future work.

Chapter 2

Study of Electroporation of Lipid Bilayer Membranes

2.1 Introduction

Electroporation, also known as electropermeabilization, is the breaching of the integrity of the cell membrane that follows the application of an external electric field of sufficient magnitude and duration. In this process permeabilizing structures (pores) appear in the membrane, allowing molecular transport across this normally impermeable barrier [16, 40, 41]. Electroporation has a broad range of applications in biology, biotechnology, and medicine, from drug and gene delivery into cells to tumor therapy [42, 43, 44, 45, 46]. Despite the wide laboratory use of electroporation, the details of the effects of electric fields on biological membranes, and particularly the molecular mechanisms of pore creation in living cells, are not well understood [47]. Our limited knowledge of this phenomenon causes difficulties in controlling the process in clinical applications and limits development of new technologies.

Permeabilization can be monitored by tracking the transport of normally impermeant materials across the cell membrane or by measuring changes in the electrical properties of the membrane, but direct experimental observation is difficult because of the small spatial and fast temporal scales of this process. Theoretical models have been developed to facilitate the interpretation of experimental data and the understanding of the mechanism of electroporation. Although continuum models [48, 49] can predict large-scale features of electroporation, they lack details regarding pore initiation, growth, and decay and contain empirically fitted parameters. Molecular dynamics (MD) simulations provide access to the microscopic structure of a membrane and its interaction with the surrounding solvent and ions in atomic detail. Since we are interested in understanding the molecular mechanism of electropore creation and evolution, we employ MD to study this problem.

Our model focuses on the basic building block of a cell membrane the phospholipid bilayer. While there is evidence that electroporation is to some extent affected by the complex structure of the cell membrane (e.g. oxidized lipids, cholesterol, lipid heterogeneity, cytoskeletal attachments, etc), the electrical breakdown and the subsequent increase in membrane conductance has long been observed experimentally in simple planar lipid bilayers [50, 51, 52, 53, 54, 55, 56]. In addition, experimental observations of electroporation due to external nanosecond electric pulses [57] further indicate that while ion channels, cytoskeletal networks, and membrane-associated polypeptides can facilitate additional permeabilization

of the membrane, these effects would occur in conjunction with and possibly on a longer time scale than the electrical breakdown of lipid bilayers.

Some MD studies of electroporation have emphasized how phospholipids respond to external electric fields [19, 58, 22]. The behavior of water dipoles in the complex electric field landscape of the membrane interface has also been noted as an important part of the pore formation process [18]. But the precise cause of pore formation has not been identified, and the roles of phospholipid and water molecules have not been clearly understood. In this article we argue that the electric field-driven reorganization of water dipoles is the primary contributor to electropore formation. We explain pore creation as the result of a rearrangement of interfacial water dipoles into a lower energy configuration in the presence of an external electric field. A scenario for pore formation is presented in which the coherent behavior of water dipoles plays the primary role, while lipids act as somewhat resistive partners in this process. This view simplifies the study of electroporation, stresses the importance of understanding the dynamics of water under the influence of an external electric field in interfacial processes, and opens up new ways to directly connect this problem to those of classical statistical mechanics.

In this work we emphasize the fundamental biophysical interactions between electric fields and molecules in a simple, homogeneous, phospholipid bilayer interface. Although biological membranes are considerably more complex, and electroporation protocols often involve the application of electric fields for much longer times than those considered here, it is our expectation that the model presented will establish the primary events and actors even for more complex descriptions of a membrane.

2.2 Models and Methods

2.2.1 Model systems

In order to clearly illustrate the primary role of water dipoles in electropore formation we study two configurations using MD: water-vacuum-water (WVW) and water-lipid-water (WLW).

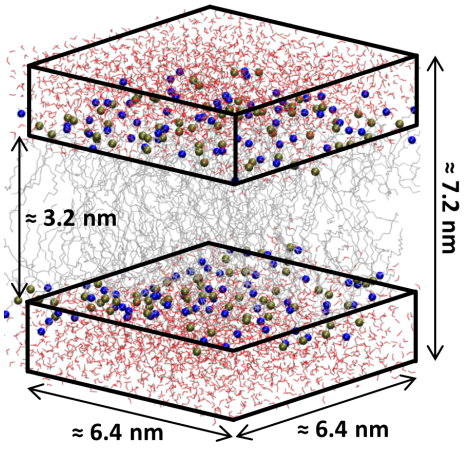

Figure 2.1: WLW system

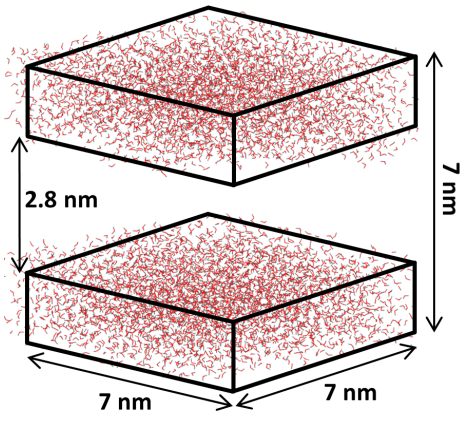

Figure 2.2: WVW system

The WLW systems (Figure 2.1 contain 128 1-palmitoyl-2-oleoyl-*sn*-glycero-3-phosphocholine (POPC) lipids and 4480 water molecules (35 waters/lipid), which results in a system box size of approximately 6.4 nm $\times$ 6.4 nm $\times$ 7.2 nm. The two directions tangential to the POPC bilayer are defined as the X and Y directions, with Z perpendicular to the plane of the membrane. To ensure that replicated simulations are independent, each atom was assigned a randomized velocity from a Maxwell distribution at the beginning of a simulation. POPC systems were equilibrated before the application of an external electric field by allowing the simulations to proceed until a constant area per lipid (approximately 0.66 nm^2) was reached (typically in 1030 ns).

The WVW systems (Figure 2.2) are comprised of 6877 water molecules arranged in two layers of thickness 4.2 nm separated by a 2.8 nm vacuum gap. This configuration was constructed by generating a 7 nm $\times$ 7 nm $\times$ 7 nm periodic water box with the `GROMACS` utility '`genbox`', then using custom `Perl` scripts to remove a 2.8 nm slice of water molecules from the center of the system, followed by 300 ps of equilibration at constant volume. The dimensions of this box and the gap size have been chosen carefully in order to produce a realistic equilibrated initial system in which the surface area of the water-vacuum interface is minimized and to ensure that the magnitude of the electric field in the gap is comparable to that of a WLW simulation (Appendix C). Under non-periodic conditions, the introduction of a vacuum gap into a constant volume system will lead to formation of a spherical bubble that minimizes the area of the water-vacuum interface. However, for a periodic cube, depending on its dimensions and the width of the vacuum gap, one of three possible configurations (a spherical bubble, a tube, and a slab with a vacuum gap in the middle, see Figure C.1 in Appendix C) can minimize the interface surface area given a constant volume. For a cube with a side edge length L and a vacuum gap of height Z, the water-vacuum gap-water configuration will have the lowest interface surface area, provided that Z obeys the relationship $Z > \frac{L}{\pi}$ (see Figure C.2 in Appendix C for details). We verified this theoretical result with MD calculations which confirmed that given a fixed volume of water in the box satisfying the above condition on Z, any initial configuration evolves to a minimum surface area state which is indeed comprised of two water layers separated by a vacuum gap. In these validating simulations, the initial system was run for up to 40 ns to ensure that the final state was in fact the equilibrium minimum-surface area configuration. This method allowed us to generate a WVW slab that is stable for tens of nanoseconds, a time scale which is much longer than the characteristic poration time. While the stability of the WVW slab configuration is an artifact of the periodic boundaries, the initial steps in pore formation described here involve a very small volume of water compared to the size of the simulation box and are not affected by the periodicity of the configuration.

After equilibration of the initial WVW and WLW systems we impose an electric field in Z direction perpendicular to the membrane surface, and observe the dynamics of the water in the presence of a constant field. We have performed simulations with external electric field values between 450 MV/m and 1000 MV/m and vacuum gap width ranging from 2.8 nm to 4.0 nm (see tables in Appendix B for details) and found no qualitative changes in the system dynamics. Quantitative differences such as reduction in the time scale of the process as the value of the external electric field grows are described in the subsequent sections.

2.2.2 Molecular Dynamics Simulations Protocols

All simulations were performed using the GROMACS set of programs version 4.5.3, as previously described [59]. The Extended Simple Point Charge (SPC/E) water model [60] was used for all simulations presented here, although we obtained similar results using SPC [61] and SPC/E flexible [62] water models. Lipids are parameterized with OPLS headgroups and Berger hydrocarbon tails [63]. Any atoms which are not explicitly modeled with OPLS or Berger parameters use the native GROMOS87 force field built into GROMACS. Lipid topologies were obtained from Tieleman's group (http://www.ucalgary.ca/tieleman/).

All simulations were coupled to a temperature bath at 310 K with a relaxation time of 0.1 ps and a pressure bath at 1 bar with a relaxation time of 1 ps, each using a weak coupling algorithm [64]. For lipid systems, pressure was coupled semi-isotropically (using a compressibility of 4.5 $\times 10^{-5}$ bar^{-1}) normal to and in the plane of the membrane (NPT). No pressure coupling was used for water-vacuum systems where volume was held constant (NVT). WLW systems were simulated in the NPT ensemble at 1 bar to maintain a dynamically controlled area per lipid before pore formation. WVW systems were run in the NVT ensemble to constrain the box dimensions and water slab separation. Note that despite the different ensemble used for the WLW system, over the time interval of interest the size of the computational box did not fluctuate by more than 0.1 nm without external electric field and 0.5 nm in the presence of electric field.

All simulations were performed with a time step of 2 fs and with Bussi *et al.*s stochastic velocity rescaling algorithm [65] as a temperature coupling method. Bond lengths were constrained using the LINCS algorithm [66] for lipids and for water. All bond lengths were fixed using constraints after the integration of forces. Following Essmann, et al. [29], the Particle Mesh Ewald (PME) method with tinfoil boundary conditions was used to handle long-range electrostatic forces and cut-offs were employed for calculating van der Waals interactions. In the simulations presented in the next section all of the relevant cut-off distances were set to 1.4 nm. However, we performed simulations with electrostatic cutoffs set to 1.0 nm, 1.2 nm, 1.4 nm, 1.6 nm, and 1.8 nm and found that the results were robust with respect to this parameter and that the dynamics of the pore initiation were qualitatively unchanged.

For systems with an external electric field, the orientation of polar molecules, such as water, in the field induces a net dipole on the system, which has been reported to cause spurious dipole orientations [67]. For the WVW system we investigated several alternative treatments of the long-range electrostatic forces, including PME with non-conducting infinite boundaries, very long cut-offs (3.4 nm), and the reaction field approach, and found that the process of pore initiation is similar, albeit at slightly different electric field strengths. After the pore forms and begins to occupy a significant portion of the computational box, the average dipole saturation differs for different choices of long-range electrostatics approximations and affects the growth rate and stability of the pore. These post-initiation stages in pore development require different models and will not be addressed in this study. Here we focus on the pore initiation process.

2.3 Results and Discussion

(a) WLW configuration

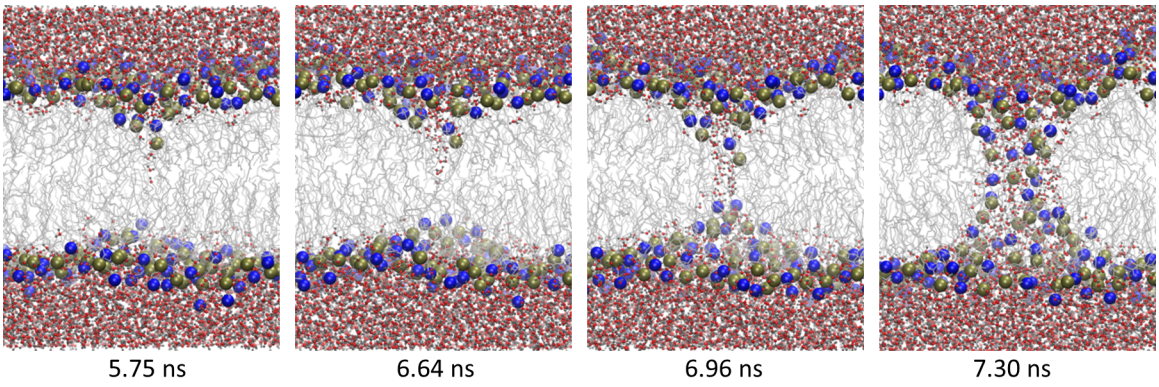

(b) WLW configuration: water only

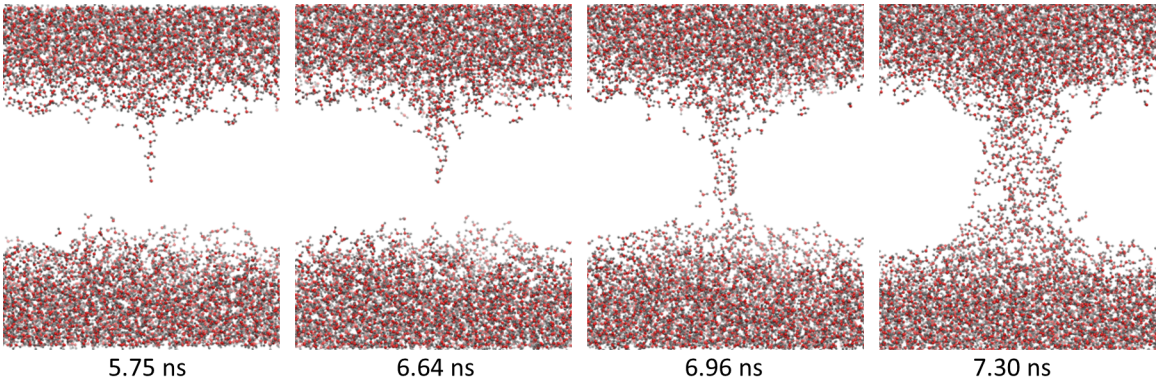

(c) WVW configuration

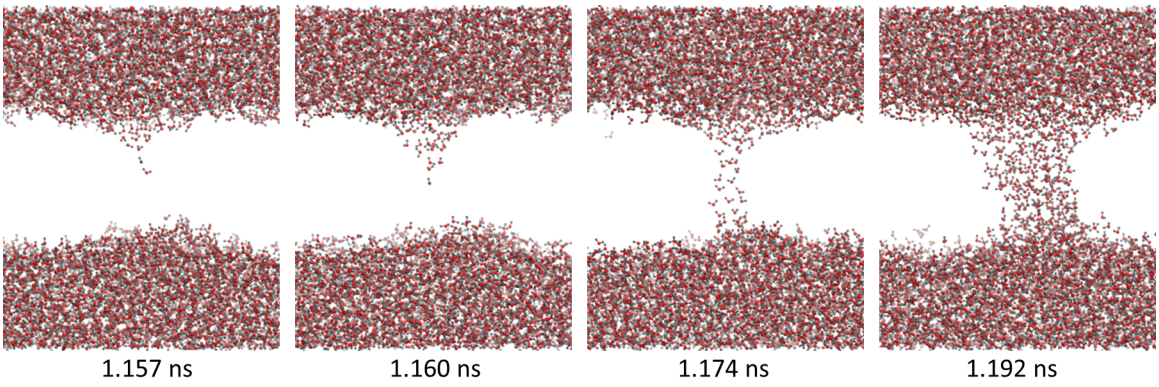

Figure 2.3: Snapshots of the time evolution of water-lipid-water (WLW) and water-vacuum-water (WVW) configurations under an external electric field of 500 MV/m. (a) is WLW configuration at the indicated times with both water molecules (oxygen red, hydrogen - gray) and lipid molecules (phosphorus - yellow, nitrogen - blue, lipid tail groups silver) displayed. (b) is the same WLW data as in (a) but with only water molecules shown. (c) WVW configuration at the indicated times.

We concentrate here on the analysis of 60 specific replicate simulations of WLW systems and WVW systems with an external electric field strength of 600 MV/m, but similar results were obtained in additional simulations (hundreds in total) with different thermodynamic ensembles, water models, electrostatic cutoff distances, and applied electric fields, as described above (see tables in Appendix B for details). The dynamics of the pore initiation process and the substance of our conclusions regarding its cause are robust and apply in general to all of these cases.

2.3.1 Dynamics of the Systems

The dynamics described in this subsection were observed in all simulations; we present in detail the results of one representative simulation to illustrate characteristic behavior. Figures 2.3(a) and 2.3(b) show the time evolution of a water-phospholipid bilayer-water (WLW) configuration over 14 ns. Figure 2.3(a) and 2.3(b) render the same data set, but Figure (a) displays both water and lipid molecules, while Figure (b) shows only water molecules. Pore formation can be roughly described as a three-part process. First, a deformation directed towards the interior of the membrane forms at the water-lipid interface. Second, this bump grows, and eventually water molecules from one side of the bilayer meet water from the opposite side to form a bridge, closely followed by lipid head groups. Third, the newly formed column of water between the two sides of the bilayer expands to become a lipid pore - a structure with water molecules in the middle and lipid head groups lining the periphery. A detailed description of this process can be found in earlier publications [19, 18, 59].

Figure 2.3(b) shows the process of pore formation from the perspective of water dynamics. Pore formation starts with protrusions consisting of a few water molecules, often as a single-file column, appearing either side of the bilayer. A protrusion extends into the bilayer interior and then expands at the base, forming a conical structure which eventually bridges the membrane. The radius of the water column spanning the bilayer then begins to increase.

Now let us examine the water-vacuum-water (WVW) simulations. Figure 2.3(c) displays the time evolution of the molecules in the water slabs under the influence of an externally imposed electric field. The progression of the dynamics of water column formation is very similar to the behavior of water in the WLW system (compare Figures 2.3(b) and 2.3(c)). The dynamics of pore (water column) formation and the similarity between WLW and WVW simulations are invariant across simulations over a wide range of parameters (e.g. external electric field between 450 MV/m and 1000 MV/m, vacuum gap width ranging from 2.6 nm to 4.0 nm. see tables in Appendix B for details).

WLW and WVW simulations differ mainly in the time scale over which the formation of the water bridge occurs, i.e., the pore initiation time [59]. To compare initiation times between WLW and WVW systems, we selected a gap size for WVW systems that result in the same magnitudes of the external and internal (in the lipid bilayer interior and the vacuum gap) electric fields. This ensures that the interfacial water molecules are exposed to similar electric fields in the WLW and WVW systems, permitting a fair comparison of pore initiation times (see Appendix C). With equivalent external and internal electric fields, WVW systems porate faster than WLW systems as you can see in Figure 2.4. We hypothesize that the lipid bilayer acts as a barrier to the interfacial water dipoles, retarding the formation of the water bridge connecting the two water layers. The energetics analysis

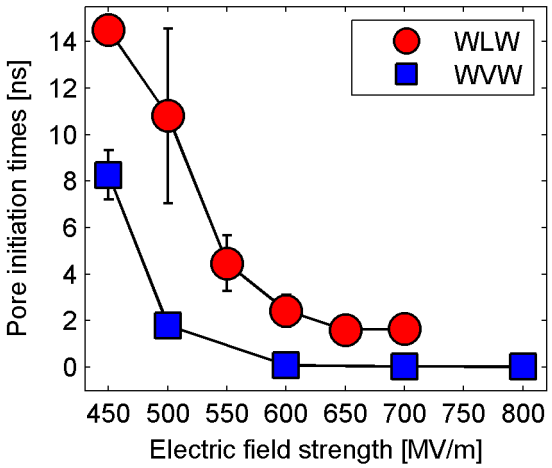

Figure 2.4: Average pore initiation times for WLW and WVW systems calculated with three sets of simulations for each configuration.

presented in the next sections supports this hypothesis.

2.3.2 Energetics Analysis of the Systems

We now discuss the energetics of the simulated systems. We demonstrate that the pore formation process described above is driven by the collective tendency of the interfacial water dipoles to minimize their electrostatic interactions while adopting an orientation that minimizes the energy of the water dipole in the external electric field, reflected in the steady drop in the per-molecule energy of waters in the nascent pore as the protrusion develops. Below we demonstrate that this energetic behavior is present in both WVW and WLW simulations.

In order to carry out the analysis, we developed the following tools to examine the energetics of water protrusion formation in ten WLW and ten WVW simulations. First, we define the interface region of the water as follows. The computational box is split in the Z dimension into rectangular slices of thickness 0.1 nm. In each slice the average density of water molecules is calculated, and the highest value is defined as bulk density. Slices with water density not exceeding 50% of the bulk value are considered interfacial, and those with water density equal to or greater than 50% of the bulk value are treated as bulk.

In order to compute the time history of the protrusion energetics, we must identify the water molecules directly involved in protrusion formation. Note that the trajectory of an individual water molecule is very noisy so that selecting protrusion molecules for each time frame is both impractical and arbitrary. Instead we select a rectangular box that includes all of the water molecules we consider to be in the protrusion at the end of our time interval of interest, i.e. at the time when pore initiation is complete, then work backwards to track all water molecules located in this box in each preceding time frame.

To define the box containing water protrusion molecules we carefully inspect the VMD [68] visualizations of the data to find the point in time when the water molecules in the protrusion growing from one of the water layers join with the water molecules from the opposite water layer. At this time point – the end of protrusion initiation time and the beginning of pore formation – we find the coordinates of the extent of the box containing protrusion water molecules in X and Y and the height of the protrusion, i.e. the coordinate of the top of the protrusion box, in Z. The base of the protrusion box in Z coincides with the

boundary of the interface region (i.e. the point above which the density of water does not exceed 50% of the bulk water density). The coordinates of the protrusion box containing this set of water protrusion molecules are then set for all time frames.

Once we isolate the water molecules comprising the protrusion, we compute the time history of the average potential energy per protrusion molecule and its constituent terms, specifically: (i) the electrostatic interaction energy (equation A.1 in appendix A) between water molecules in the protrusion and all other water molecules, (ii) the Lennard-Jones approximation (equation A.2 in appendix A) to the van der Waals interaction between protrusion and bulk water, and (iii) the interaction energy between the protrusion water dipoles and the external electric field (equation A.3 in appendix A). For WLW simulations we also compute the electrostatic and Lennard-Jones interaction energies between the protrusion water molecules and the lipids. Note that all energetic terms are computed as averages per protrusion molecule. That is, at each time frame we determine how many water molecules are in the protrusion box and divide each of the interaction energy values by the number of protrusion molecules. The details of the energy terms calculations can be found in Appendix A.

In addition to the energy terms, we calculate the height H of the protrusion as the distance between the interface region boundary and the protrusion atom (i.e. an atom in the protrusion box), which is the farthest from this boundary in Z. Since the data is noisy, for each variable we also compute a smoothed version using a 50 ps moving average for WLW and a 2 ps moving average for WVW simulations.

For each of the simulations we use visualization of data to determine a time interval over which the tip of the protrusion extends from approximately the top of the interface layer to roughly half of the height of the middle region free of water molecules. In this way we capture the protrusion just after it begins to grow and just before it starts interacting with the water molecules in the layer on the other side of the vacuum gap or lipid bilayer. Since there is so much variation between replicate simulations, we determine this time interval for each simulation individually both from the perspective of the protrusion height as well as the energy variables. Figure 2.5 illustrates typical positions of the protrusion and the rest of the water molecules at the initial and the final points of the identified time interval. The figure displays the data from a single WVW simulation but the rest of the WVW and all of the WLW simulations yield a qualitatively similar picture.

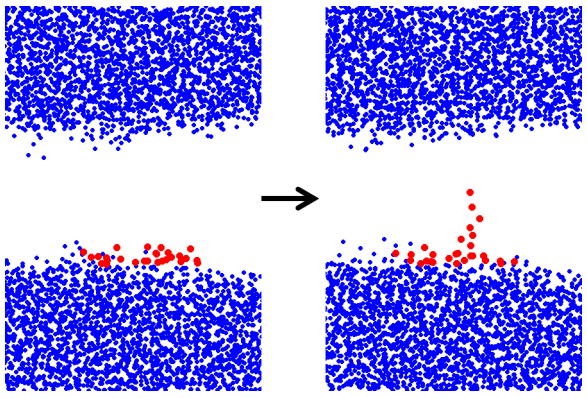

Figure 2.5: XZ-projection of the water molecules positions in a typical WVW simulation. The left picture is just before protrusion begins to grow and the right picture is just before it begins to interact with/attract water molecules from the other side of the gap. Protrusion molecules are colored in red and the rest of the water molecules are shown as blue.

This analysis reveals a drop in the per-molecule energy of the waters in the protrusion as the height of the protrusion grows for both WLW and WVW as seen in Figure 2.6.

To show a correlation between this drop in energy and the protrusion growth for each simulation we computed the Pearsons correlation coefficient between the smoothed data for protrusion height and each of the energies per protrusion water molecule over the time interval described above (mid-point of protrusion growth).

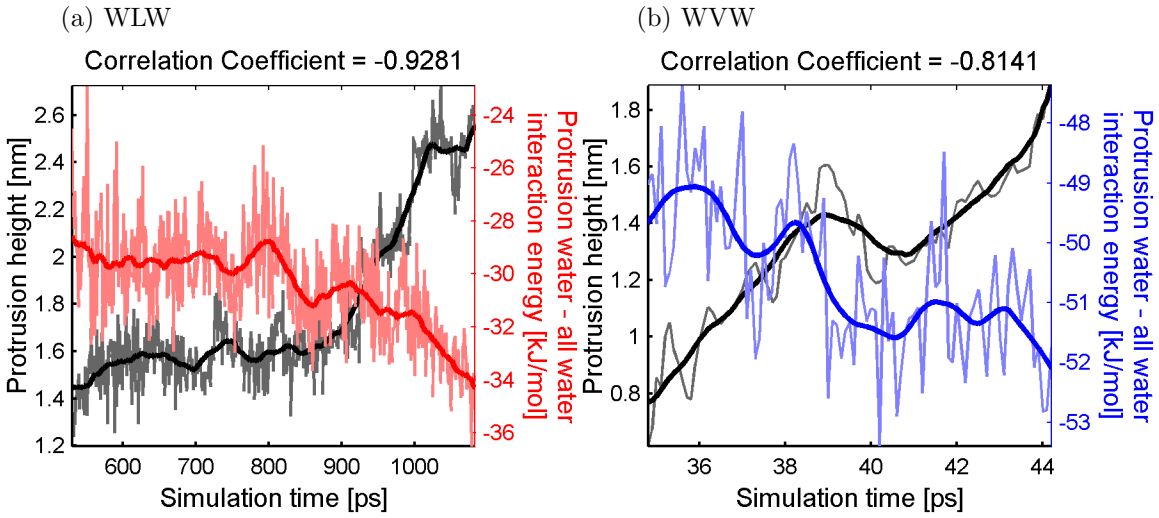

Figure 2.6: Graphs demonstrating anti-correlation between the increase of the protrusion height (black curve) and the decrease of the total interaction energy per protrusion molecule of protrusion waters with all other water molecules (both in the protrusion and in bulk) for (a) WLW (red curve) and (b) WVW (blue curve) simulations

First, we examine the correlation coefficient between the protrusion height and the sum of all the energetic interaction terms (i), (ii) and (iii) between the protrusion water and the bulk water. Figure 2.7 displays histograms of the correlation coefficient distribution across the WLW (Figure 2.7(a)) and WVW (Figure 2.7(b)) simulations. For the thirty WLW simulations this correlation coefficient has a mean value of -0.65 and a median value of -0.76. Note that the correlation coefficient is negative for 29 of the 30 thirty simulations. Under close inspection we find that the one simulation with a positive correlation coefficient exhibits anomalous protrusion formation. In this case some of the water molecules become detached from the bulk for a portion of the pore formation process. This makes it difficult to identify and isolate the protrusion molecules using our procedure. The results for the 30 simulations clearly demonstrate, however, that the growth of the protrusion is coupled with a drop in the average interaction energy for the water molecules in the protrusion.

The results for the WVW simulations are noisier, since water molecules move more freely into and out of the interface and protrusion regions than they do in WLW systems, where the interface water mobility is tempered by the presence of lipid headgroups. The mean of the correlation coefficient is -0.5, and the median is -0.63. Despite the noisier data, for 25 of 30 WVW simulations the correlation coefficient is negative. In four of the five WVW simulations with positive correlation coefficients we find that fluctuations in the extent of the protrusion during its growth make it difficult to isolate the protrusion molecules in a rectangular box. In the fifth simulation (correlation coefficient 0.82) we find two protrusions

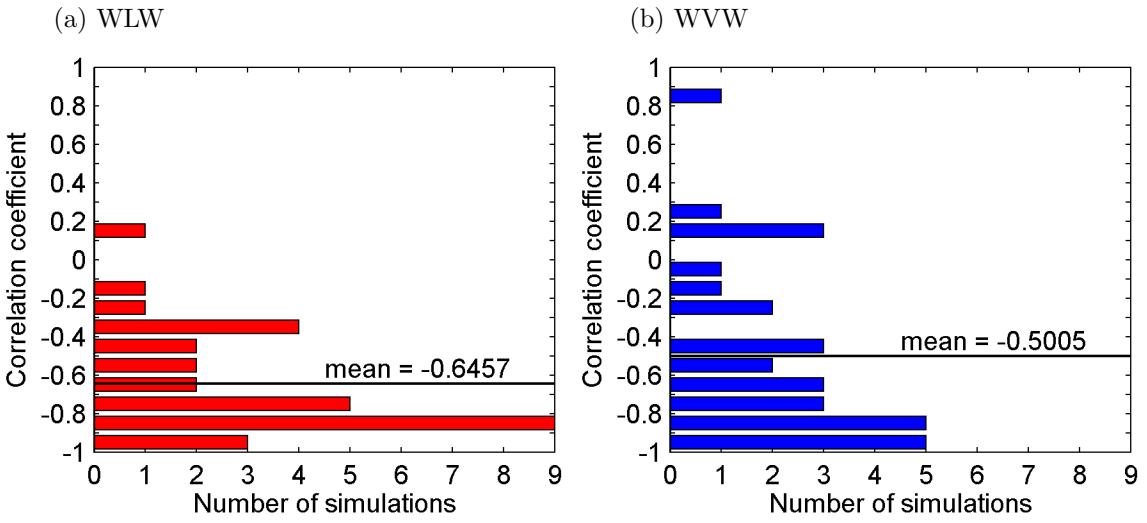

Figure 2.7: Histograms of the Pearson correlation coefficients demonstrating anti-correlation between the increase of the protrusion height and the decrease of the total interaction energy per protrusion molecule of protrusion waters with all other water molecules (both in the protrusion and in bulk) for (a) WLW and (b) WVW simulations.

growing in close proximity, and the interaction between the two protrusions appears to affect the dynamics. Isolating the energetics of one of the protrusions is difficult and incomplete, since it is significantly affected by the neighboring protrusion. The deviation from the negative correlation in these exceptional cases does not alter the overall conclusion for the energetics of protrusion water molecules. Statistically both in WLW and WVW simulations we see a clear correlation between the growth of the protrusion and the decrease of the per protrusion water molecule interaction energy between the protrusion water and the bulk water.

In order to illustrate the details of the interaction energies evolution as the protrusion grows we choose two representative simulations, a WLW and a WVW system, and examine their energetics. The results of this comparison are presented in Figures 2.6 and 2.8. From Figure 2.6 we can see why the correlation coefficient in both cases is negative: as the height of the protrusion grows (black curve), the sum of total protrusion-protrusion and protrusion-bulk water interaction energies per protrusion molecule (WLW red curve, WVW blue curve) decreases. Note that over the course of the identified time interval the magnitude of the decrease in the total potential energy per protrusion molecule is comparable for all sixty WLW and WVW simulations, with WLW systems showing a slightly higher decrease. On average the protrusion water molecule energy in WLW simulations is reduced by approximately 2.8 kJ/mol, while for the WVW protrusion waters the total potential energy decreases by 1.4 kJ/mol.

In Figure 2.8 we decompose these total energies into the three components discussed above, (i), (ii) and (iii), to illustrate how this decrease is accounted for. The potential energy decrease is mainly due to the decrease of the electrostatic interaction energy (Figure 2.8(b)). The dipole-external electric field interaction term decreases slightly (Figure 2.8(a)), and the

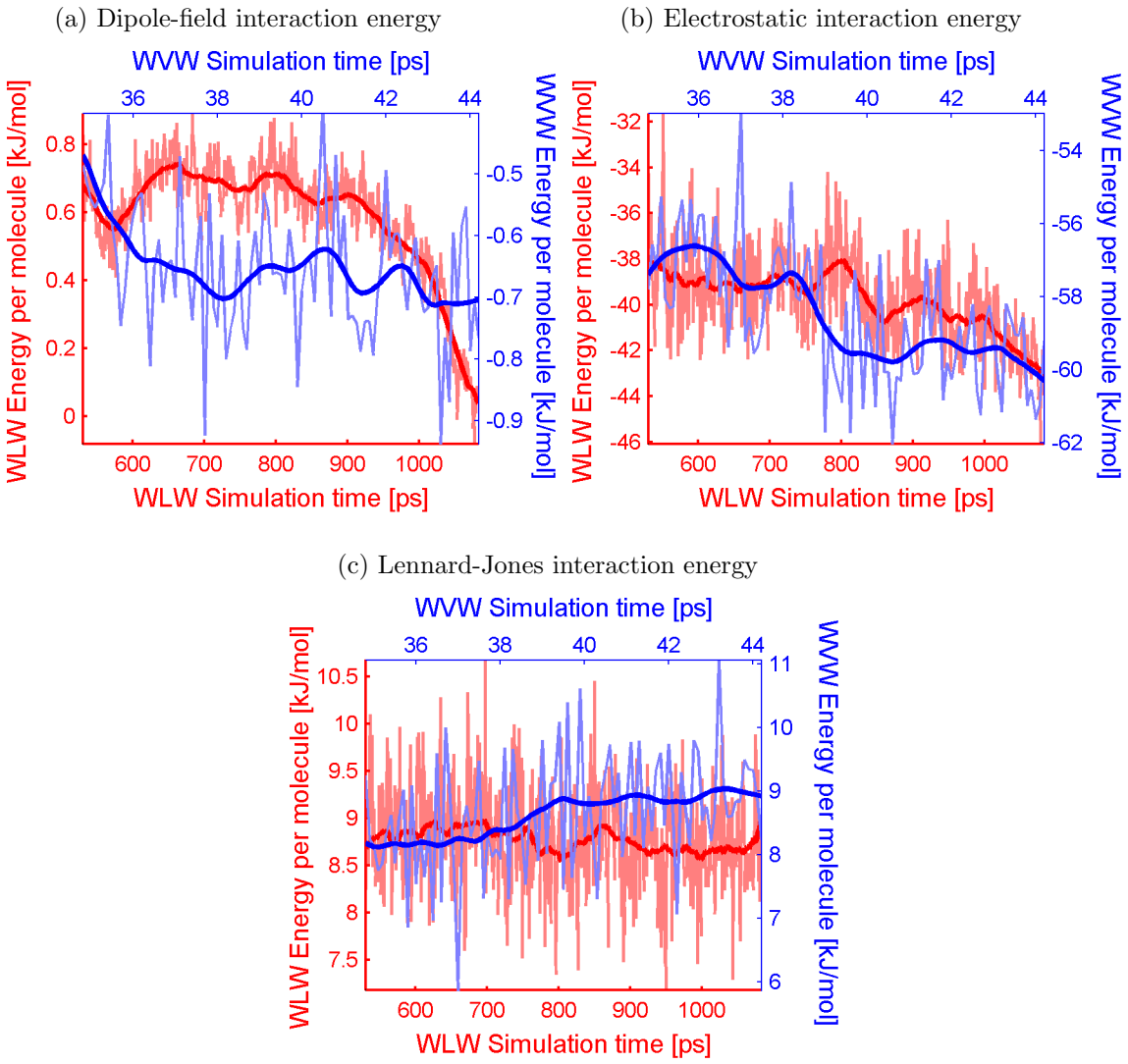

Figure 2.8: Comparison of constituent terms of the total interaction energy per protrusion molecule between WLW (red curve) and WVW (blue curve) simulations: (a) dipoleexternal electric field interaction energy, (b) electrostatic interaction energy, (c) Lennard-Jones interaction energy.

Lennard-Jones potential energy remains largely unchanged (Figure 2.8(c)). The decrease in the dipole-electric field interaction term corresponds with the alignment of the protrusion molecules with the external field. To examine this alignment more closely we also compute an average angle between water dipoles and the electric field in the protrusion and in the bulk. We find that from the start of a simulation to the end of the pore initiation process in the thirty WVW systems this angle is reduced by 19 degrees on average for the protrusion waters and by only 4 degrees in the bulk. Similarly, in the thirty WLW systems the dipole-electric field angle decreases by 11 degrees in the protrusion and only by 2 degrees in the bulk.

To summarize, these results present a scenario of protrusion evolution in which the

interfacial waters, constrained less than the molecules in the bulk, align with the external field and are restructured into a protruding column, where the dipoles are arranged vertically in a configuration that is energetically more favorable than a horizontal arrangement in the plane of the membrane. The external electric field drives the water molecules to overcome their interfacial and bulk interactions and to form the protrusion.

The fluctuations in the WVW system are larger, but the overall energetic behavior of the protrusion molecules is similar between WLW and WVW systems and consistent throughout all thirty simulations. The main difference between WLW and WVW dynamics is the time scale of protrusion and pore formation. In the WVW case the water molecules are more mobile and free to form a protrusion since they are not restrained by the lipid membrane.

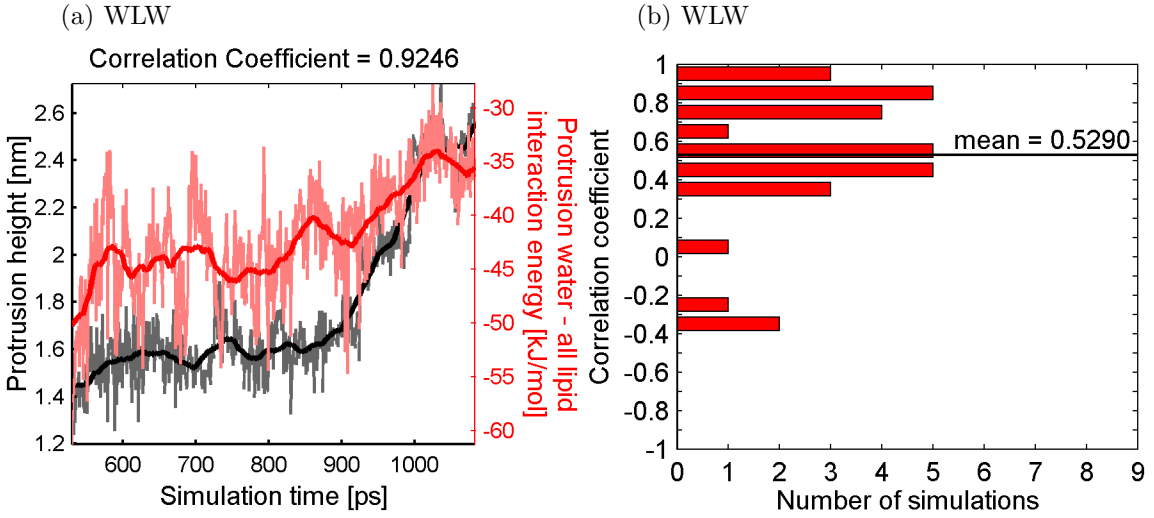

Figure 2.9: A graph (a) and a histogram of the correlation coefficient (b) demonstrating positive correlation between the protrusion height growth and the increase in the total interaction energy between the protrusion waters and the lipids in WLW simulations.

The retarding effect of the phospholipids on water protrusion formation can be quantitatively verified by an examination of the protrusion waterslipids interaction energy. For the WLW simulations we have computed a correlation coefficient between the protrusion height and the sum of the electrostatic and Lennard-Jones interaction energies between protrusion water molecules and the lipids in the system. As before, this term is calculated per protrusion water molecule. For the thirty WLW simulations the correlation coefficient ranges from -0.38 to 0.96 with a mean of 0.53 and a median of 0.57. Figure 2.9 shows a typical evolution as the protrusionlipid interaction energy increases with the growth of the protrusion height. While Figure 2.9(a) displays interaction energy between protrusion waters and all other lipids in the system, we also calculated this energy including only lipids neighboring the protrusion as follows. We have found all lipid molecules which have at least one headgroup atom located within 5 Å of any protrusion atom. We designated these lipids as neighboring the protrusion and computed two interaction energies - between protrusion waters and the neighboring lipids only (Figure 2.10(a)) and between protrusion waters and the rest of the lipids (Figure 2.10(b)). As we can see from Figure 2.9 and Figure 2.10,

the neighboring lipids only make any significant contribution to the protrusion-lipids interaction energy. Given the positive correlation between the growth of the protrusion and the protrusion water-lipids interaction energy increase, we conclude that as the protrusion forms, the initial interaction between the protrusion molecules and the lipids is unfavorable and lipids serve as a barrier delaying the formation of the protrusion.

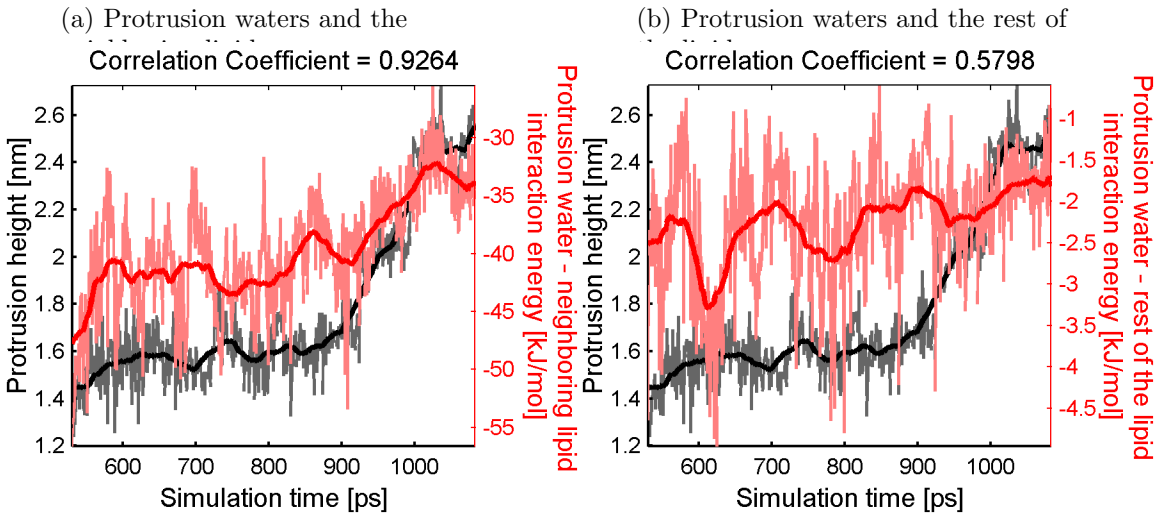

Figure 2.10: Per-protrusion-molecule interaction energy between protrusion and (a) only the neighboring lipids and (b) the rest of the lipids, excluding neighboring lipids.

While it is not possible to consider the protrusion molecules as an isolated subsystem with self-contained energetics and clearly decreasing total energy, our analysis reveals similarities between the WVW and WLW systems at both structural and energetic levels. Based on these results we argue that the same mechanism of electrostatic energy minimization in the presence of external electric field drives formation of pores for both WLW and WVW configurations, but the presence of lipid bilayer slows down this process.

2.3.3 Simple theoretical model of seven dipoles

The following simple theoretical model illustrates the results of the simulations and the energetic benefits of a protrusion creation. Consider two configurations of seven dipoles: (I) a horizontal (i.e. perpendicular to the external electric field direction) sheet of equidistant dipoles, where the mean dipole component $< \mu_E >$ in the direction of the external electric field E is set according to the theoretically established dependency of $< \mu_E >$ on the magnitude of E in bulk water; (II) a vertical (i.e. parallel to the external electric field direction) single-file chain of equidistant dipoles aligned with the external electric field.

In both configurations, the distance between dipoles is set to 0.31 nm in agreement with the average spacing of water molecules in the `SPC/E` model. For the planar dipole configuration, the component of the dipole moment μ_E in the direction parallel to the electric field is assumed to be equal to the average dipole moment predicted by theLangevin-Debye formula [69] $< \mu_E >= \mu \left(\coth \left(\frac{\mu E}{kT} \right) - \frac{kT}{\mu E} \right)$ which establishes the dependence of the dipole

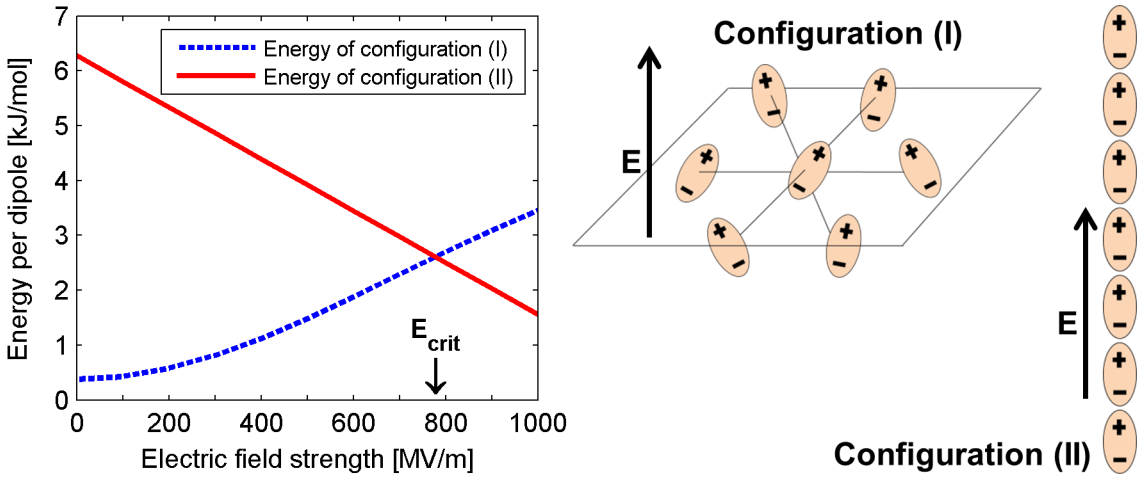

Figure 2.11: Energetic comparison of planar dipole versus vertical configurations. Total energies of dipole configurations (I) and (II). Dashed line is sum of dipole-dipole interaction and dipole-electric field interaction terms for a horizontal layer of oriented dipoles (configuration (I)), solid line is sum of dipole-dipole interaction, dipole-electric field interaction, and the total solvation energy required to remove the dipoles from the bulk water for the vertical stack of dipoles (configuration (II)).

moment on the electric field. The angle of the planar component of the dipole moment is $\mu - \mu_E$ with the planar coordinate axis is drawn from a uniform random distribution of values from 0 to 2π. For the vertical dipole configuration, dipole moment μ is taken to be parallel to E.

We now compute and compare the average energies of configurations (I) and (II) as follows. The total energy for (I) is comprised of two terms: the dipole-dipole interaction (equation A.4 in appendix A), which represents the dominant term of the electrostatic interaction between all of the dipoles, and the energy of the dipole in the external electric field (equation A.3 in appendix A). In addition to these two terms the total energy for configuration (II) includes an estimate of the desolvation energy it would require to remove the dipoles from the bulk water. Goncalves and Stassen [70] estimated the free energy of water solvation with molecular dynamics simulations. We use their result and estimate the free energy required to extract a water molecule from the bulk at -6.7 kcal/mol = -27.8 kJ/mol. Thus the total energy required to extract seven water dipoles from the bulk is approximately -194.5 kJ/mol.

For each of the two configurations we computed these total energies for different values of an external electric field ranging from 0 to 1000 MV/m. Figure 2.11 shows the dependence of the total energy of each of the configurations on the external electric field values. The results presented in the figure demonstrate that we can expect the existence of a critical field value E_{crit} such that creation of configuration (II) becomes more energetically favorable then aligning the dipoles in the bulk water. While obviously we cannot expect this basic model to provide a precise estimate of the E_{crit} value, it illustrates our theory of formation of protrusions and bridges at the water-vacuum interface as a result of electrostatic energy minimization.

2.4 Conclusions

Our simulations and analysis show that at the molecular scale electroporation of a phospholipid bilayer is driven by the restructuring of interfacial water molecules into column-like structures as their dipole moments align with an external electric field. This electric field-driven reorganization of the lipid bilayer is associated with an overall drop in the per-molecule energy for the waters in the growing protrusion. Membrane phospholipids simply follow the bridging water. This view allows significant reduction of the complexity of the analysis of electroporation and opens possibilities for applying well-developed analytical and computational tools to study this problem. Additionally, this insight into the significance of the interfacial water dynamics can facilitate development of new experimental and technological approaches to better control and utilize the process of electroporation.

Note

Chapter 3

Study of Nano-sized Water Droplet in Electric Field

3.1 Introduction

Water's unique combination of small size, near-spherical shape, high polarity, and hydrogen bonding ability give it a large repertoire of structures and intermolecular interactions. These properties are key to water's myriad functions in biochemistry, ranging from stabilizing charged residues and ions to inducing hydrophobic collapse in folding proteins and acting to stabilize reaction intermediates in enzyme active sites. Water's large dipole moment and ability to freely rotate in solution also allows it to interact strongly with external electric fields. At sufficient strengths, external fields can induce "electrofreezing" in water, which has been observed both experimentally [72, 8, 10] and in computer simulations [9, 11]. As presented in Chapter 2, we revealed that the interaction between the water molecules and an external electric field can be the main driver of the initial formation of a transmembrane pore when biological cells are subjected to an electroporation procedure [71].

The systems involved in electroporation modeling in Chapter 2 and, in fact, most modern molecular dynamics (MD) studies of the liquid phase, involve infinite "bulk" systems with periodic boundary conditions. Such simulations require approximate treatment of long-range forces and constrain the structural changes and the spatial heterogeneity in the system. Particularly, past MD researches reported that the use of the Particle Mesh Ewald (PME) method [29] for handling the long-range electrostatic interactions under tin-foil boundary conditions for systems with an external electric field might produce an artifact of overly aligned water dipoles with the field [73, 74]. In contrast, simulations of isolated nanodroplets allow the use of exact long-range forces (for sufficiently small systems) and enable structural change in response to the external electric field. However, this approach introduces some complexities to the simulations. For small droplets the number of water molecules on the surface of the droplet will be comparable to the number of waters in the "bulk" volume. As a result, some aspects of the behavior of a nanodroplet in the electric field will depend directly on the size of the system simulated. A related issue is that different water models may yield different behavior depending on how accurate they are near the water-vacuum interface. In this chapter, we present a detailed study of the effect of an external electric field on a water nanodroplet where we study the systematic dependencies between important parameters.

The relevance of water nanodroplet behavior under the influence of an external electric field considered in this project is two-fold. First, it provides a testing platform for verifying energetic behavior of small clusters of water molecules involved in electroporation models in Chapter 2. Unlike the periodic complex water-vacuum-water or water-lipid-water configurations considered previously, nanodroplets do not require the use of periodic boundary conditions or approximations to the long-range interactions that can complicate the study of the energetics. Results presented here further validate the theory of the water-driven electroporation process proposed.

Second, the behavior of nanodroplets is an important subject in itself relevant to a variety of process including electrospray [3, 75] which advanced into various versatile applications such as electrospinning [4, 5] and Nobel Prize research, Electrospray ionization [6, 7]. It is further relevant to meteorology [1, 2, 32], crop spraying [12], spray painting [13], and inkjet printing [14, 15]. There is extensive literature studying disintegration mechanism of electrified drops [33, 38, 39, 34]. The most closely related study is papers on 10 nm diameter nanodroplets of the small polar organic compound formamide [39]. This paper showed that at a critical strength of an external electric field there was a sharp structural transition of the nanodroplet from a nearly-spherical shape to an elongated nearly ellipsoidal structure accompanied by enhanced reorientation of the molecular dipoles in the direction of the electric field. Also, the critical field strengths required for this transition was found to be close to the prediction of the model developed by Taylor for macroscopic droplets [31] and a new analytical model of free energy terms that yielded predictions of the droplet shape as a function of the applied field was proposed in this paper. Our paper is the first MD study where the questions of the molecular level mechanism of the water droplet evolution and the connection between the droplet size and the electric field strengths are explored. While ignoring the entropy term included in the free energy analysis of the process we manage to derive predictive semi-empirical models using the internal energy of the droplet that provide good prediction of the droplet's shape dynamics.

The goal is to examine molecular level structural and energetic details of the water nanodroplet shape transition. Rather than studying one simulation we execute a spectrum of production runs spanning a range of droplet sizes and electric field strengths with multiple simulations for each configuration. A detailed analysis of these simulations allows us to answer two questions which are key to understanding the behavior of a nanodroplet in electric field. First, we are able to explain the molecular level mechanism behind the droplet shape extension under the influence of the external electric field. Second, based on examining the energetics of the nanodroplet dynamics, we provide a detailed picture of the energetic landscape of the nanodroplet dynamics and develop a quantitative theory that predicts the behavior of the nanodroplet based on its size and the strength of the external electric field.

3.2 MD Simulation Methods

We performed all atom molecular dynamics simulations of all of our water systems using the `GROMACS` program suite, versions 4.0.5, 4.0.7, 4.5.4, and 4.5.5[18,19]. The droplets were simulated in a vacuum with no periodic boundary conditions and with all force field cutoffs set to infinity. For all simulations we used a 1 fs integration time step to improve energy conservation, and the double precision version of `GROMACS` to avoid floating point underflow

errors resulting from the use of infinite force field cutoffs.

Our simulations to analyze nanodroplet behavior can be split into three parts. The first set of simulations modeled the process of nanodroplet stretching from the initial spherical form as increasingly larger external electric fields are applied. The second set of runs started with a nanodroplet in an initially stretched configuration and the field was lowered in a systematic way to determine the minimum field that would support the extended droplet. The first set of simulations allowed us to closely examine the time evolution of relevant parameters during the process stretching. The second set of simulations allowed us to map out the equilibrium states and the energetic landscape. Both sets of simulations were used to determine the critical electric field strength required for transition of the nanodroplet between equilibrium states. Finally, the third set of simulations started with half-stretched nanodroplets and used to confirm the existence of the critical electric field.

3.2.1 Details of nanodroplet stretching simulations

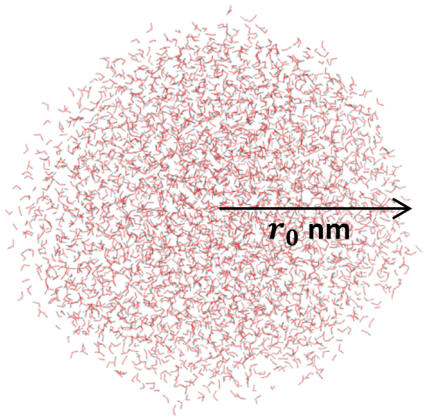

We studied three different sizes of droplets with initial radii of $r_0 = 2$ nm (initially 1125 water molecules), $r_0 = 3$ nm (initially 3789 waters), or $r_0 = 4$ nm (initially 8972 waters). To create the three initial spherical configurations, we first generated a water box with its sides equal to the diameter of droplet. Then a custom `Perl` script was used to remove water molecules outside of spherical shape.

The water models were carefully chosen to thoroughly investigate the behavior of water molecules under the influence of an external electric field. A popular `SPC/E` water model [60] was used for all three sizes of nanodroplets. `SPC/E` is a simple model which consists of one oxygen and two hydrogen atoms with the O-H bond length of 1 Å and the H-O-H bond angle equal to 109.47° and it is known to have good properties such as experimentally confirmed values for density, viscosity, diffusion constant and dielectric permittivity with relatively low computational cost.

In addition to `SPC/E` (bond lengths and angles constrained to be rigid), we simulated 2 nm radius droplet with two other water models to investigate any significant effects of flexibility and polarizability. Flexible `SPC/E` model (flexible bond lengths and bond angles) [62] and the `SW` polarizable water model (rigid bond lengths and angles) [76] were selected. The rigid, anisotropic version of the `SW` water model is chosen because it was found to yield the best agreement with water properties in the original publication of this model.

Equilibration

We first equilibrated all droplets without external electric fields for 1 ns in NVT thermodynamic ensemble which kept three properties, the number of atoms N, the volume V (which was infinite), and the temperature T, conserved during the simulation. Temperature was set to be 300 K using Bussi *et al.*'s stochastic temperature coupling algorithm [65] with a time constant of 0.1 ps.

After the equilibration process, the trajectory was extended for an additional nanosecond and structures were saved every 100 ps to create 10 different starting structures for replicate simulations in an electric field. During the equilibration process, a small number of waters evaporated away from the droplet. Before starting the production simulations, we removed all evaporated water molecules, defined as any monomer, dimer or trimer of water that was more than 1 nm from any other water molecule in the droplet surface. After the evaporated water molecules were removed, the initial structures of the radius of 2 nm systems (initially 1125 waters) had 1119 to 1112 waters (loss of up to 1.15% of the original waters), the 3 nm radius systems (initially 3789 waters) had 3776 to 3766 waters (loss of up to 0.61%), and the 4 nm radius systems (initially 8972 waters) had 8929 to 8919 waters (loss of up to 0.59%).

Production Runs

Starting from these equilibrated structures we ran MD simulations without temperature coupling (i.e. in the NVE ensemble) in the presence of a static electric field with strengths ranging from 0 to 1000 MV/m in the direction we denote as $+Z$. For all 10 replicates of 2, 3, and 4 nm radius `SPC/E` droplets with zero electric field, we found the total energy and temperature are conserved over the 1 ns long simulations. The list of all simulations performed for this study is given in Table 3.1.

Table 3.1: List of stretching simulations performed. For each pair of values (r_0, E), 10 replicates were simulated except for the SPC/E with $(r_0, E) = (4, 800)$ and $(r_0, E) = (4, 900)$ as indicated by an asterisk *. All the simulations ran for 1 ns unless indicated in the parenthesis.

Initial droplet radius, r_0 [nm]	Water model used	Electric fields, E [MV/m]
2	`SPC/E`	0, 100, 200, 300, 400, 500, 600, 700, 800(20 ns), 825(20 ns), 900, 1000
2	`SPC/E` (flexible)	800, 850(20 ns), 875(20 ns), 900(3 ns), 1000(2 ns)
2	`SW` (rigid, anisotropic)	800(2 ns), 825, 850, 900(0.5 ns), 1000(0.5 ns)
3	`SPC/E`	0, 100, 200, 300, 400, 500, 600, 650(10 ns), 700(10 ns), 800, 900
4	`SPC/E`	0, 100, 200, 300, 400, 500, 600, 650, 700, 800*, 900*

3.2.2 Details of nanodroplet collapse simulations

We ran a separate set of simulations of collapsing nanodroplets to investigate the relationship between the size of initial droplet radius and various properties such as the critical electric field strength that causes the shape deformation and the change in internal and surface energies. We created 15 differently sized prolate droplets containing 429 to 8939 `SPC/E` water molecules by carving a water box using the custom `Perl` script.

Table 3.2: List of collapsing simulations performed. For each pair of values $(r0, E)$, 3 replicates were simulated. All the simulations ran for 1 ns.

Initial droplet radius, r_0 [nm]	Water model used	Electric fields, E [MV/m]
1.45	SPC/E	888, 889, 890, 891
1.53		863, 864, 865, 866
1.63		800, 801, 802, 803, 804, 805, 806, 807, 810, 820, 821, 822, 823, 824, 825, 826, 827
1.79		780, 781, 782, 783, 784, 785, 786, 787, 788, 789, 790, 791
1.92		738, 739, 740, 741, 743, 744, 745, 750, 753, 754, 755, 756, 757, 758
2.17		700, 701, 702, 703, 704, 705
2.41		661, 662, 663, 664, 665, 666
2.64		625, 626, 627, 628, 629, 630, 631, 632, 633, 635, 635
2.87		602, 603, 604, 605, 606, 607, 613, 614, 615, 616
3.09		580, 581, 582, 583, 587, 588, 589, 590, 591
3.30		550, 551, 510, 552, 553, 554, 555, 556, 557, 558
3.48		538, 539, 540, 541
3.66		525, 526, 527, 528
3.83		512, 513, 514, 515
4.00		500, 501, 502, 503

Equilibration

We first equilibrated all prolate droplets with an external electric field of 1500 MV/m in the $+Z$ direction. We ran NVT simulations at 300 K using Bussi *et al.*'s stochastic temperature coupling algorithm [65] with a time constant of 0.1 ps. Each simulation was run for 500 ps to align the water molecules to the given field while keeping the shape of the droplet in an extended form. Then the evaporated water molecules were removed from the final simulation structures of all 15 droplets.

Production Runs

The resulting 15 droplet configurations were used as initial structures for the process of finding the critical strength of the electric field which caused the nanodroplet to transition between equilibrium states. We created a `Python` script to control MD runs and to execute the shape checking algorithm. The `Python` program automatically varied the electric field strength between 1000 and 200 MV/m using bisection algorithm and recorded the shape of the droplet for a given electric field. As we will explain in detail in the subsequent sections, we found three regimes of electric field strength, which corresponded to the existence of one or two equilibrium states for the droplet shape depending on the field strength. Since for fields strengths close to the critical value, it can take a while for the droplet to settle down to a stable shape, our code determines if the shape is equilibrated by checking the ratio of the vertical to horizontal axis after every 250 ps of a simulation and automatically extends the MD run by 250 ps if the ratio is not constant over the latest 250 ps time interval.

Once we obtain the rough range of critical strength of the electric field that causes shape extension from the `Python` program, we performed additional simulation to fine-tune the critical value. We varied the field strength in decreasing increments down to 1 MV/m. These simulations were run for 1 ns in NVE ensemble. The list of all refining simulations performed for this study is shown in the Table 3.2.

3.2.3 Details of half stretched nanodroplet simulations

We ran additional set of simulations to confirm the existence of a critical field. We extracted five half-stretched droplets from one of the $r_0 = 2nm$ and $E = 1000$ MV/m simulations and then removed the evaporated water molecules.

Production Runs

We ran 1 ns long NVE simulations. We varied the electric field strength from 740 and 780 MV/m and produced 10 or 20 replicates for all five half-stretched droplets for each different electric field strengthes. The list of all simulations performed for this study is given in the Table 3.3.

Table 3.3: List of half-stretched simulations performed. Five half-stretched droplets extracted from the set #1 of $r_0 = 2$ nm and $E = 1000$ MV/m `SPC/E` simulation. For the electric fields $E = 740$, 750, 770, and 780 MV/m, 10 replicates were simulated. For electric fields $E = 760$ MV/m, 20 replicates were produced. All the simulations ran for 1 ns.

Droplet ID	Extract time point [ps]	Electric fields, E [MV/m]
Drop 1	87	740, 750, 760, 770, 780
Drop 2	88	740, 750, 760, 770, 780
Drop 3	89	740, 750, 760, 770, 780
Drop 4	90	740, 750, 760, 770, 780
Drop 5	91	740, 750, 760, 770, 780

3.3 Results and Discussion

The dynamics described in this section were observed in all simulations. Detailed structural and energetic analysis methods are described in Appendix A. The analysis results are presented in tables in Appendix D in details and the results of some representative simulation will be presented in this section to illustrate characteristic behavior.

To begin with, we show the time evolution of two representative droplet simulations. Figure 3.1 illustrates how the initially spherical droplet of radius 2 nm either assumes a slightly prolate spheroidal form when the electric field strength is set to 700 MV/m (Figure 3.1(a)) or significantly extends if the electric field strength is increased to 900 MV/m (Figure 3.1(b)). We observed that for all sizes of nanodroplet and for all water models, the droplet shape dramatically extended if the applied electric field is high enough to cause this extension. For example, 700 MV/m in Figure 3.1(a) is not hight enough but

(a) Electric field, $E = 700$ MV/m

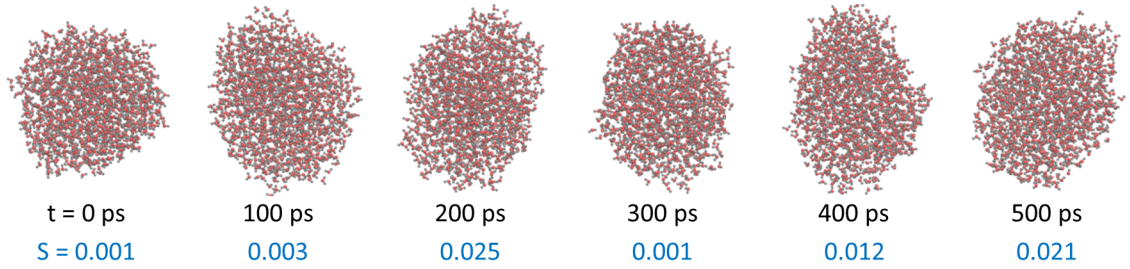

(b) Electric field, $E = 900$ MV/m

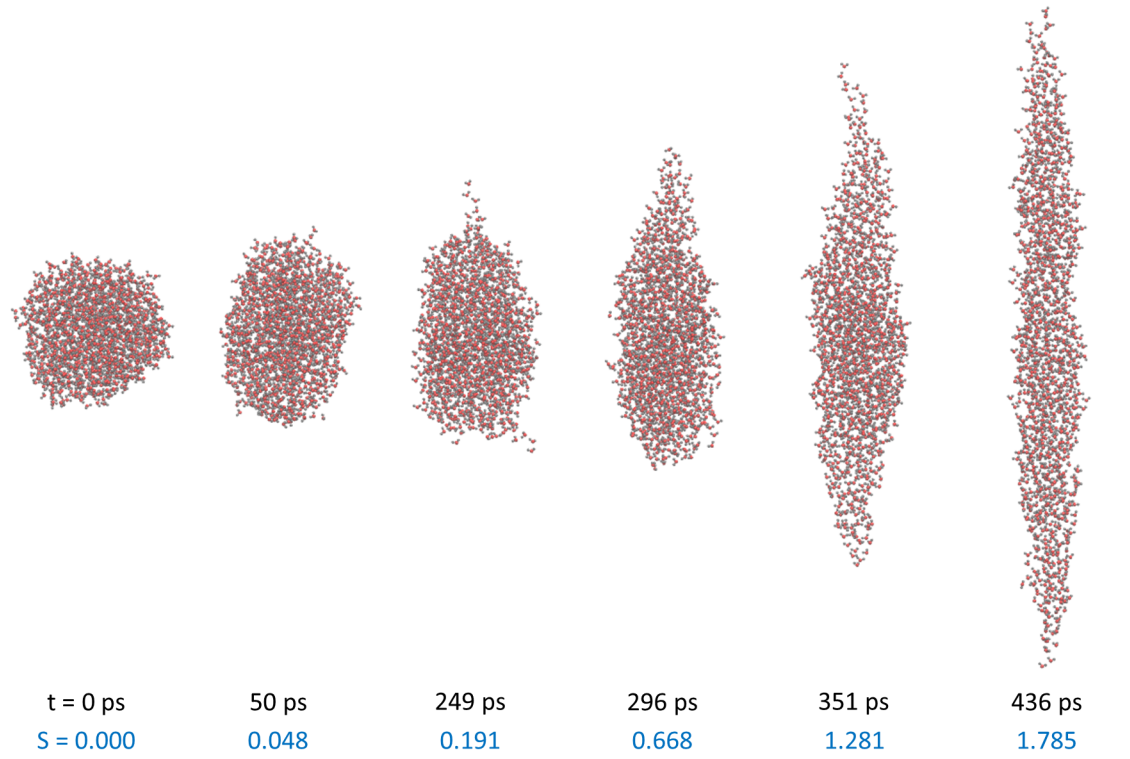

Figure 3.1: Snapshots of the time evolution of droplets of the initial radius, $r_0 = 2$ nm under an external electric field of 3.1(a) $E = 700$ MV/m and 3.1(b) $E = 900$ MV/m. Oxygen atoms are shown in red and hydrogen atoms are shown in gray. The values of shape parameter, S at the indicated times are displayed.

900 MV/m in Figure 3.1(b) is high enough to cause the extension for $r_0 = 2$ nm droplet. We found that the field strength causing this change is varying for different sizes of droplet and slightly different for different water models.

3.3.1 Structural behavior of a nanodroplet in an external electric field

Both the stretching and the collapsing simulations demonstrated that depending on the strength of the electric field the nanodroplet assumes either of the two states – a slightly

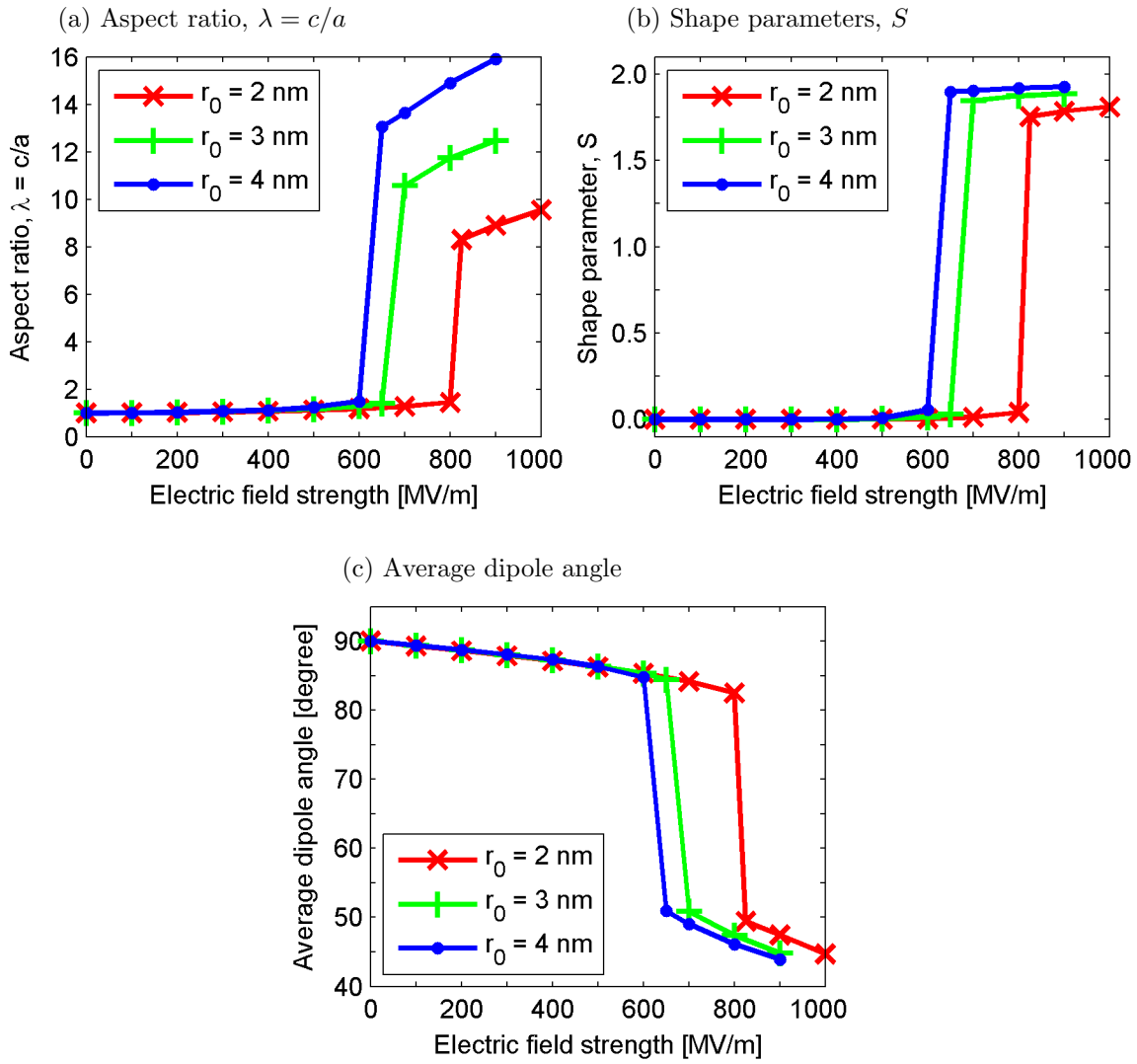

Figure 3.2: Plot of structural data (a) aspect ratio, (b) shape parameters, S, and (c) average dipole angle versus external electric filed strength. Data trend for all three radii, $r_0 = 2$, $r_0 = 3$, and $r_0 = 4$ are shown together.

prolate spheroid or a significantly extended ellipsoid with pointy tips. To simplify characterization of the nanodroplet shape we fit an ellipsoid onto each of the conformations formed by the droplets following the procedure described in the Appendix A. We then quantify the resulting ellipsoid by two parameters: the aspect ratio $\lambda = c/a$ of its major axis c aligned with the electric field to the minor axis a perpendicular to the field direction, and the shape parameter, S. The shape parameter S is derived from the gyration tensor [77] that describes second moments of the position of a collection of particles. It is commonly used to describe the conformations of polymers and proteins [78, 79]. S is bounded between $-1/4$ and 2 and the range of S values corresponds to the shapes of the ellipsoid. The shape is defined to be an oblate ellipsoid for $-1/4 < S < 0$, a sphere for $S = 0$, and a prolate ellipsoid for $0 < S < 2$. See Appendix A for more details.

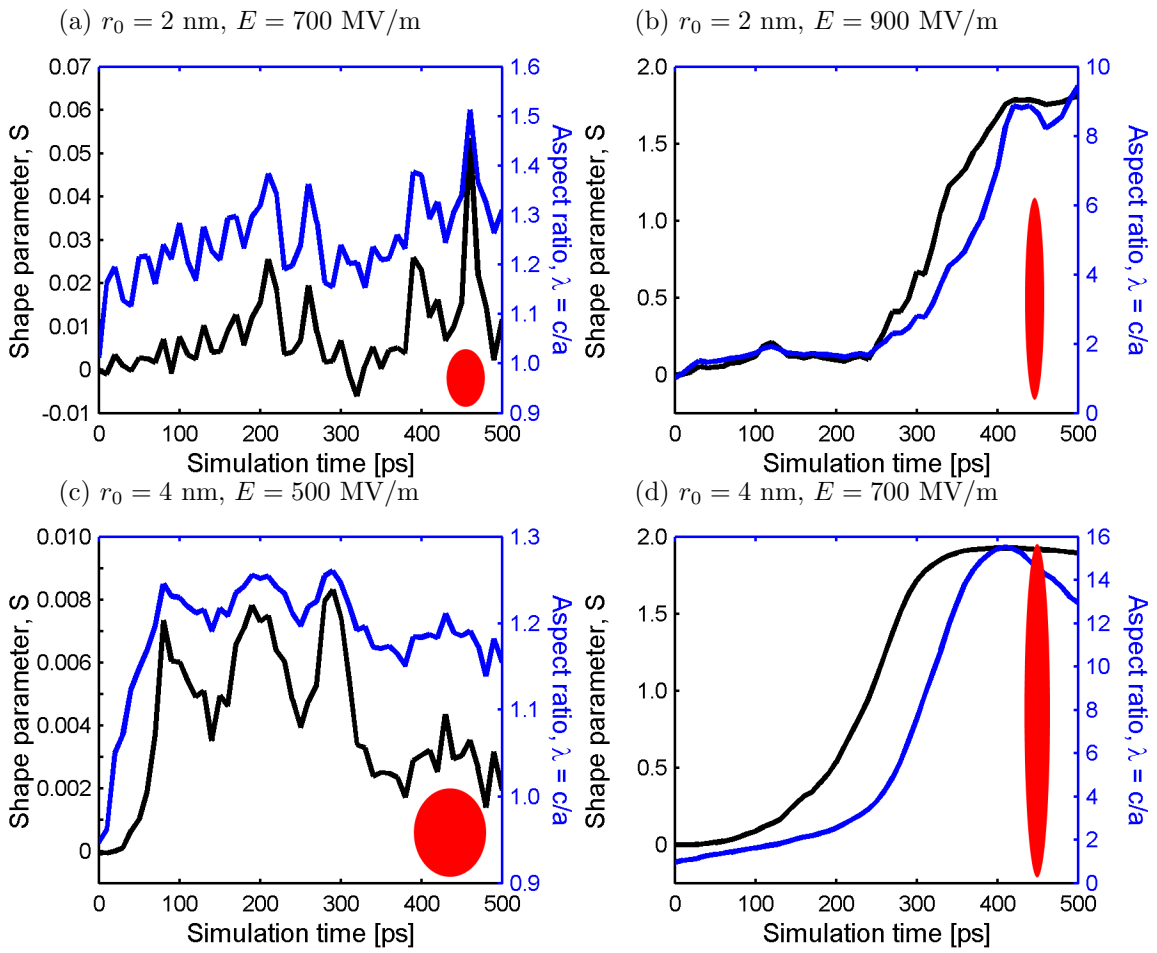

Figure 3.3: Temporal evolution of the shape parameter, S (black line) and the aspect ratio, $\lambda = c/a$ (blue line) for selected representative simulations. Ellipsoid in red are drawn to scale.

If the electric field strength is low and the nanodroplet stretches only slightly we find $\lambda \lesssim 1.5$ and $S \lesssim 0.04$. For the high electric field, the droplet stretches significantly and the lower bounds for the parameters are $\lambda \gtrsim 6$ and $S \gtrsim 1.8$. Table D.1 in the Appendix D provide detailed values of these parameters for the complete range of the initial droplet radii and the electric field strengths simulated. We present three selected structural data from the Table D.1 as plots shown in Figure 3.2. As we can see from Figure 3.2(a) and 3.2(b), it is evident that for a given electric field strength, both of the parameter values λ and S increase as the initial size of the droplet is increased. Also, from Figure 3.2(c), we can observe that the average angle between the water dipoles and the external electric field direction decreases (i.e. more aligned to the field) from $\approx 90°$ to $\approx 40°$ as the droplet shape elongates and further dipoles in a larger droplet are more aligned to the field than the smaller droplet. Overall in Figure 3.2, we can conclude that the shape transition occurs at lower electric field for larger droplet.

Figure 3.3 shows the temporal evolution of the two parameters S and λ for nanodroplets with initial radii 2 nm and 4 nm for low (700 MV/m for 2 nm droplet and 500 MV/m for

4 nm droplet) and high (900 MV/m for 2 nm droplet and 700 MV/m for 4 nm droplet) electric field values. Figures 3.3(a) and 3.3(c) clearly demonstrate how the slight increase in the two parameters for the low electric field is contrasted with the significant growth of these parameters for the high electric field cases shown in Figures 3.3(b) and 3.3(d).

For a certain range of low electric field strengths the nanodroplet in all stretching and all collapsing simulations assumed a slightly extended shape as a final equilibrium. Similarly, for a certain range of high electric fields all of these simulations led to the nanodroplet equilibrating in a significantly extended ellipsoidal shape. However, for range of mid-range electric field strengths, a significant extension of the nanodroplet shape happens only in a portion of the 10 replicate simulations, while in the rest of the runs the nanodroplet stretches only slightly. For example, 6 droplets stretched out of 10 replicates for `SPC/E` 2 nm droplet at 825 MV/m. See Appendix A for details.

These results raise two important questions that are key to fully understanding the dynamics of the nanodroplet extension. First, we need to explain the molecular level mechanism behind the droplet extension. Second, the behavior of the droplet in the critical mid-range of electric field strengths has to be fully understood. We need to develop a quantitative theory that predicts these critical values based on the droplet size and clarifies the dual behavior of the nanodroplet in this range. In the subsequent sections we use detailed energetic analysis to answer both of these questions and propose a new quantitative theory that describes the behavior of the nanodroplets in an external electric field.

3.3.2 Energetic behavior of a nanodroplet in an external electric field

An important advantage of molecular dynamics (that is not always exercised) is that each of the energy components leading to the overall behavior of the simulated system can be measured and analyzed separately. In the case of water in an electric field, this provides an important tool for determining the balance between energetic terms that drives changes in the orientation of the individual water molecules and the overall droplet structure. This is particularly true when small systems, like nanodroplets, are considered.

The primary goal of this paper is to elucidate the energetic details of the dynamics leading to the change in shape and the relationship between this deformation and the strength of the external electric field. To achieve that, we compute and examine the evolution of all components of the total energy of the system. Specifically, we calculate three components of the potential energy described in Appendix A.

- the electrostatic interaction energy, U_{el} (Equation A.1),
- the Lennard-Jones interaction energy, U_{lj} (Equation A.2), and
- the water dipoles and the applied external electric field interaction energy, U_{df} (Equation A.3)

In addition, we compute the water dipole-dipole interaction component U_{dd} (Equation A.4) of the total electrostatic energy U_{el} to determine what percentage of the total electrostatic energy it is responsible for. Finally, we compute the surface energy U_{surf} (Equation A.5), i.e. the energetic cost to increase the exposed surface area of the droplet, which is approximated by multiplying the surface area of the droplet and the surface tension of `SPC/E` water 63.3 mJ/m^2 [80]. The details of the how the energetic components are

calculated is described in Appendix A and the tabulated results can be found in Table D.2 in Appendix D.

Calculating the detailed energetics allows us not only to follow the changes in energy of a particular configuration over time but also compare the various energetic components of different configurations. Thus we can explore the energy landscape of the different configurations of water molecules within a nanodroplet as it takes different shapes. This analysis allows us to determine the most energetically favorable conformations of a collection of waters and the likelihood of a transition between two different nanodroplet shapes. The results establish that the key to the change in the nanodroplet shape is the alignment of water droplets with the external electric field while simultaneous restructuring to minimize unfavorable intermolecular dipole-dipole interactions.

In the presence of an external electric field isolated water molecules can lower their potential energy by aligning their dipole moments parallel to the electric field; however the water dipoles in a spherical droplet cannot align due to the high interaction energy with the adjacent parallel dipoles. If the droplet changes shape to an extended ellipsoid these unfavorable dipole-dipole interactions are largely replaced by favorable stacked parallel dipole-dipole interactions, allowing the water molecules to align with the field. The counterbalancing term is the energetic cost to extend the spherical droplet into an extended ellipsoid, which our analysis shows is about half due to the increased water-vacuum surface area and half due to the reduction in favorable electrostatic interactions within the droplet.

From looking at the energetics as it evolves over time we can understand how the external electric field causes the dipoles to align and the nanodroplet to assume an extended ellipsoidal shape which is more favorable from the perspective of the dipole-dipole and dipole-field interaction energies. Figure 3.4 shows a typical evolution of the energetic components for a nanodroplet of initial radius 4 nm placed in 700 MV/m electric field (value above E_{crit} for this case). All of the graphs are superimposed on the curve representing the change in the shape parameter S to clarify how the shape change is correlated with the changes in the energies. As we can see the deformation into an extended ellipsoid allows the collection of the water molecules to significantly decrease the dipole-dipole (Figure 3.4(a)) and the dipole-field (Figure 3.4(b)) interaction energies. The overall electrostatic energy (Figure 3.4(c)) increases and the total potential energy of the nanodroplet remains nearly constant (Figure 3.4(e)) as we simulate the droplets in NVE ensemble. Figure 3.4(d) demonstrates that the Lennard-Jones energy does not change significantly although it does exhibit a small decrease.

We observed the same structural and energetic behavior for all water models we tested. The only major difference was that the shape extension occurs at a slightly different strength of the electric field. In addition to explaining the overall behavior of the nanodroplet, calculating all of the energetic components (see Table D.2 and Table D.3 in Appendix D) helps us predict the critical mid-range strengths of the electric field and the nanodroplet dynamics for this range explained in the following subsection.

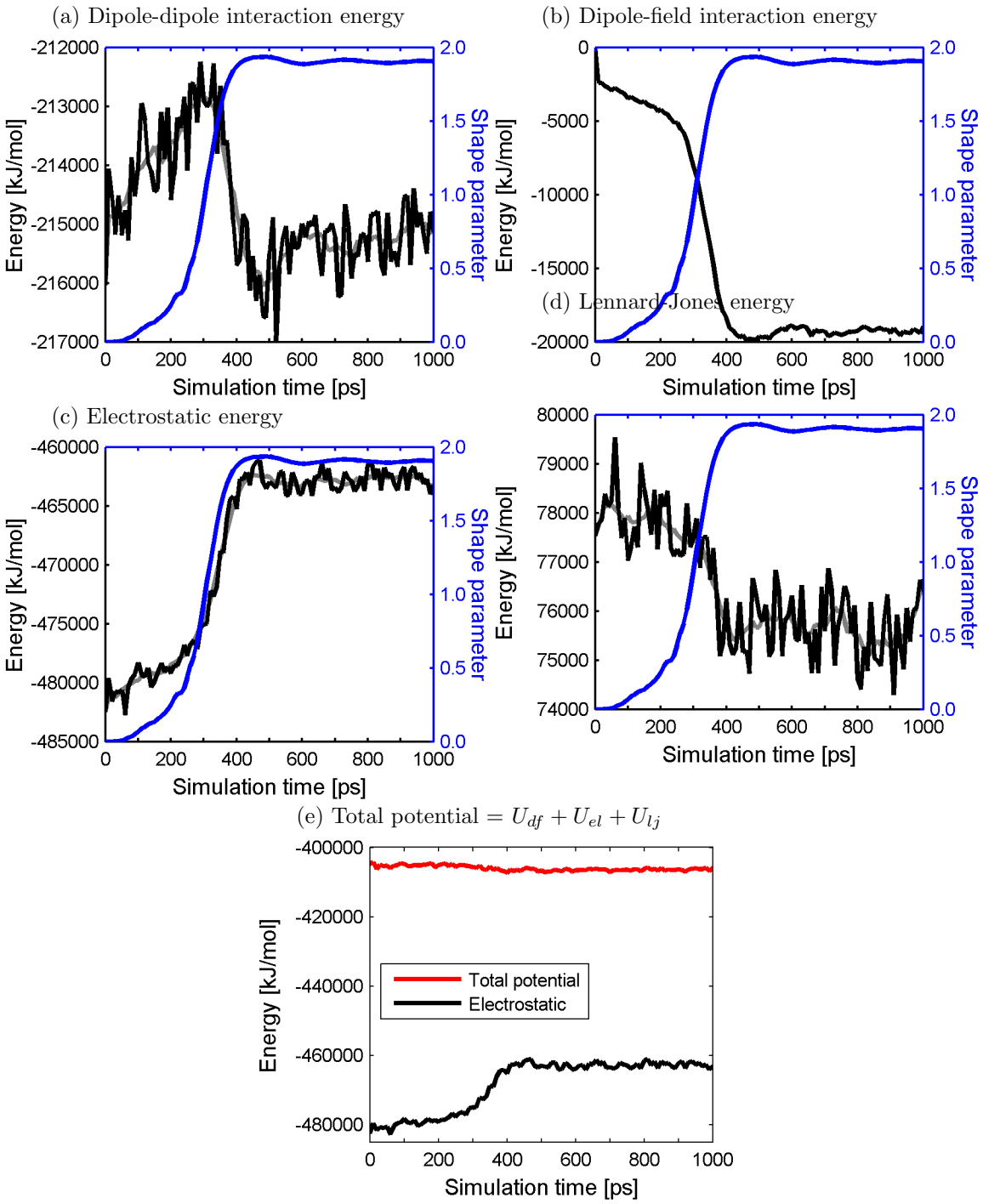

Figure 3.4: Temporal evolution of the energetic components for a sample droplet with the initial radius $r_0 = 4$ nm and the electric field strength $E = 700$ MV/m. Grey line is a smoothed version using 2 ps moving average. Note that the total potential energy is conserved throughout the simulation.

3.3.3 Nanodroplet equilibria at the critical strengths of the electric field

A large body of experimental and theoretical research has been dedicated to the study of macroscopic droplets ($\gtrsim \mu$m) under the influence of external electric field since the seminal papers by Zeleny [81, 82] and G. I. Taylor [31]. The basic theory first proposed by Taylor in 1964 [31] assumes that the droplet reaches an equilibrium shape of a prolate spheroid and allows the calculation of the corresponding aspect ratio $\lambda = c/a$ by balancing the electrostatic force, the surface tension and the fluid pressure at the surface of the droplet. The resulting prediction yields the following relationship between λ, the electric field strength E, the surface tension T and the radius of the initial spherical droplet r_0.

$$E\sqrt{\frac{r_0}{T}} = \Phi(\lambda) = \sqrt{8\pi}\lambda^{(-4/3)}\sqrt{2-\lambda^{-1}-\lambda^{-3}}\left(\frac{1}{2(1-\lambda^{-2})^{3/2}}\ln\frac{1+\sqrt{1-\lambda^{-2}}}{1-\sqrt{1-\lambda^{-2}}} - \frac{1}{1-\lambda^{-2}}\right) \quad (3.1)$$

Linear stability analysis that Taylor based on the work by Rayleigh [30] showed that if the electric field strength is greater than the critical value E^T_{crit} the spheroidal shape determined from equation 3.1 is unstable.

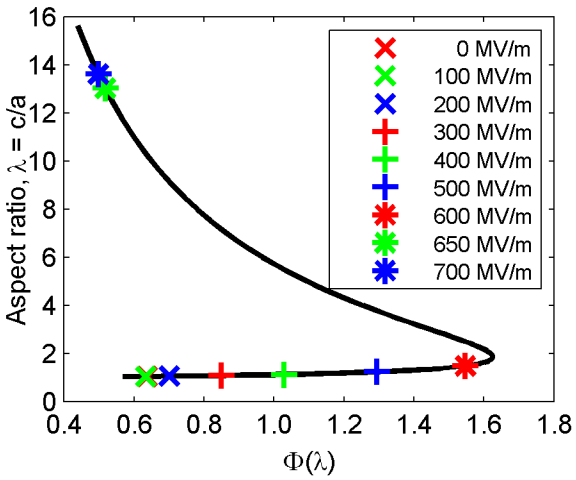

Figure 3.5: Comparison of Taylor theory, Equation 3.1, (black solid line) with the simulation data (colored symbols) of the droplets with $r_0 = 4$ nm.

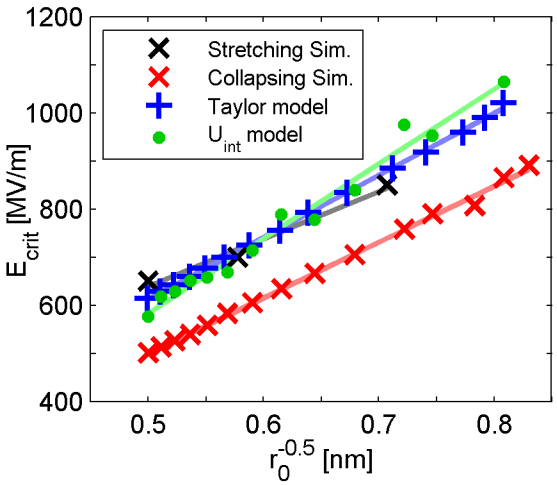

Figure 3.6: Plot of critical electric fields. We compare the prediction by Taylor model (Equation 3.1) and the prediction by U_{int} model (Equation 3.2) with the MD simulation data obtained from stretching and collapsing simulations.

Following this analysis [31] we can estimate the value of E^T_{crit} using our nanodroplet stretching simulations by finding the strength of the electric field below which the ratio λ does not exceed the value 1.86. Just as it was also found by Luedtke *et al.* for formamide droplets [39], the theoretical and computational results closely match (see Figure 3.5 and 3.6). Note, however, that it is difficult to make this estimate with a high precision since

for the field strengths near the critical value the behavior of the droplet is very sensitive to the electric field and some of the simulations show a significantly extended droplet while others follow the Taylor's shape prediction. In fact, if we try to make the same estimate of E^T_{crit} using collapsing droplet simulations, we find that our prediction now systematically differ from the Taylors value as shown in Figure 3.6. To examine the behavior further we use empirical relationships derived from the simulations along with the following energetic arguments.

The favorable drop in potential energy for the N_w randomly oriented waters, each with a dipole moment μ, to align with the electric field E with an orientation of θ_i degrees for an ith molecule is:

$$\Delta U_{df} = -E \times \mu \times \sum_{i=1}^{N_w} \cos(\theta_i).$$

Note that for the non-polarizable water models used, the dipole moment is a constant. Using the simulation data we can find a relationship between $\Theta = \sum_{i=1}^{N_w} \cos(\theta_i)$ and the major to minor axes ratio λ as shown in Figrure 3.7(a). The simulation data can be approximated well by a quadratic function $\Theta = A\lambda^2 + B\lambda + C$, with the parameter values for A, B, C and the small variation in these values given in Table 3.4. Then the change in the potential energy for the dipole-field interaction can then be expressed as a function of λ:

$$\Delta U_{df} = -E \times \mu \times (\lambda^2 + B\lambda + C)$$

We can also use the simulation data to determine the relationship between λ and the change in the internal energy ΔU_{int} as shown in Figrure 3.7(b). The internal energy ΔU_{int} is simply the sum of the electrostatic, U_{el} and the Lennard-Jones, U_{lj} interaction energies. We find that the following power function given below best fits this relationship with narrowly ranging parameter values of M and D shown in Table 3.4.

$$\Delta U_{int} = D\lambda^M$$

Table 3.4: Empirically fitted parameters.

	data fitting parameters	mean ± standard deviation
ΔU_{df}	A	-8.19 ± 0.63
	B	163.31 ± 6.24
	C	-43.99 ± 15.08
ΔU_{int}	D	-48800 ± 229
	F	-0.03 ± 0.0012

Combining the two expressions and examining the total change of energy $\Delta U_p = \Delta U_{df} + \Delta U_{int}$ with respect to λ for different values of E we find that for a range of electric field strengths it is possible to have a double well potential profile in the energy shown in Figure 3.7(c). This profile of the energetic curve in the mid-range of the electric field values close to the critical field explains why the droplets in some of the simulations for particular E field values remain only slightly extended, while others settle to a highly extended shape. The height of the energy barrier between the two states depends on E and determines the

time scale for the droplet to find a configuration corresponding to a global, rather than local, minima in the energy (see below).

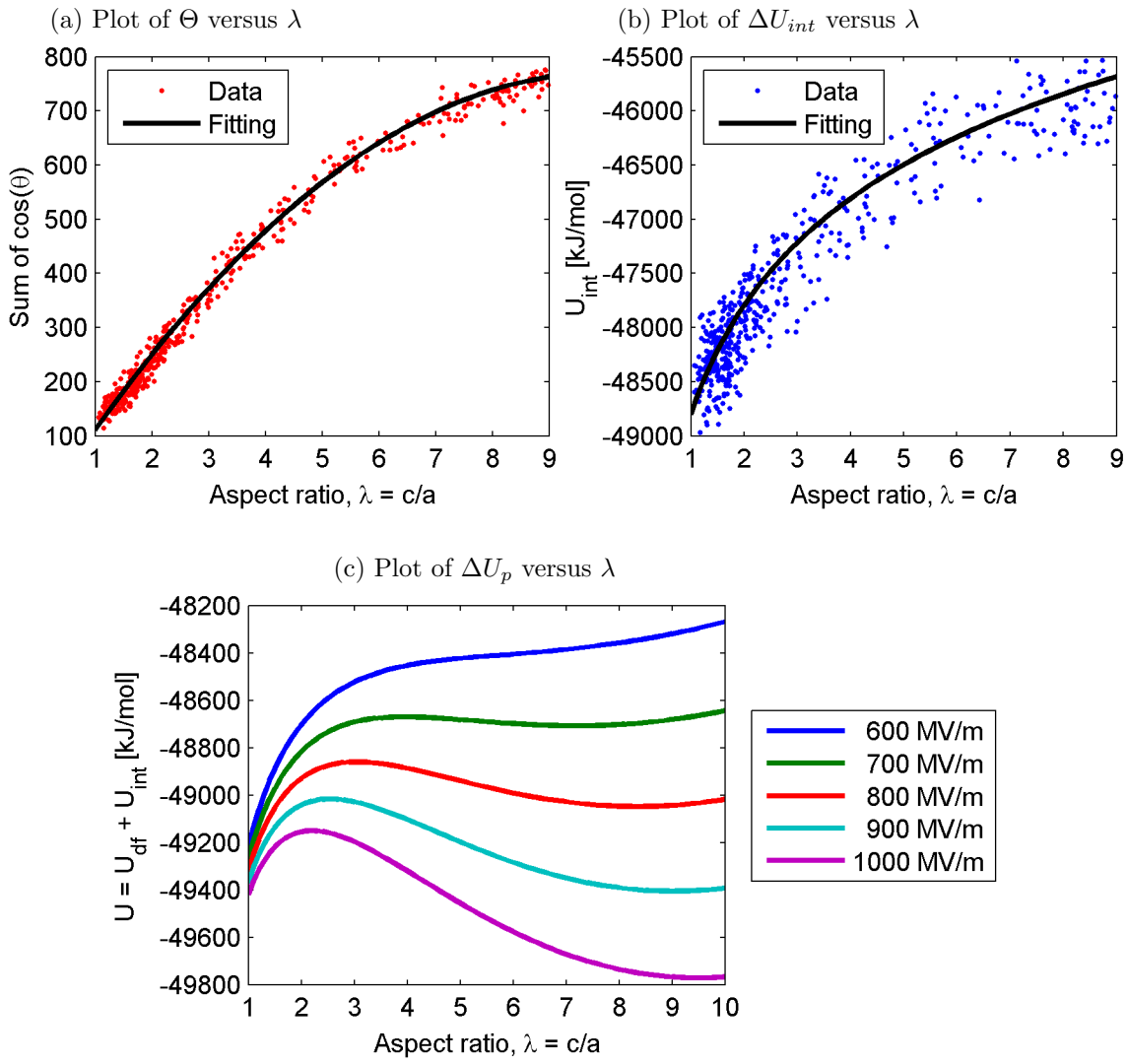

Figure 3.7: Plot of energy components of simulation data and their fitting curves against the aspect ratio, λ. (a) is plot of $\Theta = \sum_{i=1}^{N_w} \cos(\theta_i)$ data with quadratic function fitting curve, (b) is plot of $\Delta U_{int} = U_{el} + U_{lj}$ data with power function fitting curve, and (c) is plot of the potential energy, $\Delta U_p = \Delta U_{df} + \Delta U_{int}$ where U_{df} and U_{int} are obtained from the fitted curves in (a) and (b), respectively.

The analytic expression for the $\Delta U_p = \Delta U_{df} + \Delta U_{int}$ along with the empirically derived parameter values can also be used to find the maximum field strength for which there is only one slightly prolate spheroidal global equilibrium state and the minimum field strength for which there is only one global equilibrium state as a significantly extended ellipsoid. We can also determine the value of E for which both of the equilibria correspond to the same energy level (see below).

Using a similar combination of the empirical estimates and theoretical arguments we can

also find how the critical value of the electric field E_{crit} required for elongation of a droplet varies with the initial radius of the droplet r_0. Empirically we found that the average dipole angle θ (i.e. angle from the field direction to water dipole, see Appendix A) at the critical field strength is homogeneous across the entire extended droplet (at least for the small droplets considered in this study). Thus we can approximate the favorable drop in potential energy with:

$$\Delta U_{df} = -E \times \mu \times N_w \times \cos(\theta)$$

From simulation data plot presented in Figure 3.8(a), we find that the $\cos(\theta)$ is linearly dependent on the initial droplet radius r_0 with

$$\cos(\theta) = -a_1 \times r_0 + a_2, \qquad a_1 = 0.0588 \quad \text{and} \quad a_2 = 0.6337.$$

The critical field at which the droplet extends occurs when the energetic advantage of aligning with the field ΔU_{df} is greater than the cost in internal energy ΔU_{int} to elongate the droplet, i.e. when

$$E \times \mu \times N_w \times \cos(\theta) \geq \Delta U_{int}.$$

Hence,

$$E_{crit} = \frac{\Delta U_{int}}{\mu \times N_w \times \cos(\theta)} \tag{3.2}$$

Using the fact that the number of water molecules is proportional to $1/r_0^3$, i.e. $N_w \propto r_0^{-3}$ and the fitted relationship shown in Figure 3.8(a), i.e. $\cos(\theta) = -a_1 \times r_0 + a_2$, we can obtain

$$E_{crit} \approx \frac{\Delta U_{int}}{\mu \times N_w \times (-a_1 \times r_0 + a_2)} \propto \frac{\Delta U_{int}}{a_2 r_0^3 - a_1 r_0^4}.$$

Empirically, for the fitted values of a_1 and a_2 and for r_0 between 1.4 nm and 4.0 nm, we find

$$a_2 r_0^3 - a_1 r_0^4 \propto r_0^{2.67}.$$

Then we can yield an overall scaling

$$E_{crit} \propto \frac{\Delta U_{int}}{r_0^{2.67}}.$$

Fitting the change in internal energy to a power function of r_0, yields the following empirical relationship shown in Figure 3.8(b):

$$\Delta U_{int} \propto r_0^{2.05}$$

As we can see in Figure 3.8(c), plotting the change in internal energy, ΔU_{int} versus the change in the nanodroplet surface area, ΔSA, we find a nearly perfect linear relationship with a proportionality constant close to 1, indicating that the change in surface energy can be used to predict the energetic cost of elongating the droplet.

Combining the obtained results we find the following prediction of the critical field variation with respect to r_0:

$$E_{crit} \propto \frac{\Delta U_{int}}{r_0^{2.67}} \approx \frac{r_0^{2.05}}{r_0^{2.67}} = \frac{1}{r_0^{0.61}}$$

This empirically derived relationship between E_{crit} and r_0 is very similar to that from Taylor's model:

$$E_{crit} \propto \frac{1}{r_0^{0.5}}$$

Note that U_{int} prediction we just derive (green marks) closely overlap with Taylor's prediction (blue marks) in Figure 3.6. Instead of complex free energy analysis, we derive a semi-empirical model using the internal energy of the droplet that can be easily calculated from simulation trajectories.

(a) Plot of $\cos(\theta)$ versus r_0

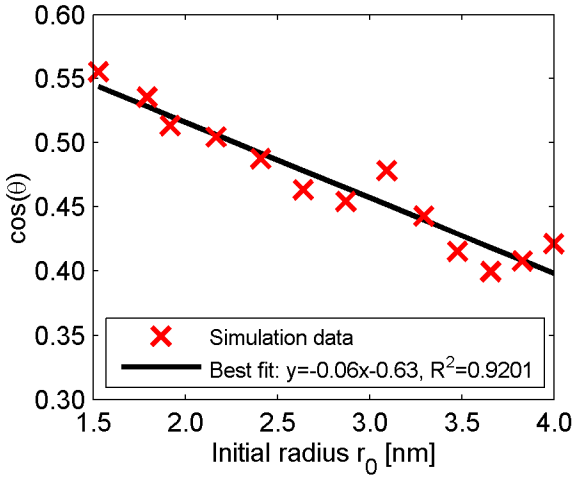

(b) Plot of $\log(\Delta U_{int})$ versus $\log(r_0)$

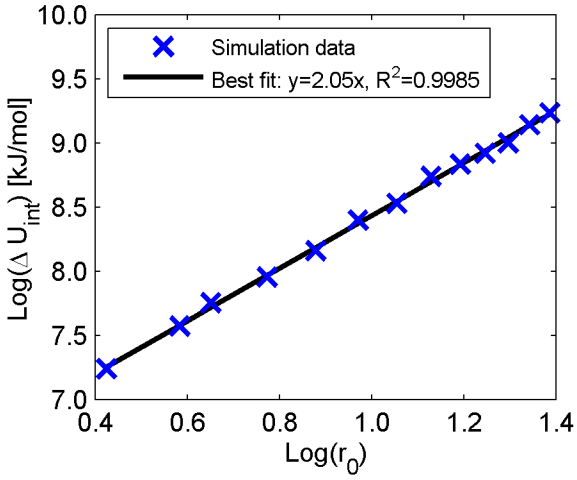

(c) Plot of $\log(\Delta U_{int})$ versus $\log(\Delta SA)$

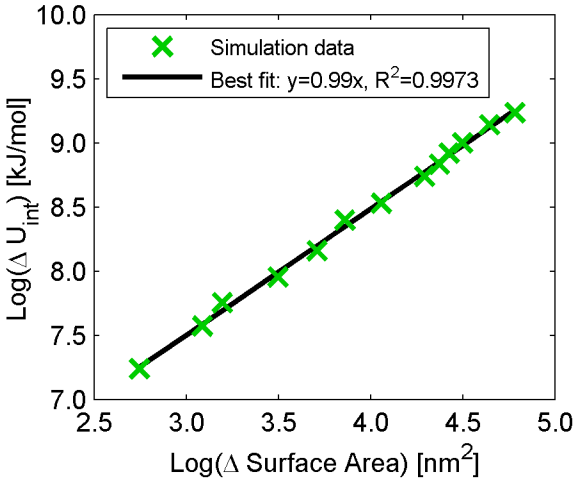

Figure 3.8: Plot of three relationships with linear fitting used for U_{int} model 3.2 derivation. (a) is plot of $\cos(\theta)$ against r_0 with linear fit, (b) is plot of ΔU_{int} against r_0 with linear fit in $\log - \log$ scale, and (c) is plot of ΔU_{int} against Δ Surface Area (SA) with linear fit in $\log - \log$ scale.

3.3.4 Evidence two equilibrium status (no metastable stage)

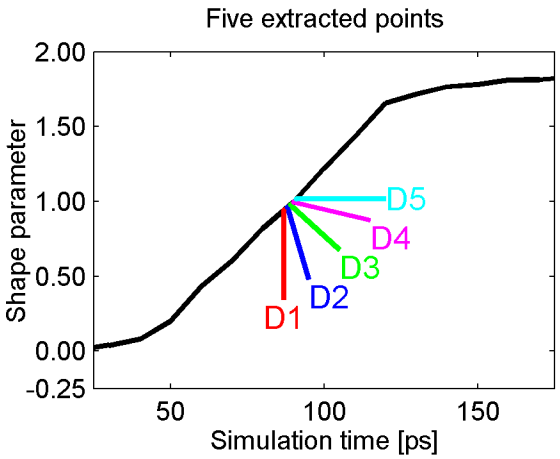

Figure 3.9: Five droplets lie near shape parameter, $S \approx 0.9$ are extracted. Drop 1 at 87 ps, Drop 2 at 88 ps, Drop 3 at 89 ps, Drop 4 at 90 ps, Drop 5 at 91 ps.

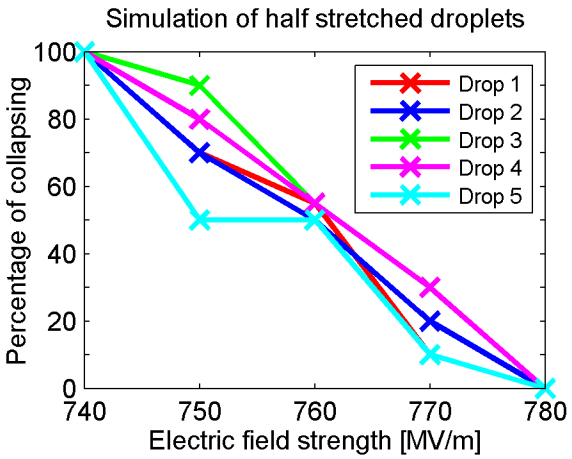

Figure 3.10: Percentage of collapsed droplets after 1 ns simulation with the external field varying from 740 MV/m to 780 MV/m are plotted. At 760 MV/m, all five half stretched droplets have 50% collapsing rate, i.e. 50% extending rate.

The third set of simulations is simulations of half stretched nanodroplets. As explained in the method section, we extracted five half stretched droplets from one of r_0 simulations as shown in Figure 3.9. We ran it for 1 ns with the external field range from 740 MV/m to 780 MV/m. As we can see in Figure 3.6, for the 2 nm initial radius droplets we used to extract the half stretched droplets, 740 MV/m is approximately the lower bound of E_{crit} observed from collapsing simulations (Table 3.2) and 780 MV/m is approximated the upper bound of E_{crit} observed from stretching simulation (Table 3.1). We produced 10 to 20 replicates to investigate whether the electric field that causes half of droplets extends and half of them collapses exists. As we see in Figure 3.10, for all half stretched droplets, 50% of droplet collapsed to near sphere shape and other 50% of droplet extended to long prolate at 760 MV/m. This result explains that the actual critical electric field exist in between the E_{crit} found from the stretching simulations (black marks) and the E_{crit} found from the collapsing simulations (red marks) in Figure 3.6. We argue that there is no meta-stable stage. If enough time is allowed, a droplet will either stay in a slight prolate spheroid form or in a long extended prolate.

3.3.5 Evidence for energetic barrier to droplet extension

Except for the very largest applied electric fields, there is a time delay between the time the electric field is applied and the extension of the droplet. The average time to extension monotonically decreases with increasing field, as shown in Table D.1 in Appendix D, but there is considerable variation in the time to extension between replicate simulations as shown in Figure 3.11.

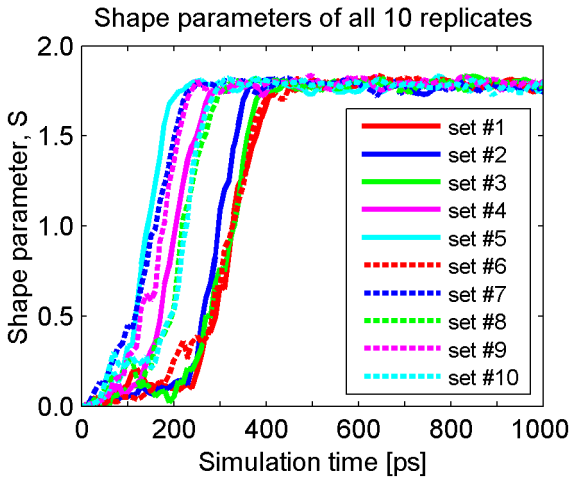

Figure 3.11: Plot of shape parameters of all 10 replicates of $r_0 = 2$ nm radius, SPC/E droplet with the external electric field strength, $E = 900$ MV/m.

The magnitude of the barrier can be estimated from the empirical equations for ΔU_{df} and ΔU_{int} derived previously. Since ΔU_{int} is proportional to the droplet surface area (see Figure 3.8(c)) which is a function of the aspect ratio $\lambda = c/a$, we can plot the total energy change versus the "reaction rate" for droplet extension, λ, for any specified electric field. A set of such plots is shown in Figure 3.7(c) for the $r_0 = 2$ nm droplets with field strengths of 600 - 1000 MV/m in increments of 100 MV/m. As this figure shows, for the lowest electric field the energy monotonically increases as the droplet extends away from the near-spherical ground state. As the field is increased, a second minimum appears at large λ corresponding to the extended droplet form.

At all fields there is an energy barrier that decreases with increasing field. If the system follows simple Arrhenius kinetics then the rate follows the equation:

$$\text{Reaction rate constant} \sim \frac{1}{t_{extend}} = a \exp\left(-\frac{\Delta U}{kT}\right)$$

where t_{extend} is the average time to droplet extension , ΔU is "activation energy" which is the calculated barrier (from Figure 3.7(c)) to droplet extension per water molecule, k is Boltzmann's constant, and T is temperature.

Take log on both side yield

$$\log\left(\frac{1}{t_{extend}}\right) = -\frac{1}{kT}\Delta U + \log(a).$$

Hence, a plot of the $\log(1/t_{extend})$ versus the calculated barrier ΔU should give straight lines if the rate is dominated by simple barrier crossing. These resulting graphs for the three different droplet sizes, shown in Figure 3.12. The rates for droplet extension do appear to follow Arrhenius-like kinetics considering the fact that only 3-4 data points are used to form these reasonably linear and parallel lines.

A complexity in describing the reactions involving large groups of molecules is identifying the correct "reaction rate" since the transition from the spherical to the extended form involves the coordinated motion of many interacting waters. Since the slope found from this Arrhenius plot should be $-1/kT = -0.4$ but the average of three slopes in Figure 3.12 is -12.7, we can estimate the number of waters follows Arrhenius "reaction rate" to be approximately 32 waters.

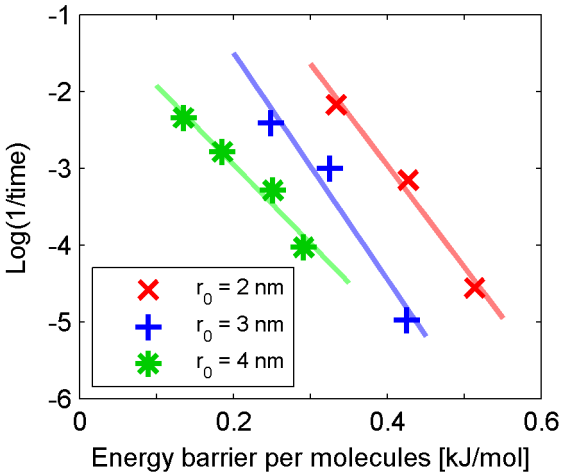

Figure 3.12: Plot of $\log(1/t_{extend})$ against energy barrier per molecule for the three different sizes of droplet.

3.4 Simple continuum dipole-dipole interaction energy model

A physics-based continuum model for calculating a dipole-dipole interaction energy in a prolate is created. Consider two dipoles in electric field like shown in Figure 3.13.

Figure 3.13: System of two dipole moments in electric field

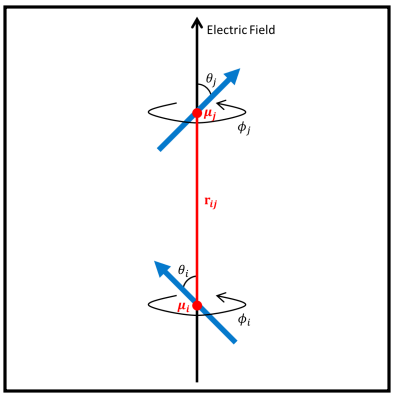

The electric field $\mathbf{E}_i$ from i-th dipole is given by

$$\mathbf{E}_i(\mathbf{r}) = -\frac{1}{4\pi\epsilon_0\|\mathbf{r}-\mathbf{r}_i\|^3}\left[\boldsymbol{\mu}_i - 3\frac{\boldsymbol{\mu}_i\cdot(\mathbf{r}-\mathbf{r}_i)(\mathbf{r}-\mathbf{r}_i)}{\|\mathbf{r}-\mathbf{r}_i\|^2}\right]$$

The interaction energy, U_{dd} between two permanent electric dipoles is proportional to the product of the two dipole moments and depends on their relative orientation.

$$
\begin{aligned}
U_{dd} &= -\boldsymbol{\mu}_j \cdot \mathbf{E}_i(\mathbf{r}_j) \\
&= -\frac{1}{4\pi\epsilon_0 \|\mathbf{r}-\mathbf{r}_i\|^3}\left[\boldsymbol{\mu}_i \cdot \boldsymbol{\mu}_j - 3\frac{\boldsymbol{\mu}_i \cdot (\mathbf{r}_j-\mathbf{r}_i)(\mathbf{r}_j-\mathbf{r}_i)\cdot \boldsymbol{\mu}_j}{\|\mathbf{r}-\mathbf{r}_i\|^2}\right] \\
&= \frac{1}{4\pi\epsilon_0 r_{ij}^3}\left[\boldsymbol{\mu}_i \cdot \boldsymbol{\mu}_j - 3\frac{\boldsymbol{\mu}_i \cdot (\mathbf{r}_j-\mathbf{r}_i)(\mathbf{r}_j-\mathbf{r}_i)\cdot \boldsymbol{\mu}_j}{r_{ij}^2}\right] \\
&= \frac{1}{4\pi\epsilon_0 r_{ij}^5}\left[r_{ij}^2 \boldsymbol{\mu}_i \cdot \boldsymbol{\mu}_j - 3(\boldsymbol{\mu}_i \cdot \mathbf{r}_{ji})(\boldsymbol{\mu}_j \cdot \mathbf{r}_{ji})\right]
\end{aligned}
$$

where two permanent water dipoles are $\boldsymbol{\mu}_i$ and $\boldsymbol{\mu}_j$ and $(\mathbf{r}_j - \mathbf{r}_i) = \mathbf{r}_{ji}$ is the vector between the two dipoles and r_{ij} is the distance between them. The constant ϵ_0 is the vacuum permittivity.

Write dipole in spherical coordinates, $\boldsymbol{\mu} = (\mu\sin(\theta)\cos(\phi), \mu\sin(\theta)\sin(\phi), \mu\cos(\theta))$. μ is the magnitude of dipole moment and θ is the polar angle and ϕ is the azimuthal angle of dipole moment.

Then the dot products, $\boldsymbol{\mu}_i \cdot \boldsymbol{\mu}_j$ and $\boldsymbol{\mu}_i \cdot \mathbf{r}_{ji}$ and $\boldsymbol{\mu}_j \cdot \mathbf{r}_{ji}$ become

$$
\begin{aligned}
\boldsymbol{\mu}_i \cdot \boldsymbol{\mu}_j &= \mu_i \sin(\theta_i)\cos(\phi_i)\mu_j \sin(\theta_j)\cos(\phi_j) + \mu_i \sin(\theta_i)\sin(\phi_i)\mu_j \sin(\theta_j)\sin(\phi_j) + \mu_i \cos(\theta_i)\mu_j \cos(\theta_j) \\
&= \mu_i\mu_j\left[\sin(\theta_i)\sin(\theta_j)\cos(\phi_i)\cos(\phi_j) + \sin(\theta_i)\sin(\theta_j)\sin(\phi_i)\sin(\phi_j) + \cos(\theta_i)\cos(\theta_j)\right] \\
&= \mu^2\left[\sin(\theta_i)\sin(\theta_j)\cos(\phi_i)\cos(\phi_j) + \sin(\theta_i)\sin(\theta_j)\sin(\phi_i)\sin(\phi_j) + \cos(\theta_i)\cos(\theta_j)\right]
\end{aligned}
$$

$$
\begin{aligned}
\boldsymbol{\mu}_i \cdot \mathbf{r}_{ji} &= \mu_i \times r_{ij} \times \cos(\theta_i) \\
&= r\mu\cos(\theta_i)
\end{aligned}
$$

$$
\begin{aligned}
\boldsymbol{\mu}_j \cdot \mathbf{r}_{ji} &= \mu_j \times r_{ij} \times \cos(\theta_j) \\
&= r\mu\cos(\theta_j)
\end{aligned}
$$

Note that the magnitude of two water dipoles are the same, $\mu_i = \mu_j$, so both of them are simply denoted by μ. In addition, the distance between two dipoles, r_{ij} is simply denoted by r.

Hence,

$$
\begin{aligned}
U_{dd} &= \frac{1}{4\pi\epsilon_0 r^5}\left[r^2\mu^2\left(\sin\theta_i\sin\theta_j\cos\phi_i\cos\phi_j + \sin\theta_i\sin\theta_j\sin\phi_i\sin\phi_j + \cos\theta_i\cos\theta_j\right) - 3r^2\mu^2\cos\theta_i\cos\theta_j\right] \\
&= \frac{r^2\mu^2}{4\pi\epsilon_0 r^5}\left[\sin\theta_i\sin\theta_j\cos\phi_i\cos\phi_j + \sin\theta_i\sin\theta_j\sin\phi_i\sin\phi_j + \cos\theta_i\cos\theta_j - 3\cos\theta_i\cos\theta_j\right] \\
&= \frac{\mu^2}{4\pi\epsilon_0 r^3}[\underbrace{\sin\theta_i\sin\theta_j\cos\phi_i\cos\phi_j}_{\text{part A}} + \underbrace{\sin\theta_i\sin\theta_j\sin\phi_i\sin\phi_j}_{\text{part B}} - \underbrace{2\cos\theta_i\cos\theta_j}_{\text{part C}}]
\end{aligned}
$$

3.4.1 Averaging Dipole-dipole interaction energy

Averaging the dipole-dipole interaction energy, $\overline{U_{dd}}$ over the polar angle θ and the azimuthal angle ϕ is

$$\overline{U_{dd}} = \frac{\iiiint U_{dd}(\theta_i, \theta_j, \phi_i, \phi_j)\, P(\theta_i)P(\theta_j)P(\phi_i)P(\phi_j)\, d\theta_i\, d\theta_j\, d\phi_i\, d\phi_j}{\iiiint P(\theta_i)P(\theta_j)P(\phi_i)P(\phi_j)\, d\theta_i\, d\theta_j\, d\phi_i\, d\phi_j}$$

The polar angle θ follows the exponential distribution[1] and the azimuthal angle ϕ follows the uniform distribution.

$$P(\theta) = \begin{cases} \lambda e^{-\lambda\theta}, & \theta \geqslant 0 \\ 0, & \theta < 0. \end{cases}$$

$$P(\phi) = \begin{cases} \frac{1}{2\pi}, & 0 \leqslant \phi \leqslant 2\pi \\ 0, & \text{otherwise.} \end{cases}$$

Hence, the average dipole-dipole interaction energy, $\overline{U_{dd}}$ over the polar angle θ and the azimuthal angle ϕ is

$$\overline{U_{dd}} = \underbrace{\frac{\int_0^{2\pi}\int_0^{2\pi}\int_0^{\pi}\int_0^{\pi} \frac{\mu^2}{4\pi\epsilon_0 r^3}\left[\sin\theta_i \sin\theta_j \cos\phi_i \cos\phi_j\right]\ \lambda e^{-\lambda\theta_i}\lambda e^{-\lambda\theta_j}\frac{1}{2\pi}\frac{1}{2\pi}\, d\theta_i\, d\theta_j\, d\phi_i\, d\phi_j}{\int_0^{2\pi}\int_0^{2\pi}\int_0^{\pi}\int_0^{\pi}\ \lambda e^{-\lambda\theta_i}\lambda e^{-\lambda\theta_j}\frac{1}{2\pi}\frac{1}{2\pi}\, d\theta_i\, d\theta_j\, d\phi_i\, d\phi_j}}_{\text{part A}}$$

$$+ \underbrace{\frac{\int_0^{2\pi}\int_0^{2\pi}\int_0^{\pi}\int_0^{\pi} \frac{\mu^2}{4\pi\epsilon_0 r^3}\left[\sin\theta_i \sin\theta_j \sin\phi_i \sin\phi_j\right]\ \lambda e^{-\lambda\theta_i}\lambda e^{-\lambda\theta_j}\frac{1}{2\pi}\frac{1}{2\pi}\, d\theta_i\, d\theta_j\, d\phi_i\, d\phi_j}{\int_0^{2\pi}\int_0^{2\pi}\int_0^{\pi}\int_0^{\pi}\ \lambda e^{-\lambda\theta_i}\lambda e^{-\lambda\theta_j}\frac{1}{2\pi}\frac{1}{2\pi}\, d\theta_i\, d\theta_j\, d\phi_i\, d\phi_j}}_{\text{part B}}$$

$$- \underbrace{\frac{\int_0^{2\pi}\int_0^{2\pi}\int_0^{\pi}\int_0^{\pi} \frac{2\mu^2}{4\pi\epsilon_0 r^3}\left[\cos\theta_i \cos\theta_j\right]\ \lambda e^{-\lambda\theta_i}\lambda e^{-\lambda\theta_j}\frac{1}{2\pi}\frac{1}{2\pi}\, d\theta_i\, d\theta_j\, d\phi_i\, d\phi_j}{\int_0^{2\pi}\int_0^{2\pi}\int_0^{\pi}\int_0^{\pi}\ \lambda e^{-\lambda\theta_i}\lambda e^{-\lambda\theta_j}\frac{1}{2\pi}\frac{1}{2\pi}\, d\theta_i\, d\theta_j\, d\phi_i\, d\phi_j}}_{\text{part C}}$$

$$= \underbrace{\frac{0}{\left(e^{-\lambda\pi}-1\right)^2}}_{\text{part A}} + \underbrace{\frac{0}{\left(e^{-\lambda\pi}-1\right)^2}}_{\text{part B}} - \underbrace{\frac{\mu^2\lambda^4\left(e^{-\lambda\pi}+1\right)^2}{2\pi\epsilon_0 r^3\left(\lambda^2+1\right)^2}\cdot\frac{1}{\left(e^{-\lambda\pi}-1\right)^2}}_{\text{part C}}$$

$$= -\frac{2\mu^2\lambda^4\left(e^{-\lambda\pi}+1\right)^2}{4\pi\epsilon_0 r^3\left(\lambda^2+1\right)^2\left(e^{-\lambda\pi}-1\right)^2}$$

[1] Based on our observation from MD simulation result.

Note that details of part A, B, and C calculations are described in Appendix E.

Unit of average dipole-dipole interaction energy

$$\text{unit of } \overline{U_{dd}} = \text{unit of } \frac{\mu^2}{\epsilon_0 r^3} = \frac{[Cm]^2}{[C^2N^{-1}m^{-2}][m]^3} = \frac{C^2m^2N}{C^2m} = Nm = J$$

3.4.2 Dipole-dipole interaction energy over an ellipsoid

We want to integrate $\overline{U_{dd}}$ over an ellipsoid.

$$\frac{1}{2}\iiint\limits_E \iiint\limits_E \overline{U_{dd}}\; dx_1\, dy_1\, dz_1\, dx_2\, dy_2\, dz_2 =$$

$$\text{constant} \times \underbrace{\frac{1}{2}\iiint\limits_E \iiint\limits_E \frac{1}{r^3}\; dx_1\, dy_1\, dz_1\, dx_2\, dy_2\, dz_2}_{\text{main part}}$$

where the integrating bound E representing an ellipsoid.

$$\frac{x^2}{a^2} + \frac{y^2}{b^2} + \frac{z^2}{c^2} \leq 1$$

We will look into the main part.

$$\iiint\limits_E \iiint\limits_E \frac{1}{r^3}\; dx_1\, dy_1\, dz_1\, dx_2\, dy_2\, dz_2$$

$$= \iiint\limits_E \iiint\limits_E \frac{1}{\sqrt{(x_1-x_2)^2 + (y_1-y_2)^2 + (z_1-z_2)^2}^3}\; dx_1\, dy_1\, dz_1\, dx_2\, dy_2\, dz_2$$

We change the variables as follows.

$$\begin{array}{lll}
x_1 = a\,\bar{x}_1 & \text{and} & dx_1 = a\,d\bar{x}_1 \\
y_1 = b\,\bar{y}_1 & \text{and} & dy_1 = b\,d\bar{y}_1 \\
z_1 = c\,\bar{z}_1 & \text{and} & dz_1 = c\,d\bar{z}_1 \\
x_2 = a\,\bar{x}_2 & \text{and} & dx_2 = a\,d\bar{x}_2 \\
y_2 = b\,\bar{y}_2 & \text{and} & dy_2 = b\,d\bar{y}_2 \\
z_2 = c\,\bar{z}_2 & \text{and} & dz_2 = c\,d\bar{z}_2
\end{array}$$

Then the integrating bound E becomes S representing sphere.

$$\bar{x}^2 + \bar{y}^2 + \bar{z}^2 \leq 1$$

Then the integration becomes

$$\iiint_E \iiint_E \frac{1}{\sqrt{(x_2-x_1)^2+(y_2-y_1)^2+(z_2-z_1)^2}^3}\, dx_1\, dy_1\, dz_1\, dx_2\, dy_2\, dz_2$$
$$= \iiint_S \iiint_S \frac{a^2b^2c^2}{\sqrt{(a\bar{x}_2-a\bar{x}_1)^2+(b\bar{y}_2-b\bar{y}_1)^2+(c\bar{z}_2-c\bar{z}_1)^2}^3}\, d\bar{x}_1\, d\bar{y}_1\, d\bar{z}_1\, d\bar{x}_2\, d\bar{y}_2\, d\bar{z}_2$$
$$= \iiint_S \iiint_S \frac{a^2b^2c^2}{\sqrt{a^2(\bar{x}_2-\bar{x}_1)^2+b^2(\bar{y}_2-\bar{y}_1)^2+c^2(\bar{z}_2-\bar{z}_1)^2}^3}\, d\bar{x}_1\, d\bar{y}_1\, d\bar{z}_1\, d\bar{x}_2\, d\bar{y}_2\, d\bar{z}_2$$

We change the cartesian coordinate systems to spherical coordinates

$$\bar{x} = \rho\sin(\theta)\cos(\phi)$$
$$\bar{y} = \rho\sin(\theta)\sin(\phi)$$
$$\bar{z} = \rho\cos(\theta)$$

Then we have

$$\iiint_S \iiint_S \frac{a^2b^2c^2}{\sqrt{a^2(\bar{x}_1-\bar{x}_2)^2+b^2(\bar{y}_1-\bar{y}_2)^2+c^2(\bar{z}_1-\bar{z}_2)^2}^3}\, d\bar{x}_1\, d\bar{y}_1\, d\bar{z}_1\, d\bar{x}_2\, d\bar{y}_2\, d\bar{z}_2$$
$$= \int_0^{2\pi}\int_0^{\pi}\int_0^{1} \int_0^{2\pi}\int_0^{\pi}\int_0^{1} \frac{a^2b^2c^2}{\sqrt{a^2(\rho_2\sin\theta_2\cos\phi_2-\rho_1\sin\theta_1\cos\phi_1)^2+b^2(\rho_2\sin\theta_2\sin\phi_2-\rho_1\sin\theta_1\sin\phi_1)^2}\cdots$$
$$\cdots\frac{}{\sqrt{c^2(\rho_2\cos\theta_2-\rho_1\cos\theta_1)^2}^3}\, \rho_1^2\sin\theta_1\rho_2^2\sin\theta_2\; d\rho_1\, d\theta_1\, d\phi_1\, d\rho_2\, d\theta_2\, d\phi_2$$

We computed the integral to calculate $\overline{U_{dd}}$ over an ellipsoid for $r_0 = 2$ nm case and plotted it against the aspect ratio $\lambda = c/a$ as shown in Figure 3.14.

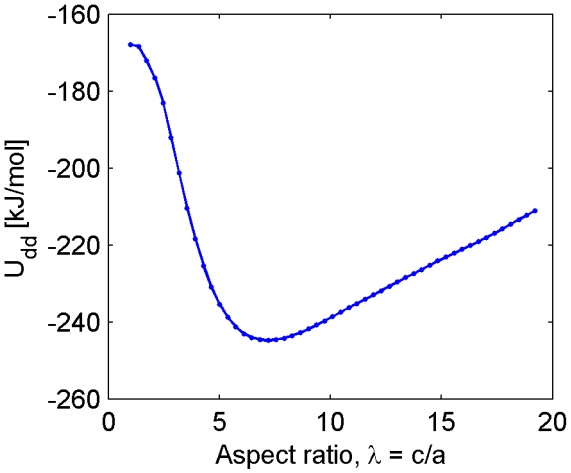

Figure 3.14: Plot of the dipole-dipole energy, U_{dd} versus the aspect ratio, $\lambda = c/a$ of prolate with $r_0 = 2$ nm.

We can observe that average dipole-dipole interaction energy, U_{dd} decreases only until some level of aspect ratio. This result support the explanation of the reason why droplets stretches until some point but does not extend until anymore.

3.5 Conclusions

We have presented a detailed study of the structural and energetic behavior of nanodroplets under the influence of an externally applied electric field. A careful analysis of a multitude of simulations revealed the molecular mechanism of the nanodroplet shape extension in the electric field. We found that the transformation of an initially spherical droplet into a highly extended prolate ellipsoid is due to the tendency of water dipoles to align with the electric field and reorganize to minimize the dipole-dipole interaction energy. A quantitative theory was developed to predict the shape and temporal dynamics of the nanodroplet given its initial radius and the strength of the applied electric field. The analysis allowed to describe the energetic landscape of the nanodroplet transitions between equilibrium states. In fact, it was revealed that for a mid-range of critical electric field strengths it is possible to have two local equilibrium states and Arrhenius-like behavior of the nanodroplet as it has to overcome the energy barrier to reach the global minima. The theoretical predictions agree well with previously obtained results for macrodroplets. A combination of empirical and theoretical arguments yielded formulas that connect important parameters of the system and predict the nanodroplet behavior as the function of its initial size and the strength of the external electric field. The results of the study provide additional evidence for the theory of water dipoles driven formation of the pores in biological membranes as well as relevance to a variety of scientific and engineering applications.

Chapter 4

Conclusion

We studied behavior of water molecules under the influence of an externally imposed electric field using two different model systems.

We simulated a process of electroporation of a phospholipid bilayer to understand the initiation mechanism of pore formation in biological membrane. We not only simulated a piece of lipid bilayer surrounded by water (WLW) system that has been studied in the past but also created and simulated a simple water only (WVW) system. Through a direct structural and energetic analysis of large number of simulation trajectories, we showed that pore is initiated by water molecules. The interfacial water molecules protrude from the surface and form a column-like structure as their dipole moments align with an external electric field. We observed that the per-molecule potential energy of the water protrusion interacting with other water molecules decreases as the height of protrusion grows. We also observed that the per-molecule potential energy of the water protrusion interacting with phospholipids increases. We conclude that the membrane phospholipids act as a sticky barrier to the interfacial water molecules advancing into the interior of the membrane in response to the external electric field applied. Furthermore, we modeled two simple configurations consisting of seven dipoles. By comparing the energy of these dipoles, we demonstrated the energetic benefits of the interfacial water protrusion as well as the existence of a critical electric field that causes electroporation.

Our WLW and WVW models have certain limitations. In particular, due to the periodic boundary conditions employed in both model systems, long-range electrostatic forces has to be approximated using Particle Mesh Ewald method and cut-off has to used to compute van der Waal's interactions. In order to overcome the limitation caused by periodic boundary conditions, we created a nano-sized water droplet and studied water behavior in the external electric field. The advantage of nanodroplet model is that we can compute interaction forces without use of above any cut-offs or approximations. We simulated a large number of droplets in many different sizes and using different water models while varying electric field. We illustrated the structural changes of nano-sized water droplets. We observed that the droplets under certain electric field stays in a slightly prolate spherical form but if an external electric field strength is above certain level then the droplets dramatically stretch in the field direction. Through analysis of MD trajectories, we showed that the potential energy of the droplet decreases as the droplet stretches its shape. We investigated the dependance of critical electric field that causes the stretching on the initial radius of the droplet. For smaller droplet, higher field is required to extend. We compared the

critical fields for different sizes of the droplet found from MD simulations with a theoretical Taylor's model and a semi-empirical model of our own and showed that they follow the similar pattern. A key achievement of semi-empirical model we proposed is that this model is built simply by balancing the internal energy of the droplet instead of complicated free energy analysis. Further, from the energy analysis result, we demonstrated that two local equilibrium states, slightly prolated shape and fully extended shape, are possible. Also, we observed that the nanodroplets in an electric field follows Arrhenius-like behavior as it has to overcome the energy barrier to reach the global minima. Finally, we developed a simple continuum model of dipoles only and explained the reason why the droplets only extend up to a certain length.

Future direction

In the future, we want to develop a predictive analytical theory that describes the shape and dynamics of the droplet with respect to the key parameters such as the strength of the electric field and the initial volume of the droplet. Taylor's model assumes that the electric conductivity is constant inside the droplet. Also, the energy balancing model assumes homogeneous distribution of an angle between the water dipoles and the electric field inside the droplet. However, for large droplets we are questioning this assumption and, in fact, we have some preliminary results that indicate the existence of both the "bulk" and the "interface" regions inside a large droplet. The main difference between these two regions is the ability of water dipoles to align with the electric field with the "interface" dipoles being able to attain a much smaller angle with the external field compared to "bulk" waters.

Our preliminary MD simulations of larger nano-sized droplets, $r_0 = 5$ nm and $r_0 = 6$ nm, indicate that electric permittivity properties inside the droplet may not be assumed as a constant. We divide the droplet into six regions as shown in Figure 4.1. Then the average dipole angle in each regions is computed for every time step in the MD trajectory.

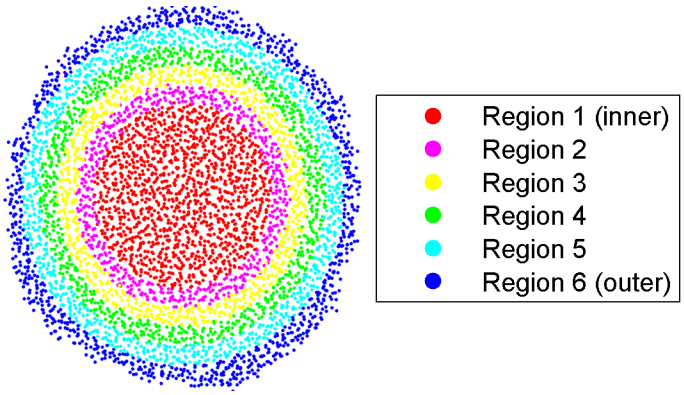

Figure 4.1: Cross section of $r_0 = 5$ droplet. Six regions are shown in different colors. The regions are defined by the radial distance from the center of mass of the droplet. The inner most region has the molecules located less than 50% of the principal radii. Then for the following regions, the length definition is increased by 10%. The outer most region has the molecules located further than 90% of the principal radii.

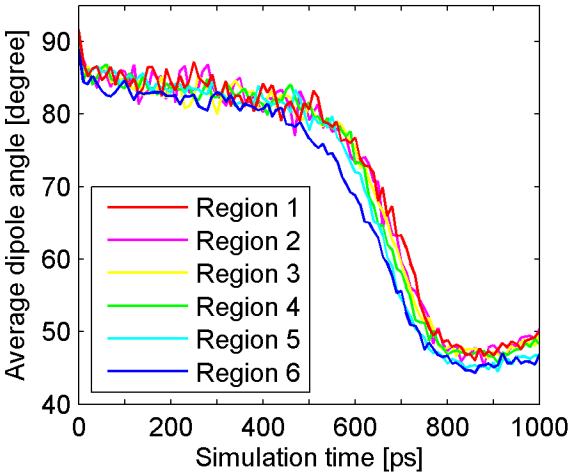

Figure 4.2: Plot of average dipole angle in six regions versus simulation time of droplet with $r_0 = 5$ nm with $E = 600$ MV/m

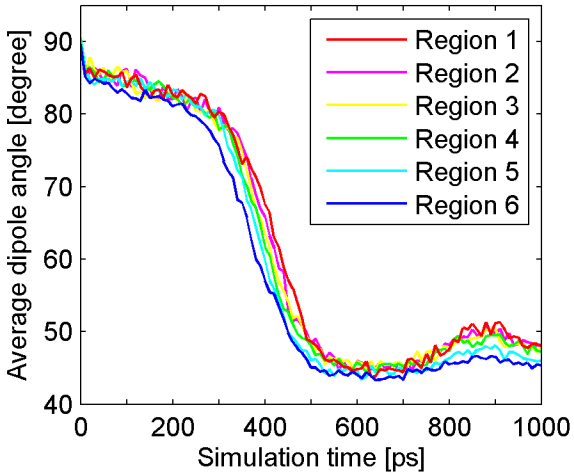

Figure 4.3: Plot of average dipole angle in six regions versus simulation time of droplet with $r_0 = 6$ nm with $E = 600$ MV/m

Figure 4.2 and Figure 4.3 show how the average dipole angle is changing over time for six different regions inside $r_0 = 5$ nm and $r_0 = 6$ nm droplets respectively under 600 MV/m external electric field. We observe that the dipoles in the inner most (red line) part of both droplets are less aligned to the field, i.e. bigger angle, than the dipoles in the outer most (blue line) surface. We will investigate whether just like in our simulations of electroporation, a large droplet roughly splits into an interfacial and bulk water regions which have different electric permittivity properties i.e., the water dipoles are more or less aligned with the field. If the difference is observed then we can parameterize this factor as a variable and integrate into the analytical model that predict the shape and dynamics of the droplet.

Appendix A

Analysis methods

A.1 Energetic analysis

For energetic analysis, we calculate the total potential energy comprised of three terms:

- the electrostatic (Coulomb) interaction energy (Equation A.1),
- the van der Waals interaction energy using Lennard-Jones approximation (Equation A.2),
- the interaction energy between the water dipoles and the applied external electric field (Equation A.3).

In addition, we calculate the dipole-dipole interaction energy (Equation A.4).

The equations for the electrostatic, Lennard-Jones, and dipole-dipole interactions describe the interaction between a pair. In Chapter 2, we compute these interaction energy by summing over all pairwise interactions between the atoms of the regions of interest. For example, the interaction energy between the protrusion waters and bulk waters, we add all the pairwise interactions among the protrusion waters and all the pairwise interactions between the regions. In Chapter 3, these interaction energy is a total sum over all pairwise interactions between the atoms of the droplet.

The dipole-dipole interaction energy and the dipole-field interaction energy are only relevant to water molecules.

For a droplet study, we calculate the surface energy (Equation A.5).

Electrostatic interaction energy

The electrostatic interaction energy results from the Coulomb's law which describes the electrostatic interaction between electrically charged particles. The electrostatic interaction energy between two atoms, i and j, with two charges q_i and q_j that are separated by a vector $\mathbf{r}_{ij}$ is given by

$$U_{el}(\mathbf{r}_{ij}) = \left(\frac{1}{4\pi\epsilon_0}\frac{q_i q_j}{\|\mathbf{r}_{ij}\|}\right) \tag{A.1}$$

where ϵ_0 is the vacuum permittivity and $\|\mathbf{r}_{ij}\|$ is the distance between two atoms, i and j.

Lennard-Jones interaction energy

The van der Waal's interaction is the sum of the attractive or repulsive forces between molecules. The Lennard-Jones potential is used to approximate the interaction between two atoms i and j separated by a vector $\mathbf{r}_{ij}$ is given by

$$U_{lj}(\mathbf{r}_{ij}) = 4\epsilon_{ij}\left[\left(\frac{\sigma_{ij}}{\|\mathbf{r}_{ij}\|}\right)^{12} - \left(\frac{\sigma_{ij}}{\|\mathbf{r}_{ij}\|}\right)^{6}\right] \tag{A.2}$$

where ϵ (depth of the potential well) and σ (finite distance at which the inter-particle potential is zero) are constants depending on the types of the atoms in a pair. The first term (r^{-12}) describes a repulsion at short ranges and the second term (r^{-6}) describes an attraction at long ranges.

For a simple water model in MD simulation like `SPC/E`, only oxygen-oxygen pairs are considered for Lennard-Jones approximation. Hence, the equation above simplifies to

$$\frac{C_{12}}{\|\mathbf{r}_{oo}\|^{12}} - \frac{C_6}{\|\mathbf{r}_{oo}\|^{6}}.$$

where $\|\mathbf{r}_{oo}\|$ is the distance between oxygens of two water molecules and the constants are $C_{12} = 4\epsilon_{oo}\sigma_{oo}^{12}$ and $C_6 = 4\epsilon_{oo}\sigma_{oo}^{6}$.

Dipole-field interaction energy

If an external electric field is applied to dipolar molecules, energy induced by dipole re-orientation. The interaction energy between water dipoles and the applied external electric field is given by

$$U_{df} = -\boldsymbol{\mu}\cdot\mathbf{E} = -\|\boldsymbol{\mu}\|\|\mathbf{E}\|\cos(\theta) \tag{A.3}$$

where $\boldsymbol{\mu}$ is a dipole moments of water molecule, $\mathbf{E}$ is the electric field in vector form, and θ is an angle between the dipole moment and the electric field direction. Measuring method of θ is described in the next section.

Dipole-dipole interaction energy

The dipole-dipole interaction is the electrostatic interaction between dipoles of dipolar molecules. The dipole-dipole interaction energy between two dipolar molecules, i and j, with the dipole moments of $\boldsymbol{\mu}_i$ and $\boldsymbol{\mu}_j$ that are separated by a vector $\mathbf{r}_{ij}$ is given by

$$U_{\boldsymbol{\mu}_i\boldsymbol{\mu}_j} = \frac{1}{4\pi\epsilon_0}\frac{\|\mathbf{r}_{ij}\|^2\boldsymbol{\mu}_i\cdot\boldsymbol{\mu}_j - 3(\boldsymbol{\mu}_i\cdot\mathbf{r}_{ij})(\boldsymbol{\mu}_j\cdot\mathbf{r}_{ij})}{\|\mathbf{r}_{ij}\|^5} \tag{A.4}$$

where ϵ_0 is the vacuum permittivity and $\|\mathbf{r}_{ij}\|$ is the distance between dipoles.

For a water molecule,

$$\boldsymbol{\mu} = \sum q_{\text{atom}}\mathbf{r}_{\text{atom}} = q_{\text{O}}\mathbf{r}_O + q_{\text{H}_1}\mathbf{r}_{\text{H}_1} + q_{\text{H}_2}\mathbf{r}_{\text{H}_2}.$$

Surface energy (for droplet only)

The surface energy [83, 84] can be computed by multiplying the surface tension γ and the surface area of droplet SA.

$$U_{surf} = \gamma \cdot SA \tag{A.5}$$

For a nano-sized water droplets we present in Chapter 3, we find the surface area of the droplet by assuming the shape fits an ellipsoid. More detailed explanation of ellipsoid fitting and finding the surface area of fitted ellipsoid is described in the next section. We use the surface tension value, 63.6 mJ/m^2 found by Vega and Miguel [80].

A.2 Structural analysis (for droplet only)

We conduct various structural analysis to investigate the structural changes occurring in water droplet simulations under the influence of external electric field.

Evaporating water

Unlike a WVW simulation with periodic boundary condition, water molecules can evaporate from a droplet surface in a droplet simulation since it is placed in a vacuum. Throughout the droplet simulations, we monitor the number of water molecules evaporated from the droplet. Water molecule(s) is(are) defined as "evaporated" if any monomer, dimer or trimer of water is more than 1 nm from any other water molecule in the droplet surface.

Dipole alignment

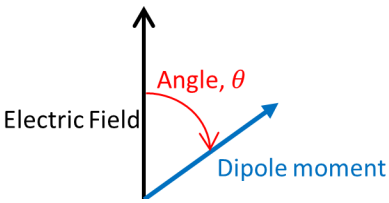

To understand the mechanism governing shape extension, we inspect behavior of water dipoles by calculating the angle, θ, between a water dipole moment and the external electric field direction, $+Z$. The angle is measurement from the field direction $+Z$ to the water dipole moment as shown in the picture. We keep track of all angles of water dipole moment in the system as well as the average angle.

Shape related parameters

To study the relationship between the shape of the droplet and the electric field strength, we quantified the droplet shape by a scalar number called the shape parameter. This shape measuring technique is commonly used to analyze conformations of polymers [78] or proteins [79]. Characteristics of the conformation such as asphericity, acylindricity, and anisotropy can be measured using the gyration tensor [77] which describes the second moments [85] i.e. rotational inertia, of the position of a collection of particles.

The gyration tensor, T, in a Cartesian coordinate system is expressed as

$$T = \frac{1}{N}\sum_{i=1}^{N}\begin{bmatrix} r_x^i r_x^i & r_x^i r_y^i & r_x^i r_z^i \\ r_y^i r_x^i & r_y^i r_y^i & r_y^i r_z^i \\ r_z^i r_x^i & r_z^i r_y^i & r_z^i r_z^i \end{bmatrix}$$

where a position vector r_i is the displacement of the i^{th} particle from the center of mass of a droplet.

In the computation, only the coordinates of the oxygen atoms x, y, and z are used to produce the gyration tensor matrix. Since the mass, m of N oxygen atoms are the same, coordinates of the center of mass of the droplet are simplified as

$$\mathbf{r}_{CM}(x,y,z) = \frac{\sum_{i=1}^{N} \mathbf{r}_i m_i}{\sum_{i=1}^{N} m_i} = \frac{1}{N}\sum_{i=1}^{N} \mathbf{r}_i$$

Hence, for the droplet in a three-dimensional Cartesian coordinate system, the gyration tensor becomes

$$T = \frac{1}{N}\sum_{i=1}^{N} \begin{bmatrix} \overline{(x^i - x^i_{CM})^2} & \overline{(x^i - x^i_{CM})(y^i - y^i_{CM})} & \overline{(x^i - x^i_{CM})(z^i - z^i_{CM})} \\ \overline{(y^i - y^i_{CM})(x^i - x^i_{CM})} & \overline{(y^i - y^i_{CM})^2} & \overline{(y^i - y^i_{CM})(z^i - z^i_{CM})} \\ \overline{(z^i - z^i_{CM})(x^i - x^i_{CM})} & \overline{(z^i - z^i_{CM})(y^i - y^i_{CM})} & \overline{(z^i - z^i_{CM})^2} \end{bmatrix}$$

The eigenvalues of the gyration tensor, T, called the principal moments, are used to compute asphericity A [79] and the shape parameter S [79] of the droplet are defined as

$$A = \frac{\sum_{i=1}^{3} \left(\lambda_i - \overline{\lambda} \right)^2}{\left(\overline{\lambda} \right)^2} \qquad \text{and} \qquad S = \frac{\prod_{i=1}^{3} \left(\lambda_i - \overline{\lambda} \right)}{\left(\overline{\lambda} \right)^3}$$

where λ_i is the i^{th} eigenvalue of T representing the squares of the three principal radii of gyration and $\overline{\lambda}$ is the mean eigenvalue defined as $\frac{\text{tr}(T)}{3}$.

The asphericity parameter A is always non-negative and zero when particles are distributed in a spherically symmetric way (i.e. sphere). The shape parameter S is always bounded between -1/4 and 2 and the range of S values corresponds to the shapes of the ellipsoid. The shape is defined to be an oblate ellipsoid for $-1/4 < S < 0$, a sphere for $S = 0$, and a prolate ellipsoid for $0 < S < 2$.

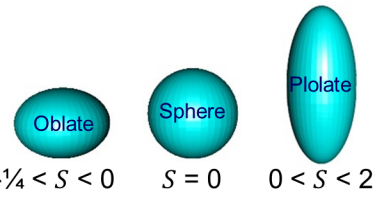

Ellipsoid fitting

We assume that the shape of a droplet fits an ellipsoid and computed its three principal axes and its length using the inertia tensor [86]. The inertia tensor I is the scaling factor between angular momentum L and angular velocity ω (i.e. $L = I \cdot \omega$), which is expressed in a Cartesian coordinate system as

$$I = \frac{1}{N}\sum_{i=1}^{N} \begin{bmatrix} m^i \left[(r^i_y)^2 + (r^i_z)^2 \right] & -m_i r^i_x r^i_y & -m_i r^i_x r^i_z \\ -m_i r^i_y r^i_x & m^i \left[(r^i_x)^2 + (r^i_z)^2 \right] & -m_i r^i_y r^i_z \\ -m_i r^i_z r^i_x & -m_i r^i_z r^i_y & m^i \left[(r^i_x)^2 + (r^i_y)^2 \right] \end{bmatrix}$$

where m is mass of oxygen and a position vector r^i is again the displacement of the i^{th} particle from the center of mass of a droplet. The eigenvectors of the inertia tensor represent directions of the three principal axes and the corresponding eigenvalues are called the principal moments of inertia about the given axes.

We computed the lengths of the three principal axes of the ellipsoid by equating the eigenvalues of the computed inertia tensor above with the moment of inertia tensor [87] for solid ellipsoid of axes a, b, and c with mass m given below.

$$I = \frac{1}{N}\sum_{i=1}^{N}\begin{bmatrix} \frac{1}{5}m(b^2+c^2) & 0 & 0 \\ 0 & \frac{1}{5}m(a^2+c^2) & 0 \\ 0 & 0 & \frac{1}{5}m(a^2+b^2) \end{bmatrix}$$

Surface area of the fitted ellipsoid

Using the axes information obtained from ellipsoid fitting process, we calculate approximate surface area of the fitted ellipsoid. The surface area, SA of a general ellipsoid [88] is given by

$$SA = 2\pi c^2 + \frac{2\pi ab}{\sin\phi}\left[E(\phi,k)\sin^2\phi + F(\phi,k)\cos^2\phi\right]$$

where three axes a, b, and c are in order of $a \geq b \geq c$ and

$$\cos\phi = \frac{c}{a} \qquad \text{and} \qquad k^2 = \frac{a^2(b^2-c^2)}{b^2(a^2-c^2)}.$$

Two functions $F(\phi,k)$ and $E(\phi,k)$ are incomplete elliptic integrals of the first and the second kind [89], respectively. We used `C` code provided in Mathematics Source Library [90] for calculation of these elliptic integrals.

Appendix B

List of all WLW and WVW simulations performed and the associated parameters

All the MD simulations performed for the electroporation project is presented.

- Table B.1 has a list of all the simulations used to determine pore initiation time for WLW and WVW systems.
- Table B.2 has a list of all the simulations used to analyze energetics of both WLW and WVW systems.
- Table B.3 and B.4 lists all simulations used to study the effects of vacuum gap size in WVW systems.
- Table B.5 has a list of all WVW simulations used to study the effects of short-range electrostatic cutoffs
- Table B.6 has a list of all WVW simulations used to study the effects of different water models.

Table B.1: WLW and WVW simulations used to determine pore initiation time

Simulation Type	System Size	Force Fields	Water model	Electric field [MV/m]	# of trials	Ensemble	Temp [K]	T coupling	Compressibility	Bond lengths constraints algorithm	Short-range electrostatic cutoff [nm]	Long-range Lennard-Jones cutoff [nm]	Long-range electrostatic model	FFT, Fouier spacing	Interpolation order	Pressure bath
WLW	128 POPC, 4480 Waters	OPLS	SPC/E	400	3	NPT	310	v-rescale	0.000045	LINCS	1.4	1.4	PME	0.12	4	1 bar
WLW	128 POPC, 4480 Waters	OPLS	SPC/E	450	3	NPT	310	v-rescale	0.000045	LINCS	1.4	1.4	PME	0.12	4	1 bar
WLW	128 POPC, 4480 Waters	OPLS	SPC/E	500	3	NPT	310	v-rescale	0.000045	LINCS	1.4	1.4	PME	0.12	4	1 bar
WLW	128 POPC, 4480 Waters	OPLS	SPC/E	550	3	NPT	310	v-rescale	0.000045	LINCS	1.4	1.4	PME	0.12	4	1 bar
WLW	128 POPC, 4480 Waters	OPLS	SPC/E	600	3	NPT	310	v-rescale	0.000045	LINCS	1.4	1.4	PME	0.12	4	1 bar
WLW	128 POPC, 4480 Waters	OPLS	SPC/E	650	3	NPT	310	v-rescale	0.000045	LINCS	1.4	1.4	PME	0.12	4	1 bar
WLW	128 POPC, 4480 Waters	OPLS	SPC/E	700	3	NPT	310	v-rescale	0.000045	LINCS	1.4	1.4	PME	0.12	4	1 bar

Simulation type	Computational domain dimensions	Vaccum gap size	Water model	Electric field [MV/m]	# of trials	Ensemble	Temp [K]	T coupling	Compressibility	Bond lengths constraints algorithm	Short-range electrostatic cutoff [nm]	Long-range Lennard-Jones cutoff [nm]	Long-range electrostatic model	FFT, Fouier spacing	Interpolation order	Pressure bath
WVW	7 nm by 7 nm by 7 nm, 6877 Waters	2.8 nm	SPC/E	500	3	NVT	310	v-rescale	n/a	LINCS	1.4	1	PME	0.12	4	n/a
WVW	7 nm by 7 nm by 7 nm, 6877 Waters	2.8 nm	SPC/E	600	3	NVT	310	v-rescale	n/a	LINCS	1.4	1	PME	0.12	4	n/a
WVW	7 nm by 7 nm by 7 nm, 6877 Waters	2.8 nm	SPC/E	700	3	NVT	310	v-rescale	n/a	LINCS	1.4	1	PME	0.12	4	n/a
WVW	7 nm by 7 nm by 7 nm, 6877 Waters	2.8 nm	SPC/E	800	3	NVT	310	v-rescale	n/a	LINCS	1.4	1	PME	0.12	4	n/a

Table B.2: WLW and WVW simulations used to analyze energetics of the systems

Simulation Type	System Size	Force Fields	Water model	Electric field [MV/m]	# of trials	Ensemble	Temp [K]	T coupling	Compressibility	Bond lengths constraints algorithm	Short-range electrostatic cutoff [nm]	Long-range Lennard-Jones cutoff [nm]	Long-range electrostatic model	FFT, Fouier spacing	Interpolation order	Pressure bath
WLW	128 POPC, 4480 Waters	OPLS	SPC/E	500*	10	NPT	310	v-rescale	0.000045	LINCS	1.4	1.4	PME	0.12	4	1 bar
WLW	128 POPC, 4480 Waters	OPLS	SPC/E	600	30	NPT	310	v-rescale	0.000045	LINCS	1.4	1.4	PME	0.12	4	1 bar
WLW	128 POPC, 4480 Waters	OPLS	SPC/E	700	10	NPT	310	v-rescale	0.000045	LINCS	1.4	1.4	PME	0.12	4	1 bar

Simulation type	Computational domain dimensions	Vaccum gap size	Water model	Electric field [MV/m]	# of trials	Ensemble	Temp [K]	T coupling	Compressibility	Bond lengths constraints algorithm	Short-range electrostatic cutoff [nm]	Long-range Lennard-Jones cutoff [nm]	Long-range electrostatic model	FFT, Fouier spacing	Interpolation order	Pressure bath
WVW	7 nm by 7 nm by 7 nm, 6877 Waters	2.8 nm	SPC/E	500*	10	NVT	310	v-rescale	n/a	LINCS	1.4	1.4	PME	0.12	4	n/a
WVW	7 nm by 7 nm by 7 nm, 6877 Waters	2.8 nm	SPC/E	600	30	NVT	310	v-rescale	n/a	LINCS	1.4	1.4	PME	0.12	4	n/a
WVW	7 nm by 7 nm by 7 nm, 6877 Waters	2.8 nm	SPC/E	700	10	NVT	310	v-rescale	n/a	LINCS	1.4	1.4	PME	0.12	4	n/a

Table B.3: WVW simulations used to study the effects of vacuum gap size

Simulation type	Computational domain dimensions	Vaccum gap size	Water model	Electric field [MV/m]	# of trials	Ensemble	Temp [K]	T coupling	Compressibility	Bond lengths constraints algorithm	Short-range electrostatic cutoff [nm]	Long-range Lennard-Jones cutoff [nm]	Long-range electrostatic model	FFT, Fouier spacing	Interpolation order	Pressure bath
WVW	7 nm by 7 nm by 7 nm, 7231 Waters	2.6 nm	SPC/E	300	3	NVT	310	v-rescale	n/a	LINCS	1	1	PME	0.12	4	n/a
WVW	7 nm by 7 nm by 7 nm, 7231 Waters	2.6 nm	SPC/E	400	3	NVT	310	v-rescale	n/a	LINCS	1	1	PME	0.12	4	n/a
WVW	7 nm by 7 nm by 7 nm, 7231 Waters	2.6 nm	SPC/E	500	3	NVT	310	v-rescale	n/a	LINCS	1	1	PME	0.12	4	n/a
WVW	7 nm by 7 nm by 7 nm, 7231 Waters	2.6 nm	SPC/E	600	3	NVT	310	v-rescale	n/a	LINCS	1	1	PME	0.12	4	n/a
WVW	7 nm by 7 nm by 7 nm, 7231 Waters	2.6 nm	SPC/E	700	3	NVT	310	v-rescale	n/a	LINCS	1	1	PME	0.12	4	n/a
WVW	7 nm by 7 nm by 7 nm, 7231 Waters	2.6 nm	SPC/E	800	3	NVT	310	v-rescale	n/a	LINCS	1	1	PME	0.12	4	n/a
WVW	7 nm by 7 nm by 7 nm, 6877 Waters	2.8 nm	SPC/E	300	3	NVT	310	v-rescale	n/a	LINCS	1	1	PME	0.12	4	n/a
WVW	7 nm by 7 nm by 7 nm, 6877 Waters	2.8 nm	SPC/E	400	3	NVT	310	v-rescale	n/a	LINCS	1	1	PME	0.12	4	n/a
WVW	7 nm by 7 nm by 7 nm, 6877 Waters	2.8 nm	SPC/E	450	3	NVT	310	v-rescale	n/a	LINCS	1	1	PME	0.12	4	n/a
WVW	7 nm by 7 nm by 7 nm, 6877 Waters	2.8 nm	SPC/E	500	3	NVT	310	v-rescale	n/a	LINCS	1	1	PME	0.12	4	n/a
WVW	7 nm by 7 nm by 7 nm, 6877 Waters	2.8 nm	SPC/E	600	3	NVT	310	v-rescale	n/a	LINCS	1	1	PME	0.12	4	n/a
WVW	7 nm by 7 nm by 7 nm, 6877 Waters	2.8 nm	SPC/E	700	3	NVT	310	v-rescale	n/a	LINCS	1	1	PME	0.12	4	n/a
WVW	7 nm by 7 nm by 7 nm, 6877 Waters	2.8 nm	SPC/E	800	3	NVT	310	v-rescale	n/a	LINCS	1	1	PME	0.12	4	n/a

Table B.4: WVW simulations used to study the effects of vacuum gap size

Simulation type	Computational domain dimensions	Vaccum gap size	Water model	Electric field [MV/m]	# of trials	Ensemble	Temp [K]	T coupling	Compressibility	Bond lengths constraints algorithm	Short-range electrostatic cutoff [nm]	Long-range Lennard-Jones cutoff [nm]	Long-range electrostatic model	FFT, Fouier spacing	Interpolation order	Pressure bath
WVW	7 nm by 7 nm by 7 nm, 6554 Waters	3 nm	SPC/E	600	3	NVT	310	v-rescale	n/a	LINCS	1	1	PME	0.12	4	n/a
WVW	7 nm by 7 nm by 7 nm, 6554 Waters	3 nm	SPC/E	700	3	NVT	310	v-rescale	n/a	LINCS	1	1	PME	0.12	4	n/a
WVW	7 nm by 7 nm by 7 nm, 6554 Waters	3 nm	SPC/E	800	3	NVT	310	v-rescale	n/a	LINCS	1	1	PME	0.12	4	n/a
WVW	7 nm by 7 nm by 7 nm, 6554 Waters	3 nm	SPC/E	900	3	NVT	310	v-rescale	n/a	LINCS	1	1	PME	0.12	4	n/a
WVW	7 nm by 7 nm by 7 nm, 5727 Waters	3.5 nm	SPC/E	650	3	NVT	310	v-rescale	n/a	LINCS	1	1	PME	0.12	4	n/a
WVW	7 nm by 7 nm by 7 nm, 5727 Waters	3.5 nm	SPC/E	700	3	NVT	310	v-rescale	n/a	LINCS	1	1	PME	0.12	4	n/a
WVW	7 nm by 7 nm by 7 nm, 5727 Waters	3.5 nm	SPC/E	800	3	NVT	310	v-rescale	n/a	LINCS	1	1	PME	0.12	4	n/a
WVW	7 nm by 7 nm by 7 nm, 5727 Waters	3.5 nm	SPC/E	900	3	NVT	310	v-rescale	n/a	LINCS	1	1	PME	0.12	4	n/a
WVW	7 nm by 7 nm by 7 nm, 4899 Waters	4 nm	SPC/E	800	3	NVT	310	v-rescale	n/a	LINCS	1	1	PME	0.12	4	n/a
WVW	7 nm by 7 nm by 7 nm, 4899 Waters	4 nm	SPC/E	850	3	NVT	310	v-rescale	n/a	LINCS	1	1	PME	0.12	4	n/a
WVW	7 nm by 7 nm by 7 nm, 4899 Waters	4 nm	SPC/E	900	3	NVT	310	v-rescale	n/a	LINCS	1	1	PME	0.12	4	n/a
WVW	7 nm by 7 nm by 7 nm, 4899 Waters	4 nm	SPC/E	1000	3	NVT	310	v-rescale	n/a	LINCS	1	1	PME	0.12	4	n/a

Table B.5: WVW simulations used to study the effects of short-range electrostatic cutoffs

Simulation type	Computational domain dimensions	Vaccum gap size	Water model	Electric field [MV/m]	# of trials	Ensemble	Temp [K]	T coupling	Compressibility	Bond lengths constraints algorithm	Short-range electrostatic cutoff [nm]	Long-range Lennard-Jones cutoff [nm]	Long-range electrostatic model	FFT, Fouier spacing	Interpolation order	Pressure bath
WVW	7 nm by 7 nm by 7 nm, 6877 Waters	2.8 nm	SPC/E	600	3	NVT	310	v-rescale	n/a	LINCS	1	1	PME	0.12	4	n/a
WVW	7 nm by 7 nm by 7 nm, 6877 Waters	2.8 nm	SPC/E	600	3	NVT	310	v-rescale	n/a	LINCS	1.2	1.2	PME	0.12	4	n/a
WVW	7 nm by 7 nm by 7 nm, 6877 Waters	2.8 nm	SPC/E	600	3	NVT	310	v-rescale	n/a	LINCS	1.4	1.4	PME	0.12	4	n/a
WVW	7 nm by 7 nm by 7 nm, 6877 Waters	2.8 nm	SPC/E	600	3	NVT	310	v-rescale	n/a	LINCS	1.6	1.6	PME	0.12	4	n/a
WVW	7 nm by 7 nm by 7 nm, 6877 Waters	2.8 nm	SPC/E	600	3	NVT	310	v-rescale	n/a	LINCS	1.8	1.8	PME	0.12	4	n/a

Table B.6: WVW simulations used to study the effects of different water models

Simulation type	Computational domain dimensions	Vaccum gap size	Water model	Electric field [MV/m]	# of trials	Ensemble	Temp [K]	T coupling	Compressibility	Bond lengths constraints algorithm	Short-range electrostatic cutoff [nm]	Long-range Lennard-Jones cutoff [nm]	Long-range electrostatic model	FFT, Fouier spacing	Interpolation order	Pressure bath
WVW	10 nm by 10 nm by 7 nm, 19870 Waters	4 nm	SPC/E	0	10	NVT	300	v-rescale	n/a	LINCS	1.2	1.2	PME	0.12	4	n/a
WVW	10 nm by 10 nm by 7 nm, 19870 Waters	4 nm	SPC/E	600	10	NVT	300	v-rescale	n/a	LINCS	1.2	1.2	PME	0.12	4	n/a
WVW	10 nm by 10 nm by 7 nm, 19870 Waters	4 nm	SPC/E	700	10	NVT	300	v-rescale	n/a	LINCS	1.2	1.2	PME	0.12	4	n/a
WVW	10 nm by 10 nm by 7 nm, 19870 Waters	4 nm	SPC/E	800	10	NVT	300	v-rescale	n/a	LINCS	1.2	1.2	PME	0.12	4	n/a
WVW	10 nm by 10 nm by 7 nm, 19870 Waters	4 nm	SPC/E	900	10	NVT	300	v-rescale	n/a	LINCS	1.2	1.2	PME	0.12	4	n/a
WVW	10 nm by 10 nm by 7 nm, 19870 Waters	4 nm	SPC/E	1000	10	NVT	300	v-rescale	n/a	LINCS	1.2	1.2	PME	0.12	4	n/a
WVW	10 nm by 10 nm by 7 nm, 19870 Waters	4 nm	SPC/E flexible	0	10	NVT	300	v-rescale	n/a	LINCS	1.2	1.2	PME	0.12	4	n/a
WVW	10 nm by 10 nm by 7 nm, 19870 Waters	4 nm	SPC/E flexible	600	10	NVT	300	v-rescale	n/a	LINCS	1.2	1.2	PME	0.12	4	n/a
WVW	10 nm by 10 nm by 7 nm, 19870 Waters	4 nm	SPC/E flexible	700	10	NVT	300	v-rescale	n/a	LINCS	1.2	1.2	PME	0.12	4	n/a
WVW	10 nm by 10 nm by 7 nm, 19870 Waters	4 nm	SPC/E flexible	800	10	NVT	300	v-rescale	n/a	LINCS	1.2	1.2	PME	0.12	4	n/a
WVW	10 nm by 10 nm by 7 nm, 19870 Waters	4 nm	SPC/E flexible	900	10	NVT	300	v-rescale	n/a	LINCS	1.2	1.2	PME	0.12	4	n/a
WVW	10 nm by 10 nm by 7 nm, 19870 Waters	4 nm	SPC/E flexible	1000	10	NVT	300	v-rescale	n/a	LINCS	1.2	1.2	PME	0.12	4	n/a

Appendix C

Choosing initial water-vacuum-water (WVW) configuration

A stable initial configuration has to be chosen to perform reliable simulations of WVW systems. In the absence of the external electric field we expect the water molecules to be arranged so that the surface area of the water-vacuum interface is minimized. Such configuration will then be stable and can be used as the initial condition for WVW simulations. To find such configuration let us consider a cubic box with side lengths L, containing a fixed volume of water V shown in Figure C.1(a).

Figure C.1: Three possible minimum surface area configurations for a cubic box containing fixed volume of water: (a) "sandwich" (the vacuum slab), (b) tube, and (c) spherical bubble

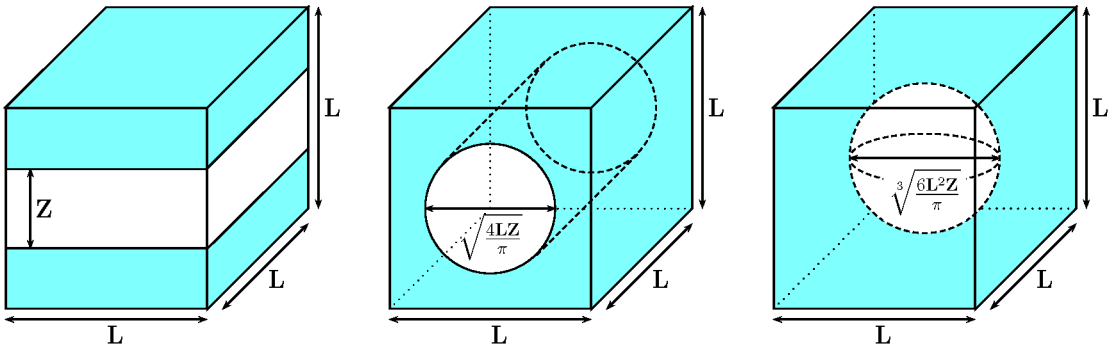

(a) $A = 2L^2$ (b) $A = 2\sqrt{\pi L^3 Z}$ (c) $A = 4\pi \left(\frac{3L^2 Z}{4\pi}\right)^{\frac{2}{3}}$

It is easy to see that there are three possible candidate configurations that can have a minimum surface area of the water-vacuum interface: (a) a rectangular vacuum layer of width Z, extending to the boundary and separating two rectangular water layers, i.e. a "sandwich" (Figure C.1(a)), (b) a cylindrical vacuum tube extending to the boundary

and surrounded by water (Figure C.1(b)), and (c) a spherical vacuum bubble surrounded by water (Figure C.1(c)). Since the volume is fixed for all three configurations, we can replace the parameter V with a parameter Z that corresponds to the vacuum layer width for the "sandwich" configuration. We can then calculate the surface area A for all three configurations in terms of the parameters Z and L as indicated in the Figure C.1). Thus for a given value of L we can compute the surface area A for a range of Z values and determine for each value of the Z a configuration with the smallest surface area. Simple algebraic manipulations of the formulas for the areas of the three configurations lead to the condition that the "sandwich" configuration will have the lowest surface area if Z obeys the relationship $Z > \frac{L}{\pi}$. Figure C.2 shows corresponding graphs for $L = 7$ nm; as we can see, for $Z = 2.8$ nm the "sandwich" i.e. the vacuum slab, configuration has the lowest surface area.

Now we need to choose the appropriate value for Z which satisfies $Z > \frac{L}{\pi}$. To ensure fair comparison with the water-lipid-water systems we need to choose the size of the gap so that the magnitude of the electric field experienced by the water molecules at the interface is comparable between the WVW and the WLW systems. It is not appropriate to compare the externally applied electric fields for the two systems since the presence of lipids will influence the magnitude of the electric field at the interface. On the other hand the size of the vacuum gap will have an effect on the resulting electric field at the water-vacuum interface for the WVW configuration. For the WLW system the membrane size is set by the mean separation of the POPC glycerol acyl oxygen atoms from one lipid leaflet to the other. Thus to choose the gap size for the WVW system we first apply different values of the external electric field to the WLW system and measure the resulting internal electric field at the water-lipids interface. We then vary the vacuum gap size Z in the WVW configuration for the same range of the external electric field magnitudes to obtain the same values of the internal electric field at the water-vacuum interface as in the water-lipid interface case. Such approach led us to choose the value of Z to be 2.8 nm. For this value of Z both the external and the internal interface electric fields magnitudes agree between the WLW and the WVW systems, thus the comparison of poration times Figure 2.4 is fair.

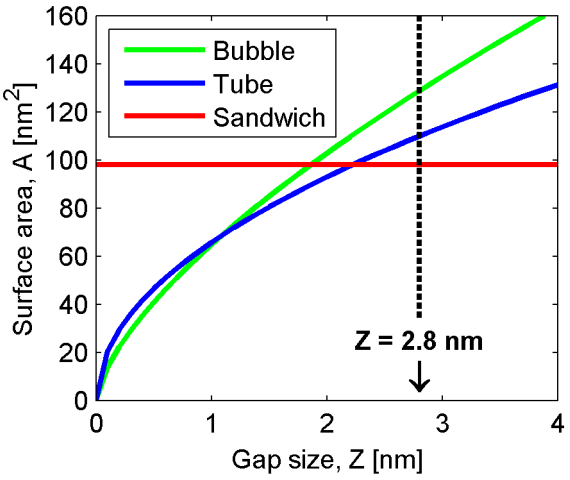

Figure C.2: Surface area of the three potential minimum area configurations for a fixed value of $L = 7$ nm and a varying value of Z. For $Z = 2.8$ nm the "sandwich" configuration has the lowest surface area.

Appendix D

Nanodroplet analysis data

D.1 Structural analysis result of nanodroplet stretching simulations

In Table D.1, we present structural analysis data from the stretching simulations.

r_0 [nm]	water model used	electric field, E [MV/m]	time to extension	shape parameter, S	$\lambda = \frac{c}{a}$	ellipsoid surface area [Å²]	water evaporation rate [waters/ns]	angle between dipole and electric field [degrees]
2	SPC/E	0	no extension observed (NE)	0.00 ± 0.00	1.00 ± 0.02	5041.20 ± 12.99	0.39 ± 0.16	90.01 ± 0.04
		100	NE	0.00 ± 0.00	1.01 ± 0.02	5039.53 ± 9.55	0.45 ± 0.18	89.30 ± 0.03
		200	NE	0.00 ± 0.00	1.02 ± 0.01	5039.58 ± 12.26	0.52 ± 0.32	88.60 ± 0.05
		300	NE	0.00 ± 0.00	1.04 ± 0.02	5048.37 ± 9.70	0.41 ± 0.16	87.86 ± 0.05
		400	NE	0.00 ± 0.00	1.07 ± 0.02	5056.07 ± 10.66	0.32 ± 0.20	87.14 ± 0.07
		500	NE	0.00 ± 0.00	1.12 ± 0.02	5059.78 ± 9.47	0.53 ± 0.15	86.29 ± 0.09
		600	NE	0.00 ± 0.00	1.18 ± 0.01	5076.57 ± 9.69	0.70 ± 0.24	85.36 ± 0.04
		700	NE	0.01 ± 0.00	1.28 ± 0.01	5116.26 ± 8.74	0.57 ± 0.27	84.15 ± 0.07
		800	NE	0.04 ± 0.00	1.44 ± 0.01	5046.28 ± 21.22	0.64 ± 0.32	82.52 ± 0.07
		825*	95.48 ± 67.12	1.75 ± 0.00	8.30 ± 0.03	8210.32 ± 39.84	0.66 ± 0.36	49.43 ± 0.08
		900	23.49 ± 7.26	1.78 ± 0.00	8.90 ± 0.10	8753.73 ± 45.22	1.07 ± 0.25	47.45 ± 0.24
		1000	8.78 ± 1.04	1.81 ± 0.00	9.55 ± 0.07	8938.26 ± 61.41	1.40 ± 0.20	44.70 ± 0.14
2	SPC/E (flex.)	800	N/A	0.02 ± 0.00	1.30 ± 0.03	5003.81 ± 13.53	0.05 ± 0.08	83.97 ± 0.14
		850	N/A	0.04 ± 0.00	1.44 ± 0.02	5032.49 ± 13.40	0.13 ± 0.11	82.91 ± 0.07
		875*	439.07 ± 461.91	1.84 ± 0.00	10.54 ± 0.02	8904.78 ± 22.73	0.06 ± 0.13	42.03 ± 0.12
		900	202.85 ± 196.00	1.85 ± 0.00	10.65 ± 0.10	8955.66 ± 53.45	0.08 ± 0.08	41.66 ± 0.24
		1000	33.71 ± 5.41	1.86 ± 0.00	10.99 ± 0.10	9049.62 ± 44.82	0.14 ± 0.10	39.97 ± 0.31
2	SW	800	N/A	0.06 ± 0.02	1.52 ± 0.05	5129.51 ± 38.14	1.66 ± 0.51	82.51 ± 0.24
		825*	558.36 ± 268.13	1.84 ± 0.00	10.45 ± 0.12	9168.66 ± 68.27	2.16 ± 0.67	44.27 ± 0.28
		850	385.98 ± 217.29	1.85 ± 0.00	10.66 ± 0.12	9246.75 ± 65.27	2.71 ± 0.48	43.39 ± 0.19
		900	146.01 ± 29.46	1.85 ± 0.01	10.84 ± 0.20	9400.32 ± 124.24	2.05 ± 0.86	42.51 ± 0.24
		1000	88.89 ± 15.93	1.87 ± 0.00	11.41 ± 0.12	9466.73 ± 168.27	2.35 ± 0.36	40.47 ± 0.23
3	SPC/E	0	NE	0.00 ± 0.00	0.99 ± 0.01	11309.34 ± 8.48	0.13 ± 0.09	90.00 ± 0.02
		100	NE	0.00 ± 0.00	1.00 ± 0.01	11300.09 ± 7.97	0.20 ± 0.07	89.36 ± 0.01
		200	NE	0.00 ± 0.00	1.03 ± 0.01	11309.01 ± 10.28	0.19 ± 0.07	88.69 ± 0.03
		300	NE	0.00 ± 0.00	1.06 ± 0.01	11317.75 ± 10.74	0.18 ± 0.06	87.99 ± 0.03
		400	NE	0.00 ± 0.00	1.11 ± 0.01	11332.59 ± 9.75	0.21 ± 0.06	87.23 ± 0.03
		500	NE	0.00 ± 0.00	1.17 ± 0.01	11366.50 ± 16.00	0.22 ± 0.06	86.37 ± 0.05
		600	NE	0.01 ± 0.00	1.28 ± 0.02	11452.40 ± 17.58	0.30 ± 0.07	85.29 ± 0.07
		650	NE	0.03 ± 0.00	1.40 ± 0.01	11469.60 ± 22.16	0.23 ± 0.04	84.45 ± 0.04
		700*	155.86 ± 219.57	1.85 ± 0.00	10.57 ± 0.03	19957.38 ± 54.30	0.27 ± 0.04	50.83 ± 0.05
		800	20.17 ± 2.27	1.87 ± 0.00	11.74 ± 0.07	20997.08 ± 128.50	0.63 ± 0.12	47.39 ± 0.13
		900	11.15 ± 1.02	1.89 ± 0.00	12.47 ± 0.09	21464.25 ± 133.17	0.77 ± 0.06	44.84 ± 0.08
4	SPC/E	0	NE	0.00 ± 0.00	1.00 ± 0.01	20054.64 ± 12.60	0.13 ± 0.04	90.01 ± 0.01
		100	NE	0.00 ± 0.00	1.01 ± 0.01	20050.60 ± 11.49	0.16 ± 0.03	89.37 ± 0.02
		200	NE	0.00 ± 0.00	1.03 ± 0.03	20066.13 ± 10.74	0.12 ± 0.06	88.75 ± 0.05
		300	NE	0.00 ± 0.00	1.07 ± 0.02	20078.14 ± 11.53	0.11 ± 0.07	88.06 ± 0.07
		400	NE	0.00 ± 0.00	1.12 ± 0.02	20114.09 ± 15.66	0.15 ± 0.08	87.33 ± 0.12
		500	NE	0.01 ± 0.00	1.23 ± 0.02	20235.95 ± 23.00	0.16 ± 0.03	86.33 ± 0.04
		600	NE	0.06 ± 0.01	1.49 ± 0.04	20667.26 ± 83.91	0.12 ± 0.06	84.76 ± 0.14
		650	56.32 ± 7.16	1.90 ± 0.00	13.05 ± 0.18	38154.20 ± 245.90	0.28 ± 0.04	50.91 ± 0.15
		700	26.84 ± 2.78	1.90 ± 0.00	13.64 ± 0.09	38759.21 ± 139.28	0.37 ± 0.06	49.06 ± 0.07
		800	16.21	1.92	14.91	39670.76	0.56	46.11
		900	10.42	1.93	15.90	40721.76	0.61	43.93

Table D.1: The parameter values averaged (± standard deviation) over both replicate simulations and the time interval over which the structure was in the final equilibrium shape (i.e. the whole simulation interval for runs with no extension and the time interval the droplet spent in an extended shape for runs where stretching occurred). Only a few of simulations showed shape elongation for the electric field with an asterisk *. The parameter values for these cases are the average of the elongated simulations only.

D.2 Energetic analysis result of nanodroplet stretching simulations

In Table D.2, we present energetic analysis data from the stretching simulations.

r_0 [nm]	water model used	electric field, E [MV/m]	electrostatic energy [kJ/mol]	Lennard-Jones Energy [kJ/mol]	dipole-dipole energy [kJ/mol]	dipole-field potential energy [kJ/mol]	surface energy [kJ/mol]
2	SPC/E	0	-58674.92 ± 327.71	9761.25 ± 81.41	-26397.95 ± 103.23	0.00 ± 0.00	1930.82 ± 4.97
		100	-58680.39 ± 320.68	9764.39 ± 82.21	-26394.13 ± 105.08	-6.41 ± 0.32	1930.18 ± 3.65
		200	-58648.74 ± 313.17	9763.65 ± 77.11	-26374.24 ± 102.75	-25.58 ± 0.97	1930.20 ± 4.70
		300	-58600.41 ± 316.54	9731.96 ± 79.37	-26366.53 ± 106.90	-58.75 ± 1.43	1933.57 ± 3.71
		400	-58571.48 ± 317.82	9732.50 ± 74.93	-26347.33 ± 92.08	-104.78 ± 2.48	1936.52 ± 4.08
		500	-58496.08 ± 299.87	9738.59 ± 68.27	-26281.42 ± 92.67	-169.91 ± 4.12	1937.94 ± 3.63
		600	-58390.89 ± 328.22	9716.41 ± 80.30	-26212.27 ± 112.84	-254.70 ± 1.88	1944.37 ± 3.71
		700	-58272.78 ± 324.93	9705.54 ± 76.98	-26154.11 ± 114.96	-374.60 ± 4.55	1959.57 ± 3.35
		800	-57394.88 ± 403.33	9705.85 ± 72.44	-25473.78 ± 170.89	-528.61 ± 6.28	1932.76 ± 8.13
		*825**	*3326.58 ± 98.99*	*-175.10 ± 53.98*	*1017.68 ± 69.65*	*-2077.63 ± 18.10*	*1134.46 ± 12.12*
		900	*2838.16 ± 97.27*	*-327.68 ± 65.02*	*273.97 ± 47.35*	*-2479.84 ± 35.56*	*1333.81 ± 23.55*
		1000	*3364.16 ± 105.57*	*-465.82 ± 67.41*	*284.82 ± 85.39*	*-2907.09 ± 29.27*	*1410.85 ± 31.53*
2	SPC/E (flex.)	800	-75348.50 ± 304.73	14051.72 ± 93.18	-35960.22 ± 93.53	-487.30 ± 11.40	1916.50 ± 5.18
		850	-74874.98 ± 350.58	14015.25 ± 85.53	-35642.32 ± 136.88	-602.45 ± 7.18	1927.48 ± 5.13
		*875**	*3650.38 ± 109.30*	*-520.22 ± 23.98*	*275.44 ± 61.82*	*-3075.09 ± 25.34*	*1457.60 ± 13.28*
		900	*3411.75 ± 162.06*	*-495.05 ± 48.94*	*66.39 ± 115.13*	*-3193.40 ± 39.08*	*1474.15 ± 23.65*
		1000	*3533.38 ± 121.87*	*-546.39 ± 68.83*	*-136.19 ± 62.83*	*-3594.95 ± 31.92*	*1505.29 ± 23.64*
2	SW	800	-63570.63 ± 125.71	8121.23 ± 22.06	-30999.54 ± 69.84	-604.06 ± 19.85	1964.64 ± 14.61
		*825**	*1889.46 ± 145.28*	*139.16 ± 33.07*	*-633.21 ± 127.15*	*-2809.24 ± 13.21*	*1541.72 ± 13.97*
		850	*2002.89 ± 116.54*	*134.25 ± 42.67*	*-676.51 ± 91.40*	*-2948.32 ± 19.95*	*1568.01 ± 30.31*
		900	*2059.88 ± 305.63*	*43.08 ± 132.81*	*-865.69 ± 208.48*	*-3119.92 ± 41.79*	*1611.50 ± 38.25*
		1000	*2007.68 ± 221.53*	*96.93 ± 118.48*	*-1165.73 ± 191.66*	*-3475.77 ± 54.08*	*1623.29 ± 58.72*
3	SPC/E	0	-203164.93 ± 390.99	33376.61 ± 100.38	-90853.16 ± 134.69	0.00 ± 0.00	4331.57 ± 3.25
		100	-203146.55 ± 439.71	33378.04 ± 118.628	-90845.2 ± 148.83	-19.88 ± 0.39	4328.02 ± 3.05
		200	-203084.77 ± 387.27	33367.23 ± 95.678	-90801.11 ± 145.13	-81.07 ± 1.84	4331.44 ± 3.94
		300	-202952.15 ± 398.29	33335.26 ± 101.31	-90739.53 ± 154.72	-186.65 ± 3.03	4334.79 ± 4.11
		400	-202806.43 ± 432.90	33310.08 ± 124.12	-90626.50 ± 160.66	-343.35 ± 3.65	4340.4 ± 3.74
		500	-202552.32 ± 391.28	33282.21 ± 96.61	-90483.16 ± 141.49	-563.44 ± 7.73	4353.46 ± 6.13
		600	-202183.70 ± 383.41	33235.33 ± 123.58	-90271.44 ± 113.39	-875.89 ± 12.76	4386.36 ± 6.73
		650	-201317.45 ± 434.43	33251.23 ± 90.87	-89578.79 ± 179.34	-1108.02 ± 9.02	4392.95 ± 8.49
		*700**	*8317.23 ± 182.53*	*-645.47 ± 39.63*	*1271.62 ± 103.89*	*-6296.29 ± 37.38*	*3137.35 ± 31.55*
		800	*8656.82 ± 169.28*	*-1121.14 ± 120.03*	*105.71 ± 129.68*	*-7896.27 ± 74.30*	*3560.21 ± 46.80*
		900	*9756.49 ± 234.53*	*-1336.68 ± 152.71*	*-64.07 ± 208.65*	*-9214.44 ± 64.33*	*3729.56 ± 52.89*
4	SPC/E	0	-483808.28 ± 117.87	78778.91 ± 76.99	-216128.90 ± 65.90	0.00 ± 0.00	7681.09 ± 4.82
		100	-483734.15 ± 88.13	78750.62 ± 73.95	-216061.05 ± 62.11	-46.02 ± 1.42	7679.54 ± 4.40
		200	-483552.26 ± 103.52	78671.07 ± 104.30	-215998.75 ± 99.31	-184.37 ± 7.34	7685.49 ± 4.11
		300	-483377.17 ± 138.33	78718.77 ± 83.56	-215862.72 ± 86.59	-427.33 ± 16.10	7690.09 ± 4.42
		400	-482916.37 ± 210.32	78649.74 ± 132.09	-215601.79 ± 117.67	-783.56 ± 34.23	7703.86 ± 5.99
		500	-482283.09 ± 142.17	78519.03 ± 85.39	-215271.25 ± 92.99	-1346.06 ± 16.42	7750.53 ± 8.81
		600	-481178.82 ± 131.11	78379.54 ± 80.34	-214628.18 ± 106.21	-2305.14 ± 62.01	7915.73 ± 32.14
		650	*15702.54 ± 240.31*	*-1858.83 ± 213.69*	*-664.68 ± 132.98*	*-14483.71 ± 79.06*	*6652.99 ± 101.48*
		700	*17518.01 ± 251.88*	*-2361.65 ± 104.24*	*-743.73 ± 219.14*	*-16246.24 ± 54.33*	*6910.64 ± 48.40*
		800	*20117.18*	*-2989.55*	*-1349.17*	*-19457.62*	*7252.72*
		900	*23874.42*	*-4170.88*	*-1386.40*	*-22623.18*	*7688.96*

Table D.2: The values in italic for high electric fields are the average net change in different energy components from replicate nanodroplet simulations before and after electric field induced stretching of the nanodroplets. The energetic values given for lower electric fields are the average of $1ns$ simulation. The electric fields with * mark have shape elongation for only a subset of the replicate simulations. The values for those cases are the average of the elongated simulations only. To calculate the surface energy, SPC/E water model surface tension value of 63.3 mJ/m^2 is used for SPC/E and SW water model as well.

D.3 Analysis result of nanodroplet collapsing simulations

In Table D.3, we present analysis data from the collapsing simulations.

number of water	r_0 [nm]	electric field, E_{crit} [MV/m]	ΔU_{int} [kJ/mol]	ΔU_{d-f} [kJ/mol]	angle between dipole and electric field [degree]	ΔSA [nm^2]	$\lambda = \frac{c}{a}$
426	1.45	891	308.96	-1031.39	54.36	13.58	5.85
499	1.53	865	1393.43	-1120.27	56.27	15.57	5.68
603	1.63	807	2107.14	-1220.13	57.76	13.80	5.49
804	1.79	790	1941.11	-1598.36	57.61	21.92	6.05
983	1.92	758	2332.86	-1792.20	59.11	24.41	6.05
1419	2.17	705	2844.41	-2376.63	59.69	33.03	6.41
1948	2.41	666	3492.75	-2973.52	60.82	40.80	6.64
2564	2.64	634	4435.47	-3545.30	62.40	47.45	6.50
3297	2.87	605	5056.83	-4267.07	62.98	57.84	6.72
4124	3.09	583	6239.52	-5422.02	61.42	73.14	7.62
4984	3.30	558	6865.62	-5810.96	63.71	79.18	7.18
5860	3.48	539	7493.75	-6185.12	65.46	83.59	6.78
6822	3.66	526	8116.76	-6765.45	66.44	89.80	6.66
7830	3.83	513	9343.54	-7728.45	65.92	103.88	7.11
8926	4.00	501	10252.82	-8893.92	65.07	119.42	7.63

Table D.3: Critical field calculations: r_0 is the radius when its shape is sphere. E_{crit} is the minimum electric field that the shape of ellipsoid stays as ellipsoid. ΔU_{int} is the change in (ellipsoid U_{int} - sphere U_{int}) droplet internal energy (sum of electrostatic and Lennard-Jones). ΔSA is the change in (ellipsoid SA - sphere SA) surface area.

Appendix E

Details of calculations

E.1 Calculation details of averaging Dipole–dipole interaction energy

Common denominator of part A, B, and C

$$\begin{aligned}
&\int_0^{2\pi}\int_0^{2\pi}\int_0^{\pi}\int_0^{\pi} \lambda e^{-\lambda\theta_i}\lambda e^{-\lambda\theta_j}\frac{1}{2\pi}\frac{1}{2\pi}\,d\theta_i\,d\theta_j\,d\phi_i\,d\phi_j \\
&\qquad = \int_0^{\pi}\lambda e^{-\lambda\theta_i}\,d\theta_i \int_0^{\pi}\lambda e^{-\lambda\theta_j}\,d\theta_j \int_0^{2\pi}\frac{1}{2\pi}\,d\phi_i \int_0^{2\pi}\frac{1}{2\pi}\,d\phi_j \\
&\qquad = \left[-e^{-\lambda\theta_i}\right]_0^{\pi} \times \left[-e^{-\lambda\theta_j}\right]_0^{\pi} \times \left[\frac{\phi_i}{2\pi}\right]_0^{2\pi} \times \left[\frac{\phi_j}{2\pi}\right]_0^{2\pi} \\
&\qquad = -\left[e^{-\lambda\pi}-1\right] \times -\left[e^{-\lambda\pi}-1\right] \times [1-0] \times [1-0] \\
&\qquad = \left(e^{-\lambda\pi}-1\right)^2
\end{aligned}$$

Numerator of part A

$$\begin{aligned}
&\frac{\mu^2}{4\pi\epsilon_0 r^3}\int_0^{2\pi}\int_0^{2\pi}\int_0^{\pi}\int_0^{\pi} \left[\sin\theta_i\sin\theta_j\cos\phi_i\cos\phi_j\right]\,\lambda e^{-\lambda\theta_i}\lambda e^{-\lambda\theta_j}\frac{1}{2\pi}\frac{1}{2\pi}\,d\theta_i\,d\theta_j\,d\phi_i\,d\phi_j \\
&\quad = \frac{\mu^2}{4\pi\epsilon_0 r^3}\int_0^{\pi}\sin\theta_i\lambda e^{-\lambda\theta_i}d\theta_i \int_0^{\pi}\sin\theta_j\lambda e^{-\lambda\theta_j}d\theta_j \int_0^{2\pi}\cos\phi_i\frac{1}{2\pi}d\phi_i \int_0^{2\pi}\cos\phi_j\frac{1}{2\pi}d\phi_j \\
&\quad = \frac{\mu^2}{4\pi\epsilon_0 r^3}\int_0^{\pi}\sin\theta_i\lambda e^{-\lambda\theta_i}d\theta_i \int_0^{\pi}\sin\theta_j\lambda e^{-\lambda\theta_j}d\theta_j \left[\frac{\sin\phi_i}{2\pi}\right]_0^{2\pi} \left[\frac{\sin\phi_i}{2\pi}\right]_0^{2\pi} \\
&\quad = 0
\end{aligned}$$

Numerator of part B

$$\begin{aligned}
&\frac{\mu^2}{4\pi\epsilon_0 r^3}\int_0^{2\pi}\int_0^{2\pi}\int_0^{\pi}\int_0^{\pi}\left[\sin\theta_i\sin\theta_j\sin\phi_i\sin\phi_j\right]\,\lambda e^{-\lambda\theta_i}\lambda e^{-\lambda\theta_j}\frac{1}{2\pi}\frac{1}{2\pi}\,d\theta_i\,d\theta_j\,d\phi_i\,d\phi_j\\
&\quad=\frac{\mu^2}{4\pi\epsilon_0 r^3}\int_0^{\pi}\sin\theta_i\lambda e^{-\lambda\theta_i}d\theta_i\int_0^{\pi}\sin\theta_j\lambda e^{-\lambda\theta_j}d\theta_j\int_0^{2\pi}\sin\phi_i\frac{1}{2\pi}d\phi_i\int_0^{2\pi}\sin\phi_j\frac{1}{2\pi}d\phi_j\\
&\quad=\frac{\mu^2}{4\pi\epsilon_0 r^3}\int_0^{\pi}\sin\theta_i\lambda e^{-\lambda\theta_i}d\theta_i\int_0^{\pi}\sin\theta_j\lambda e^{-\lambda\theta_j}d\theta_j\left[\frac{-\cos\phi_i}{2\pi}\right]_0^{2\pi}\left[\frac{-\cos\phi_i}{2\pi}\right]_0^{2\pi}\\
&\quad=0
\end{aligned}$$

Numerator of part C

$$\begin{aligned}
&-\frac{2\mu^2}{4\pi\epsilon_0 r^3}\int_0^{2\pi}\int_0^{2\pi}\int_0^{\pi}\int_0^{\pi}\left[\cos\theta_i\cos\theta_j\right]\,\lambda e^{-\lambda\theta_i}\lambda e^{-\lambda\theta_j}\frac{1}{2\pi}\frac{1}{2\pi}\,d\theta_i\,d\theta_j\,d\phi_i\,d\phi_j\\
&\quad=-\frac{\mu^2}{2\pi\epsilon_0 r^3}\int_0^{\pi}\cos\theta_i\lambda e^{-\lambda\theta_i}d\theta_i\int_0^{\pi}\cos\theta_j\lambda e^{-\lambda\theta_j}d\theta_j\int_0^{2\pi}\frac{1}{2\pi}d\phi_i\int_0^{2\pi}\frac{1}{2\pi}d\phi_j\\
&\quad=-\frac{\mu^2}{2\pi\epsilon_0 r^3}\cdot\lambda\underbrace{\int_0^{\pi}\cos\theta_i e^{-\lambda\theta_i}d\theta_i}_{\star}\cdot\lambda\underbrace{\int_0^{\pi}\cos\theta_j e^{-\lambda\theta_j}d\theta_j}_{\star}\cdot\left[\frac{\phi_i}{2\pi}\right]_0^{2\pi}\cdot\left[\frac{\phi_i}{2\pi}\right]_0^{2\pi}\\
&\quad=-\frac{\mu^2}{2\pi\epsilon_0 r^3}\cdot\lambda\frac{\lambda}{\lambda^2+1}\left(e^{-\lambda\pi}+1\right)\cdot\lambda\frac{\lambda}{\lambda^2+1}\left(e^{-\lambda\pi}+1\right)\cdot 1\cdot 1\\
&\quad=-\frac{\mu^2\lambda^4\left(e^{-\lambda\pi}+1\right)^2}{2\pi\epsilon_0 r^3\left(\lambda^2+1\right)^2}
\end{aligned}$$

where $\star$ is

$$\begin{aligned}
\int_0^{\pi}\cos xe^{-\lambda x}dx&=\left[\cos x\cdot-\frac{1}{\lambda}e^{-\lambda x}\right]_0^{\pi}-\int_0^{pi}-\sin x\cdot-\frac{1}{\lambda}e^{-\lambda x}dx\\
\int_0^{\pi}\cos xe^{-\lambda x}dx&=-\frac{1}{\lambda}\left[\cos x\cdot e^{-\lambda x}\right]_0^{\pi}-\frac{1}{\lambda}\int_0^{pi}\sin x\cdot e^{-\lambda x}dx\\
\int_0^{\pi}\cos xe^{-\lambda x}dx&=-\frac{1}{\lambda}\left[\cos x\cdot e^{-\lambda x}\right]_0^{\pi}-\frac{1}{\lambda}\left[\left[\sin x\cdot-\frac{1}{\lambda}e^{-\lambda x}\right]_0^{\pi}-\int_0^{pi}\cos x\cdot-\frac{1}{\lambda}e^{-\lambda x}dx\right]\\
\int_0^{\pi}\cos xe^{-\lambda x}dx&=-\frac{1}{\lambda}\left[\cos x\cdot e^{-\lambda x}\right]_0^{\pi}+\frac{1}{\lambda^2}\left[\sin x\cdot e^{-\lambda x}\right]_0^{\pi}-\frac{1}{\lambda^2}\int_0^{pi}\cos x\cdot e^{-\lambda x}dx\\
(1+\frac{1}{\lambda^2})\int_0^{\pi}\cos xe^{-\lambda x}dx&=-\frac{1}{\lambda}\left[\cos x\cdot e^{-\lambda x}\right]_0^{\pi}+\frac{1}{\lambda^2}\left[\sin x\cdot e^{-\lambda x}\right]_0^{\pi}\\
\int_0^{\pi}\cos xe^{-\lambda x}dx&=\frac{\lambda^2}{\lambda^2+1}\cdot-\frac{1}{\lambda}\left[-1\cdot e^{-\lambda\pi}-1\cdot 1\right]\frac{\lambda^2}{\lambda^2+1}\cdot\frac{1}{\lambda^2}\left[0-0\right]\\
\int_0^{\pi}\cos xe^{-\lambda x}dx&=\frac{\lambda}{\lambda^2+1}\left(e^{-\lambda\pi}+1\right)
\end{aligned}$$

Bibliography

[1] J. D. Sartor, "Electricity and rain," *Q. J. Roy. Meteor. Soc.*, vol. 22, pp. 45–51, August 1969.

[2] P. R. Brazier-Smith, S. G. Jennings, J. Latham, C. B. Moore, and B. Vonnegut, "Increased rates of rainfall production in electrified clouds," *Q. J. Roy. Meteor. Soc.*, vol. 99, pp. 776–786, October 1973.

[3] A. G. Bailey, *Electrostatic Spraying of Liquids*, vol. 10 of *Electronic & electrical engineering research studies: Electrostatics & Electrostatic Applications series*. Research Studies Press, 1988.

[4] D. H. Reneker and I. Chun, "Nanometre diameter fibres of polymer, produced by electrospinning," *Nanotechnology*, vol. 7, pp. 216–223, September 1996.

[5] Y. Dzenis, "Spinning Continuous Fibers for Nanotechnology," *Science*, vol. 304, pp. 1917–1919, June 2004.

[6] J. B. Fenn, M. Mann, C. K. Meng, S. F. Wong, and C. M. Whitehouse, "Electrospray ionization for mass spectrometry of large biomolecules," *Science*, vol. 246, pp. 64–71, October 1989.

[7] J. B. Fenn, "Electrospray Wings for Molecular Elephants (Nobel Lecture)," *Angewandte Chemie International Edition*, vol. 42, no. 33, pp. 3871–3894, 2003.

[8] H. R. Pruppacher, "Electrofreezing of Supercooled Water," *Pure and Applied Geophysics*, vol. 104, pp. 623–634, December 1973.

[9] I. M. Svishchev and P. G. Kusalik, "Electrofreezing of Liquid Water: A Microscopic Perspective," *Journal of the American Chemical Society*, vol. 118, pp. 649–654, January 1996.

[10] K. Carpenter and V. Bahadur, "Electrofreezing of Water Droplets under Electrowetting Fields," *Langmuir*, vol. 31, no. 7, pp. 2243–2248, 2015.

[11] J. Y. Yan, S. D. Overduin, and G. N. Patey, "Understanding electrofreezing in water simulations," *The Journal of Chemical Physics*, vol. 141, p. 074501, August 2014.

[12] S. E. Law and H. D. Bowen, "Hydrodynamic Instability of Charged Pesticide Droplets Settling from Crop-Spraying Aircraft: Theoretical Implications," *Transactions of the ASAE (American Society of Agricultural Engineers)*, vol. 31, pp. 1689–1691, November–December 1988.

[13] R. L. Hines, "Electrostatic Atomization and Spray Painting," *JPN J. Appl. Phys.*, vol. 37, pp. 2730–2736, June 1966.

[14] P. Gregory, "Ink–jet printing," in *High–Technology Applications of Organic Colorants*, Topics in Applied Chemistry, ch. 9, pp. 175–205, Springer US, 1991.

[15] R. W. Kenyon, "Ink jet printing," in *Chemistry and Technology of Printing and Imaging Systems* (P. Gregory, ed.), pp. 113–138, Springer Netherlands, January 1996.

[16] E. Neumann, M. Schaefer-Ridder, Y. Wang, and P. Hofschneider, "Gene transfer into mouse lyoma cells by electroporation in high electric fields," *EMBO Journal*, vol. 1, no. 7, pp. 841–845, 1982.

[17] D. P. Tieleman, H. Leontiadou, A. E. Mark, and S.-J. Marrink, "Simulation of Pore Formation in Lipid Bilayers by Mechanical Stress and Electric Fields," *Journal of the American Chemical Society*, vol. 125, pp. 6382–6383, May 2003.

[18] D. P. Tieleman, "The molecular basis of electroporation," *BMC Biochemistry*, vol. 5, pp. 1–12, July 2004.

[19] M. Tarek, "Membrane Electroporation: A Molecular Dynamics Simulation," *Biophysical Journal*, vol. 88, pp. 4045–4053, June 2005.

[20] P. T. Vernier and M. J. Ziegler, "Nanosecond Field Alignment of Head Group and Water Dipoles in Electroporating Phospholipid Bilayers," *Journal of Physical Chemistry B*, vol. 111, pp. 12993–12996, October 2007.

[21] M. J. Ziegler and P. T. Vernier, "Interface Water Dynamics and Porating Electric Fields for Phospholipid Bilayers," *Journal of Physical Chemistry B*, vol. 112, pp. 13588–13596, October 2008.

[22] R. A. Böckmann, B. L. de Groot, S. Kakorin, E. Neumann, and H. Grubmüller, "Kinetics, Statistics, and Energetics of Lipid Membrane Electroporation Studied by Molecular Dynamics Simulations," *Biophysical Journal*, vol. 95, pp. 1837–1850, August 2008. Biophysical Society.

[23] E. Neumann, S. Kakorin, and K. Toensing, "Fundamentals of electroporative delivery of drugs and genes," *Bioelectrochemistry and Bioenergetics*, vol. 48, pp. 3–16, February 1999.

[24] K. H. Schoenbach, R. P. Joshi, J. F. Kolb, N. Chen, M. Stacey, P. F. Blackmore, E. S. Buescher, and S. J. Beebe, "Ultrashort Electrical Pulses Open a New Gateway Into Biological Cells," *Proceedings of the IEEE*, vol. 92, pp. 1122–1137, July 2004.

[25] P. T. Vernier, "Delivery of Nanosecond, Megawatt, Pulsed Electrical Energy to Membranes, Cells, and Tissues – Biophysics and Therapeutics," in *Electroporation based technologies and treatments: International Scientific Workshop and Postgraduate Course, Proceedings of the*, pp. 91–95, University of Ljubljana, Faculty of Electrical Engineering, November 2009.

[26] A. A. Gurtovenko and I. Vattulainen, "Pore Formation Coupled to Ion Transport through Lipid Membranes as Induced by Transmembrane Ionic Charge Imbalance: Atomistic Molecular Dynamics Study," *Journal of the American Chemical Society*, vol. 127, pp. 17570–17571, November 2005.

[27] A. A. Gurtovenko and I. Vattulainen, "Ion Leakage through Transient Water Pores in Protein-Free Lipid Membranes Driven by Transmembrane Ionic Charge Imbalance," *Biophysical Journal*, vol. 92, pp. 1878–1890, March 2007.

[28] S. W. Siu and R. A. Böckmann, "Electric field effects on membranes: Gramicidin A as a test ground," *Journal of Structural Biology*, vol. 157, pp. 545–556, October 2007.

[29] U. Essmann, L. Perera, M. L. Berkowitz, T. Darden, H. Lee, and L. G. Pedersen, "A smooth particle mesh Ewald method," *Journal of Chemical Physics*, vol. 103, pp. 8577–8593, November 1995.

[30] L. R. F.R.S, "On the Equilibrium of Liquid Conducting Masses charged with Electricity," *Philosophical Magazine*, vol. 14, pp. 184–186, July 1882.

[31] G. I. Taylor, "Disintegration of Water Drops in an Electric Field," *Proceedings of the Royal Society of London. Series A. Mathematical and Physical Sciences*, vol. 280, pp. 383–397, July 1964.

[32] D. Duft, T. Achtzehn, R. Müller, B. A. Huber, and T. Leisner, "Coulomb fission: Rayleigh jets from levitated microdroplets," *Nature*, vol. 421, pp. 128–128, January 2003.

[33] O. A. Basaran and L. E. Scriven, "Axisymmetric shapes and stability of charged drops in an external electric field," *Phys. Fluids A*, vol. 1, pp. 799–809, May 1989.

[34] R. T. Collins, K. Sambath, M. T. Harris, and O. A. Basaran, "Universal scaling laws for the disintegration of electrified drops," *PNAS*, vol. 110, pp. 4905–4910, March 2013.

[35] L. Zhao and P. Choi, "Molecular dynamics simulation of the coalescence of nanometer-sized water droplets in n-heptane," *The Journal of Chemical Physics*, vol. 120, no. 4, pp. 1935–1942, 2004.

[36] M.-L. Liao, S.-P. Ju, and S.-H. Yang, "Coalescence behavior of water nanoclusters: Temperature and size effects," *The Journal of Physical Chemistry C*, vol. 111, no. 19, pp. 6927–6932, 2007.

[37] L. Rekvig and D. Frenkel, "Molecular simulations of droplet coalescence in oil/water/surfactant systems," *The Journal of Chemical Physics*, vol. 127, no. 13, pp. –, 2007.

[38] W. D. Luedtke, U. Landman, Y.-H. Chiu, D. J. Levandier, R. A. Dressler, S. Sok, and M. S. Gordon, "Nanojets, Electrospray, and Ion Field Evaporation: Molecular Dynamics Simulations and Laboratory Experiments," *J. Phys. Chem. A*, vol. 112, pp. 9628–9649, October 2008.

[39] W. D. Luedtke, J. Gao, and U. Landman, "Dielectric Nanodroplets: Structure, Stability, Thermodynamics, Shape Transitions and Electrocrystallization in Applied Electric Fields," *J. Phys. Chem. C*, vol. 115, pp. 20343–20358, September 2011.

[40] U. Zimmermann, "Electric field-mediated fusion and related electrical phenomena," *Biochimica et Biophysica Acta (BBA) - Reviews on Biomembranes*, vol. 694, pp. 227–277, November 1982.

[41] M.-P. Rols, "Electropermeabilization, a physical method for the delivery of therapeutic molecules into cells," *Biochimica et Biophysica Acta (BBA) - Biomembranes*, vol. 1758, pp. 423–428, March 2006.

[42] R. Heller, M. J. Jaroszeski, L. F. Glass, J. L. Messina, D. P. Rapaport, R. C. DeConti, N. A. Fenske, R. A. Gilbert, L. M. Mir, and D. S. Reintgen, "Phase I/II trial for the treatment of cutaneous and subcutaneous tumors using electrochemotherapy," *Cancer*, vol. 77, pp. 964–971, Mar. 1996. WOS:A1996TW39500024.

[43] M. Marty, G. Sersa, J. R. Garbay, J. Gehl, C. G. Collins, M. Snoj, V. Billard, P. F. Geertsen, J. O. Larkin, D. Miklavcic, I. Pavlovic, S. M. Paulin-Kosir, M. Cemazar, N. Morsli, D. M. Soden, Z. Rudolf, C. Robert, G. C. OSullivan, and L. M. Mir, "Electrochemotherapy - An easy, highly effective and safe treatment of cutaneous and subcutaneous metastases: Results of ESOPE (European Standard Operating Procedures of Electrochemotherapy) study," *EJC Supplements*, vol. 4, pp. 3–13, November 2006.

[44] B. Rubinsky, "Irreversible electroporation in medicine," *Technology in cancer research & treatment*, vol. 6, pp. 255–260, August 2007.

[45] E. B. Garon, D. Sawcer, P. T. Vernier, T. Tang, Y. Sun, L. Marcu, M. A. Gundersen, and H. P. Koeffler, "In vitro and in vivo evaluation and a case report of intense nanosecond pulsed electric field as a local therapy for human malignancies," *International journal of cancer. Journal international du cancer*, vol. 121, pp. 675–682, Aug. 2007.

[46] R. Nuccitelli, X. Chen, A. G. Pakhomov, W. H. Baldwin, S. Sheikh, J. L. Pomicter, W. Ren, C. Osgood, R. J. Swanson, J. F. Kolb, S. J. Beebe, and K. H. Schoenbach, "A new pulsed electric field therapy for melanoma disrupts the tumor's blood supply and causes complete remission without recurrence," *International journal of cancer. Journal international du cancer*, vol. 125, pp. 438–445, July 2009.

[47] J. Teissie, M. Golzio, and M. P. Rols, "Mechanisms of cell membrane electropermeabilization: a minireview of our present (lack of ?) knowledge," *Biochimica et biophysica acta*, vol. 1724, pp. 270–280, August 2005.

[48] J. C. Weaver and Y. A. Chizmadzhev, "Theory of electroporation: A review," *Bioelectrochemistry and Bioenergetics*, vol. 41, pp. 135–160, December 1996.

[49] T. Kotnik and D. Miklavcic, "Second-order model of membrane electric field induced by alternating external electric fields," *IEEE transactions on bio-medical engineering*, vol. 47, pp. 1074–1081, Aug. 2000.

[50] I. Abidor, V. Arakelyan, L. Chernomordik, Y. Chizmadzhev, V. Pastushenko, and M. TARASEVICH, "Electric breakdown of bilayer lipid-membranes.1.Main experimental facts and their qualitative discussion," *Bioelectrochemistry and Bioenergetics*, vol. 6, no. 1, pp. 37–52, 1979.

[51] R. Benz, F. Beckers, and U. Zimmermann, "Reversible Electrical Breakdown of Lipid Bilayer Membranes: A Charge-Pulse Relaxation Study," *Journal of Membrane Biology*, vol. 48, pp. 181–204, June 1979.

[52] M. Robello and A. Gliozzi, "Conductance transition induced by an electric-field in lipid bilayers," *Biochimica Et Biophysica Acta*, vol. 982, pp. 173–176, June 1989. WOS:A1989AF39300024.

[53] I. Genco, A. Gliozzi, A. Relini, M. Robello, and E. Scalas, "Electroporation in symmetrical and asymmetric membranes," *Biochimica Et Biophysica Acta*, vol. 1149, pp. 10–18, June 1993. WOS:A1993LJ68600002.

[54] S. Kalinowski, G. Ibron, K. Bryl, and Z. Figaszewski, "Chronopotentiometric studies of electroporation of bilayer lipid membranes," *Biochimica Et Biophysica Acta-Biomembranes*, vol. 1369, pp. 204–212, March 1998. WOS:000072653500003.

[55] K. C. Melikov, V. A. Frolov, A. Shcherbakov, A. V. Samsonov, Y. A. Chizmadzhev, and L. V. Chernomordik, "Voltage-induced nonconductive pre-pores and metastable single pores in unmodified planar lipid bilayer," *Biophysical Journal*, vol. 80, pp. 1829–1836, April 2001. WOS:000167797800020.

[56] M. Kotulska, J. Basalyga, M. B. Derylo, and P. Sadowski, "Metastable Pores at the Onset of Constant-Current Electroporation," *Journal of Membrane Biology*, vol. 236, pp. 37–41, July 2010. WOS:000280599700005.

[57] P. T. Vernier, M. J. Ziegler, Y. Sun, W. V. Chang, M. A. Gundersen, and D. P. Tieleman, "Nanopore Formation and Phosphatidylserine Externalization in a Phospholipid Bilayer at High Transmembrane Potential," *Journal of the American Chemical Society*, vol. 128, pp. 6288–6289, April 2006.

[58] Q. Hu, S. Viswanadham, R. P. Joshi, K. H. Schoenbach, S. J. Beebe, and P. F. Blackmore, "Simulations of transient membrane behavior in cells subjected to a high-intensity ultrashort electric pulse," *Physical review. E, Statistical, nonlinear, and soft matter physics*, vol. 71, p. 031914, March 2005.

[59] Z. A. Levine and P. T. Vernier, "Life cycle of an electropore: field-dependent and field-independent steps in pore creation and annihilation," *The Journal of membrane biology*, vol. 236, pp. 27–36, July 2010.

[60] H. J. C. Berendsen, J. R. Grigera, and T. P. Straatsma, "The missing term in effective pair potentials," *The Journal of Physical Chemistry*, vol. 91, no. 24, pp. 6269–6271, 1987.

[61] H. J. C. Berendsen, J. P. M. Postma, W. F. van Gunsteren, and J. Hermans, "Interaction Models for Water in Relation to Protein Hydration," in *Intermolecular*

Forces (B. Pullman, ed.), vol. 14, pp. 331–342, Springer, 1981. Proceedings of the Fourteenth Jerusalem Symposium on Quantum Chemistry and Biochemistry Held in Jerusalem, Israel, April 1316, 1981.

[62] D. M. Ferguson, "Parameterization and evaluation of a flexible water model," *Journal of Computational Chemistry*, vol. 16, no. 4, pp. 501–511, 1995.

[63] O. Berger, O. Edholm, and F. Jahnig, "Molecular dynamics simulations of a fluid bilayer of dipalmitoylphosphatidylcholine at full hydration, constant pressure, and constant temperature," *Biophysical Journal*, vol. 72, pp. 2002–2013, May 1997.

[64] H. J. C. Berendsen, J. P. M. Postma, W. F. van Gunsteren, and J. R. Haak, "Moleculear dynamics with coupling to an external bath," *Journal of Chemical Physics*, vol. 81, no. 8, pp. 3684–3690, 1984.

[65] G. Bussi, D. Donadio, and M. Parrinello, "Canonical sampling through velocity rescaling," *The Journal of Chemical Physics*, vol. 126, no. 014101, pp. 1–7, 2007.

[66] B. Hess, H. Bekker, H. J. C. Berendsen, and J. G. E. M. Fraaije, "LINCS: A linear constraint solver for molecular simulations," *Journal of Computational Chemistry*, vol. 18, pp. 1463–1472, September 1997.

[67] D. Bostick and M. L. Berkowitz, "The implementation of slab geometry for membrane-channel molecular dynamics simulations," *Biophysical journal*, vol. 85, pp. 97–107, July 2003.

[68] W. Humphrey, A. Dalke, and K. Schulten, "VMD - Visual Molecular Dynamics," *Journal of Molecular Graphics & Modelling*, vol. 14, pp. 33–38, February 1996.

[69] J. Vanderlinde, *Classical Electromagnetic Theory*, vol. Book 145 of *Fundamental Theories of Physics*. Springer, 2nd ed., 2004.

[70] P. F. B. Goncalves and H. Stassen, "Calculation of the free energy of solvation from molecular dynamics simulations," *Pure and Applied Chemistry*, vol. 76, pp. 231–240, January 2004. WOS:000189349400027.

[71] M. Tokman, J. H. Lee, Z. A. Levine, M.-C. Ho, M. E. Colvin, and P. T. Vernier, "Electric Field-Driven Water Dipoles: Nanoscale Architecture of Electroporation," *PLOS ONE*, vol. 8, p. e61111, April 2013.

[72] H. R. Pruppacher, "The Effect of an External Electric Field on the Supercooling of Water Drops," *Journal of Geophysical Research*, vol. 68, pp. 4463–4474, August 1963.

[73] I.-C. Yeh and M. L. Berkowitz, "Dielectric constant of water at high electric fields: Molecular dynamics study," *The Journal of Chemical Physics*, vol. 110, no. 16, pp. 7935–7942, 1999.

[74] T. Schwede and M. C. Peitsch, *Computational Structural Biology: Methods and Applications*. World Scientific, 2008.

[75] M. Cloupeau and B. Prunet-Foch, "Electrostatic spraying of liquids in cone-jet mode," *J. Electrostat.*, vol. 22, pp. 135–159, July 1989.

[76] P. J. van Maaren and D. van der Spoel, "Molecular dynamics simulations of water with novel shell-model potentials," *The Journal of Physical Chemistry B*, vol. 105, no. 13, pp. 2618–2626, 2001.

[77] Wikipedia, The Free Encyclopedia, "Gyration tensor." `http://en.wikipedia.org/wiki/Gyration_tensor`. [Online].

[78] D. N. Theodorou and U. W. Suter, "Shape of Unperturbed Linear Polymers: Polypropylene," *Macromolecules*, vol. 18, pp. 1206–1214, June 1985.

[79] R. I. Dima and D. Thirumalai, "Asymmetry in the Shapes of Folded and Denatured States of Proteins," *The Journal of Physical Chemistry B*, vol. 108, pp. 6564–6570, March 2004.

[80] C. Vega and E. de Miguel, "Surface tension of the most popular models of water by using the test-area simulation method," *The Journal of Chemical Physics*, vol. 126, p. 154707, April 2007.

[81] J. Zeleny, "The Electrical Discharge from Liquid Points, and a Hydrostatic Method of Measuring the Electric Intensity at Their Surfaces," *Phys. Rev.*, vol. 3, pp. 69–91, February 1914.

[82] J. Zeleny, "Instability of Electrified Liquid Surfaces," *Phys. Rev.*, vol. 10, pp. 1–6, July 1917.

[83] D. A. Scherlis, J.-L. Fattebert, F. Gygi, M. Cococcioni, and N. Marzari, "A unified electrostatic and cavitation model for first-principles molecular dynamics in solution," *The Journal of Chemical Physics*, vol. 124, p. 074103, February 2006.

[84] M. Schrader, P. Virnau, and K. Binder, "Simulation of vapor-liquid coexistence in finite volumes: A method to compute the surface free energy of droplets," *Physical Review E*, vol. 79, p. 061104, June 2009.

[85] Wikipedia, The Free Encyclopedia, "Moment of inertia." `https://en.wikipedia.org/wiki/Moment_of_inertia`. [Online].

[86] D. Baraff, "An introduction to physically based modeling: Rigid body simulation i - unconstrained rigid body dynamics." `http://www.cs.cmu.edu/~baraff/sigcourse/notesd1.pdf`, 1997. Physically Based Modeling: Principles and Practice (Online SIGGRAPH '97 Course notes).

[87] Wikipedia, The Free Encyclopedia, "List of moments of inertia." `http://en.wikipedia.org/wiki/List_of_moments_of_inertia`. [Online].

[88] Wikipedia, The Free Encyclopedia, "Ellipsoid." `http://en.wikipedia.org/wiki/Ellipsoid`. [Online].

[89] Wikipedia, The Free Encyclopedia, "Elliptic integral." `http://en.wikipedia.org/wiki/Elliptic_integral`. [Online].

[90] Mathematics Source Library, "Elliptic Integrals." `http://www.mymathlib.com/functions/elliptic_integrals.html`. [Online].